UNIVERSIDADE TECNOLÓGICA FEDERAL DO PARANÁ

ANDRE RENAN MAYER

EVALUATION OF AISI H13 AND Cr_3C_2 25NiCr HVOF COATINGS AGAINST DIE SOLDERING FOR ALUMINUM HIGH PRESSURE DIE CASTING

MASTER'S THESIS

PONTA GROSSA

2022

ANDRE RENAN MAYER

EVALUATION OF AISI H13 AND Cr_3C_2 25NiCr HVOF COATINGS AGAINST DIE SOLDERING FOR ALUMINUM HIGH PRESSURE DIE CASTING

Avaliação dos revestimentos HVOF AISI H13 e Cr_3C_2 25NiCr contra fenômeno de soldagem para fundição sob alta pressão de Alumínio

Master's thesis presented as a partial requirement for obtaining the Master's degree in Mechanical Engineering, from the Graduate Program in Mechanical Engineering, Federal University of Technology, campus of Ponta Grossa. Field: Mechanical Manufacturing and Materials.

Advisor: Prof. Dr. Anderson Geraldo Marenda Pukasiewicz

PONTA GROSSA

2022

Ministério da Educação
Universidade Tecnológica Federal do Paraná
Campus Ponta Grossa

ANDRE RENAN MAYER

EVALUATION OF AISI H13 AND CR3C2 25NICR HVOF COATINGS AGAINST DIE SOLDERING FOR ALUMINUM HIGH PRESSURE DIE CASTING

Trabalho de pesquisa de mestrado apresentado como requisito para obtenção do título de Mestre Em Engenharia Mecânica da Universidade Tecnológica Federal do Paraná (UTFPR). Área de concentração: Fabricação Mecânica E Materiais.

Data de aprovação: 02 de Maio de 2022

Dr. Anderson Geraldo Marenda Pukasiewicz, Doutorado - Universidade Tecnológica Federal do Paraná

Dr. Gelson Biscaia De Souza, Doutorado - Universidade Estadual de Ponta Grossa (Uepg)

Dr. Hipolito Domingo Carvajal Fals, Doutorado - Universidade Tecnológica Federal do Paraná

Documento gerado pelo Sistema Acadêmico da UTFPR a partir dos dados da Ata de Defesa em 09/05/2022.

“An investment in knowledge pays
the best interests”.

(Benjamin Franklin)

ACKNOWLEDGMENTS

While writing this thesis, I have been supported by many colleagues. Colleagues whom I am proud of calling friends. Unfortunately, I will not be able to name every person who has helped me.

Firstly, I would like to thank my family for all the support, especially my mother, that has been taking care of my grandmother at this challenging moment. For me, her name should be the meaning of hardworking. I also want to cite my father, who has always advised me to study.

I am also thankful for meeting Prof. Dr. Anderson. He has been my advisor for a long time and an excellent friend. I know how I have demanded his time over the years, and I am grateful for having him as an advisor. I hope one day to be able to reciprocate.

Dr. Willian, I am grateful for all the philosophical discussions we have had. He has changed how I behave as a researcher. All the knowledge I have absorbed from him is priceless.

Dr. Hipolito is an expert in his field and one of the most intelligent people I know. Nevertheless, he has always treated me equally. That is a behavior I want to inherit from him. He is an excellent professor; I still have a lot to learn from him.

MSc. Eriel, I am thankful for the assistance at the machine shop. I wish the best for him and his wife, MSc. Simone. I genuinely believe he should pursue becoming a professor. All his machinery expertise and patience would make him an excellent professional.

I want to thank all the companies involved in the route 2030 project, in special Villares Metals and Oerlikon Balzers, for supplying materials.

I would also like to thank to the *Centro de Caracterização Multiusuário em Pesquisa e Desenvolvimento de Materiais* (C2MMa) for the analyzes carried out. Without them, this thesis would lack the equipment required for many of the analyses performed.

A special thanks to everybody else who has helped me throughout this process. Without all the people involved in this process, I would not be able to accomplish this thesis.

ABSTRACT

This thesis aims to study high-velocity oxygen fuel (HVOF) coatings for high pressure die casting (HPDC). Wear is found in most fabrication processes and is usually hard to overcome, which is no different for HPDC. Several wear mechanisms are found, and the die is worn as the process occurs. Processes like nitriding and physical vapor deposition are used to improve the surface quality. Nonetheless, these processes only create a superficial change, and the geometry barely changes. Therefore, it is not unusual to recover these surfaces via welding. However, the surface quality achieved via welding is as good as the original. Furthermore, the study of coatings applied via thermal sprays is lacking in the literature. As thermally sprayed coatings have a wide range of properties, a handful of surface engineering problems can be solved by this technique. Coatings based on Cr3C2 25NiCr and AISI H13 were chosen due to the shortage of studies regarding their use for HPDC. Bulk AISI H13 and AISI H13 coated with AlCrN PVD were used as a comparative. Hot corrosion tests were performed to establish coatings performance against molten A383 aluminum alloy. Additionally, a soldering testing process was proposed. Soldering analyses have shown an extensive amount of information regarding the soldering mechanisms and corrosion of the surface. The mechanisms of each surface for soldering and corrosion were evaluated using scanning electron microscopy (SEM) and energy dispersive x-ray spectroscopy (EDS). Concerning the properties of the surfaces, in general, AlCrN PVD coating showed the best performance. Even so, the change in nitrogen concentration indicates the coating degradation by nitrogen diffusion. The corrosion rate for AISI H13 was diminished when sprayed by HVOF. It was explained by the chemical corrosion during the spraying process, creating iron oxides. However, the uneven corrosion created spikes which increased the surface soldering. The corrosion of Cr3C2 25NiCr was also evaluated and showed a small diffusional layer. However, the soldering forces were high. The stabilization of a Cr-Al-Si strong phase with small spikes created a high adhered intermetallic.

Keywords: HVOF; HPDC; molten metal corrosion; die soldering; wear.

RESUMO

Esta dissertação tem como objetivo o estudo de revestimentos de *high velocity oxygen fuel* (HVOF) com relação as suas propriedades para fundição sob alta pressão. Desgaste é encontrado na maioria dos processos de fabricação, e normalmente é difícil de contornar, o que não é diferente para HPDC. Ao passo que o processo ocorre, diversos mecanismos de desgaste são encontrados e o molde desgastado. Processos como nitretação e deposição física de vapor são utilizados para melhorar a qualidade superficial. Ainda assim, esses processos apenas criam uma mudança superficial, e a geometria é pouco modificada. Sendo assim, não é incomum a recuperação dessas superfícies por soldagem. Entretanto, a qualidade superficial adquirida por soldagem é distante da original. Além do mais, o estudo de revestimentos aplicados por spray térmico para HPDC é insuficiente na literatura. Como revestimento termicamente aspergido possuem uma ampla variedade de propriedades, uma grande quantia de problemas de engenharia de superfície pode ser resolvida com essa técnica. Revestimentos a base de Cr_3C_2 e AISI H13 foram escolhidos devido à falta de estudos em relação a seu uso para HPDC. Para comparação, AISI H13 e AISI H13 revestido com PVD de AlCrN foram utilizados. Ensaios de corrosão a quente foram realizados com o objetivo de estabelecer a performance desses revestimentos contra a liga de alumínio A383 fundido. Adicionalmente, um ensaio de *soldering* foi proposto. As análises de *soldering* mostraram uma extensiva quantia de informação com relação não apenas a mecanismos de *soldering,* mas também corrosão da superfície. Os mecanismos de cada superfície para soldering e corrosão foram avaliadas usando microscopia eletrônica de varredura (MEV) e espectrometria por dispersão de energia de raios-x (EDE). Quanto as propriedades da superfície, em geral o revestimento de AlCrN PVD mostrou a melhor performance. Ainda assim, a mudança na concentração de nitrogênio indica a degradação do revestimento por difusão do nitrogênio. A taxa de corrosão do AISI H13 diminuiu quando aspergido por HVOF. Isso é explicado pela corrosão durante o processo de aspersão, criando óxido de ferro. Entretanto, a corrosão não homogenia criou *spikes* os quais aumentaram o fenômeno de *soldering* da superfície. A corrosão do Cr3C2 25NiCr também foi analisada, e mostrou uma pequena camada difusional. Não obstante, as forças de soldering foram elevadas. A estabilização de resistentes fases de Cr-Al-Si com pequenos spikes criaram uma forte adesão de intermetálicos.

Palavras-chave: HVOF; HPDC; corrosão em metal fundido; soldagem do molde; desgaste.

LIST OF FIGURES

LIST OF GRAPHS

LIST OF TABLES

ACRONYMS AND SYMBOL LIST

AISI	American Iron and Steel Institute
Al	Aluminum
ASTM	American Society for Testing and Materials
B	Boron
C	Carbon
Cr	Chrome
EDS	Energy Dispersive X-ray Spectroscopy
HPDC	High Pressure Die Casting
HV	Vickers Hardness
HVOF	High Velocity Oxy-Fuel
M	Molybdenum
N	Nitrogen
Ni	Nickel
PVD	Physical Vapor Deposition
QCSM	Quasi-continuous stiffness mode
SEM	Scanning Electron Microscopy
W	Tungsten
XRD	X-ray Diffraction

TABLE OF CONTENTS

1 INTRODUCTION

High pressure die casting (HPDC) is being used by industries due to its high production rate, dimensional accuracy, and small dependency on post-processing of manufactured products. Nonetheless, the costs of maintenance are the main downside of the process. According to Dadić *et al.* (2016), the dies price can reach up to €100,000. Not only is the price exalted due to all the processes involved to make a die, but its lifespan is also short. Many efforts have been put into the study of minimizing the wear processes of dies (BONOLLO *et al.*, 2015; DADIĆ *et al.*, 2016 AND TORRES-GARZA *et al.*, 2014). When the die gets to its end of life, whether it by nucleation of cracks or roughness changes induced by corrosion, industries usually have been recovering it via welding processes. Therefore, it has driven the scientific community to study the effects of welding over tool steels (BORREGO *et al.*, 2009; WANG *et al.*, 2019 AND ZHU *et al.*, 2021). Another process for recovering surfaces is the use of thermal spray techniques. While the use of welding processes for die surface recovery is receiving some attention, the same does not occur for thermal sprays. Although it can be found in the literature, the technique of applying thermal sprays for HPDC has been barely studied, existing only a few studies available in the literature, such as those from Mizuno; Kitamura (2007) and Salman *et al.* (2011). Another advantage of using thermal spray coatings is the coating thickness when compared to other processes. As many studies are focused on the improvement by the development of new materials and thin coatings for HPDC, there is a lack of it as a possible solution for the wear problems concerning HPDC.

There are several mechanisms to which dies are exposed. Induced by use, high pressure die casting dies are exposed in a synergically way to wear, impact, and corrosion at high temperatures. Corrosion is one of the mechanisms which plays a significant role in die wear. The mechanisms of corrosion may vary depending on the scenario. Some of the molten metal corrosion mechanisms were described by Sequeira (2018). The dissolution of the die to the molten aluminum changes the surface quality, both of the die and the final product, and creates a variation of corrosion wear called die soldering. Die soldering occurs due to the corrosion process and formation of intermetallics. The intermetallic material formed during the diffusion acts as a bond between the product and the die. When extracted, the die surface is damaged, affecting

the next run. Although the die soldering phenomenon derives from corrosion, it also depends on the bond force generated by the intermetallic.

This work has the aim of answering how coatings deposited by HVOF behave when exposed to molten aluminum. Two different HVOF coatings were evaluated. The chemical composition of the coatings was chosen based on some criteria. The first coat was made using a powder of AISI H13. The choice of coating the surface with H13 is due to the high performance of this material under high temperature conditions. Also, the high acceptance of this material for die manufacturing makes the deposition of H13 an obvious choice. The second coating was made using chromium carbide in a metallic matrix of NiCr. It was chosen due to its high wear resistance and chemical stability at high temperatures. Soldering and corrosion analyses were done in order to evaluate the surfaces and compare them to AISI H13 and AlCrN PVD. Moreover, improvements could be made by understanding the degradation mechanisms of these coatings.

1.1 Objectives

The main objective is to evaluate the Cr_3C_2 25NiCr and H13 coatings deposited by HVOF thermal spray process as protection layers for high pressure die casting against die soldering and aluminum corrosion and compare them to PVD coating and AISI H13 bare surface.

1.2 Specific objectives

- Understand how the soldering/corrosion mechanism works for each surface;
- Propose improvements for coating processes for AISI H13 tool steel applied to HPDC, based on the analyses of the mechanisms of die soldering and corrosion;
- Development and evaluation of a methodology to perform corrosion/soldering analyses.

1.3 Justification

The use of thermal spray is not restricted only to surface enhancement. When compared to other coatings, such as physical vapor deposition, thermally sprayed

coatings have the advantage of being thicker. As die wear has a magnitude of tenths of a millimeter, thermal spray coatings are suitable for die recovery. Furthermore, HVOF thermal spray has the advantage of spraying several different materials. A thorough study concerning the potential of this technology applied for HPDC could improve the use of this manufacturing process by reducing operational costs.

2 LITERATURE REVIEW

In this chapter, it will be shown a resume of the technical basis utilized to develop the dissertation. It focuses on summarizing the technics used to recover the components, like HVOF, and the possible wear mechanism that these surfaces may be subject to. The general idea is to understand the problem as a whole.

2.1 High pressure die casting

High pressure die casting (HPDC) process has been extensively used to fit the industry demand for productivity. However, productivity is not the only advantage of this process. The high-rate production of metallic parts with outstanding dimensional precision and small dependency on post-processing of the manufactured parts are among the process benefits. Figure 1 shows an overview of the HPDC process, citing the steps for the cyclical process to make the cast part.

Figure 1 - High pressure die casting steps in a casting cycle.

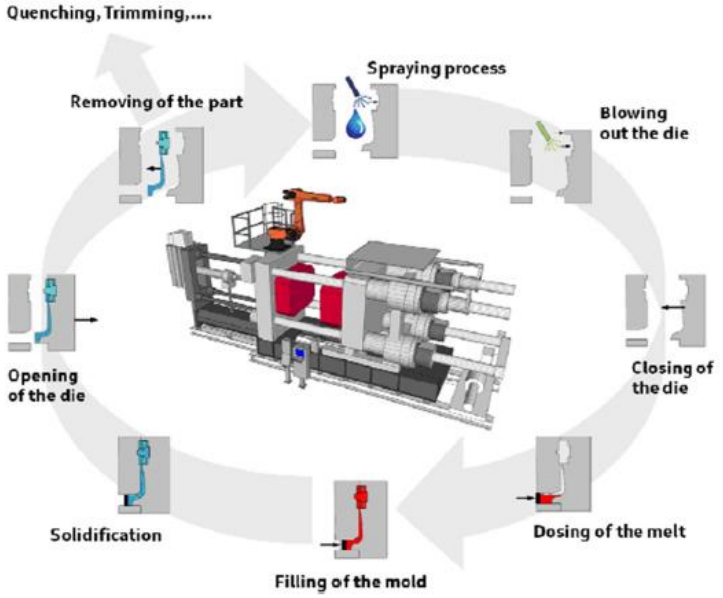

Reference: Bonollo *et al.* (2015)

As low melting point temperature alloys are being widely used, this process fits several production demands. Nevertheless, its use is limited due to high production costs (EUROPEAN ALUMINIUM ASSOCIATION, 2011). Also, according to the European aluminum association, tool costs for die casting are high; thus, large production

quantities are required to justify tooling costs. Otherwise, the use of other processes, like sand casting, is recommended. Even though the investment is lower when compared to other fabrication processes, as shown in figure 2. The tooling cost comes mainly due to the high wear caused by thermal stresses and corrosion caused by the molten metal chosen.

Figure 2 - Relationship between manufactured part cost and investment cost.

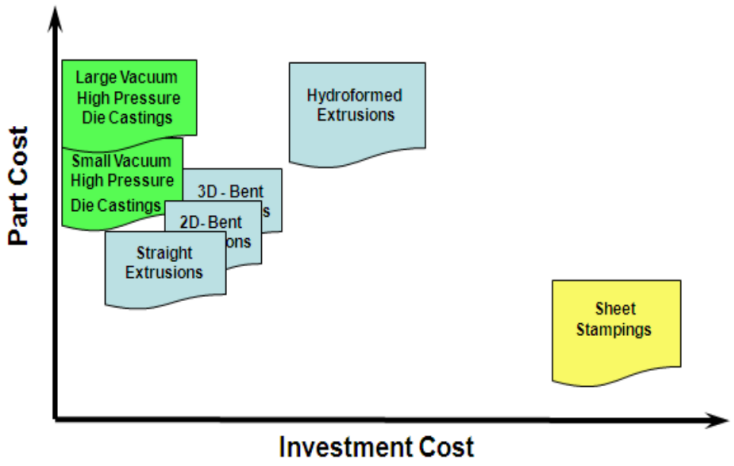

Reference: European Aluminium Association (2011)

One of the various reasons HPDC has a high part cost is die wear. According to Dadić; Živković and Čatipović (2016), dies have a life span of around 100,000 to 120,000 cycles and prices floating between € 30,000 to € 100,000 at LTH Metal Cast, which is a Croatian manufacturer. Therefore, the part cost is one of the main reasons this process may not be chosen for a designed part.

2.2 Tool steels for HPDC dies

High pressure die casting (HPDC) dies nowadays are manufactured with high quality forged steels, generally made of H11 or H13. Cavities are made by electrical discharge machining (EDM) or by high-speed milling (VICARIO *et al.*, 2015). There are several reasons justifying the use of H13, among them the high hardenability, strength, toughness, and softening resistance (NING *et al.*, 2019). A study executed by Riccardo *et al.* (2021) revealed a similar behavior of H11 and H13 regarding fatigue under isothermal temperatures. The chemical composition of H11 and H13 is shown in table 1.

Table 1 - AISI H11 and H13 tool steels chemical composition.

Tool Steel	C (wt%)	Si (wt%)	Mn (wt%)	Cr (wt%)	Mo (wt%)	V (wt%)
AISI H11	0.38	1.10	0.40	5.0	1.3	0.4
AISI H13	0.38	1	0.40	5.0	1.3	0.9

Reference: Riccardo *et al.* (2021)

According to Persson (2003), hot work tool steels are classified as either chromium (H10-H19), tungsten (H21-H26), or molybdenum (H42-H43), according to the main alloying element. Moreover, alloying with vanadium improves the high temperature wear since the vanadium carbide is the hardest of all carbides, whereas the oxidation resistance of tool steels is improved by alloying with higher levels of silicon. The tungsten and molybdenum hot work tool steels have higher temper resistance and hot hardness than chromium hot work tool steels.

2.3 Corrosion process caused by molten metal

Molten aluminum can cause high-rate corrosion of container materials, leading to an insufficient and, above all, unpredictable lifetime. The tolerance of aluminum alloy castings may be affected by the wear of dies caused by aluminum flow (SEQUEIRA, 2018). There are several kinds of corrosion, and for molten metals, a few mechanisms are known. Some of these mechanisms are discussed below.

2.3.1 Simple dissolution in molten metal

Sequeira (2018) stated that simple dissolution has not been properly explained yet. It is known that the relationship is strongly based on the solute due to its lattice energy. Figure 3 shows an approach to study simple dissolution phenomena. The system can be divided into hot and cold legs, throughout the molten metal flows. When the molten metal passes inside the corrosion coupon after the hot leg, a solution of molten metal and coupon material is made. After being cooled, the solution passes through the coupon after the cold leg, and the nucleation of the solute occurs due to the temperature change.

Figure 3 - Stages in thermal-gradient mass transfer during simple dissolution analysis.

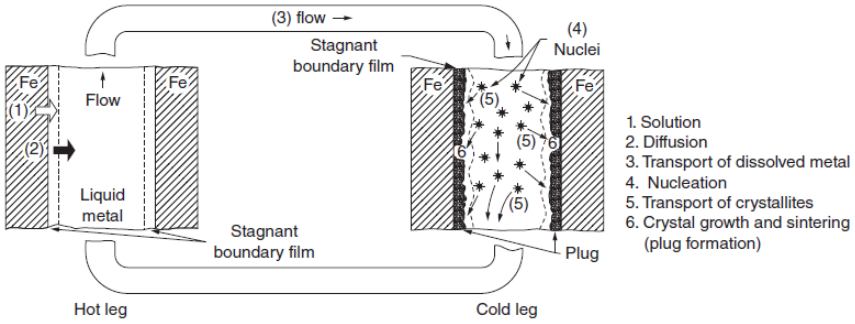

Reference: Sequeira (2018)

As stated by Zhu (2014), the dissolution process is a phenomenon that combines corrosive, erosive, and chemical reactions. Physical wear mechanisms can detach small particles from the surface, and the liquid metal flow is capable of acting as a solvent. Dissolution may also be diffusion controlled, and according to Zhu *et al.* (2004), it can be described by the equation (1). Furthermore, the dissolution rate is strongly influenced by dynamic agitation.

$$\frac{dC}{dt} = D\frac{1}{\delta}\frac{s}{v}(C_s - C) \quad (1)$$

Where

C – Concentration of the dissolved metal;

C_s – Saturation concentration;

t – Time;

D – Diffusion coefficient of the dissolved metal;

δ – The thickness of the diffusion boundary layer;

s – The specimen surface area;

v – Melt volume.

2.3.2 Intermetallic formation

Another corrosion mechanism is alloying between the molten metal and the solid metal. To understand how allowing corrosion works, it is necessary to comprehend how phase diagrams work. Figure 4 shows a binary diagram of Fe-Al. It is

possible to observe the high solubility iron has in aluminum. Therefore, many phases are stable throughout the range of solubility. According to Sequeira (2018), a degree of solubility is demanded for alloying corrosion. The result of this type of corrosion is the formation of intermetallics.

Figure 4 – Binary phase diagram of Fe-Al.

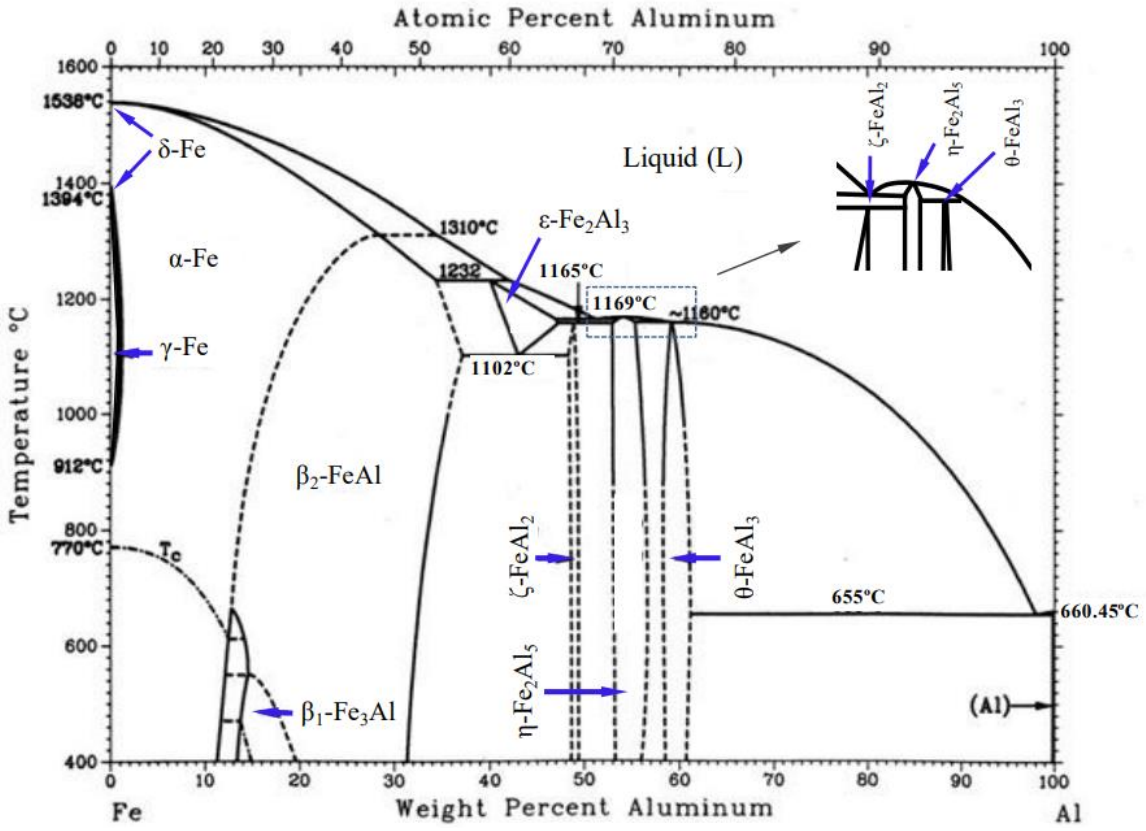

Reference: Sidhu (2012)

Furthermore, by knowing the temperature of the process, it is possible to cross a line on the diagram and have an idea of the possible phases that will be found in a molten metal corrosion scenario. According to Hugh Baker *et al.* (1992), phase diagrams give an indication of which phases are thermodynamically stable; however, nonequilibrium conditions are usually found in practice. Even though, phase diagrams are a powerful tool to investigate attacking service problems, such as hot corrosion.

2.3.3 Diffusion

The main driver of corrosion mechanisms in molten metal is diffusion. Whereas the study of phase transformations is concerned with stable or equilibrium

arrangements of atoms in an alloy, diffusion is what controls the rate at which many transformations occur. The reason why diffusion occurs is always so as to produce a decrease in Gibbs free energy (PORTER *et al.*, 2009).

Fick's first and second laws describe the diffusional process. The first law assumes diffusion as a time-dependent process (Steady-state diffusion), whereas the second law considers that the diffusion flux and the concentration gradient at some particular point in a solid vary with the time (Nonsteady-state diffusion) (CALLISTER; DAVID, 2014).

There are some mechanisms in which diffusion occurs. The most common mechanisms are substitutional and interstitial diffusion. A general case of diffusion for a nickel and copper couple is shown in figure 5. According to Porter *et al.* (2009), substitutional diffusion occurs when the atom oscillates through a certain amplitude at a defined frequency. The mean vibrational energy is increased by temperature increasement. As the mean frequency remains the same, the amplitude is increased. Normally, the movement is limited by a neighbor atom. However, if the site is vacant, an abnormal jump may put the atom into the vacancy. Therefore, the rate at which any given atom diffuses will depend on the available vacancies. Both the probability of jumping and the concentration of vacancies are strongly influenced by temperature.

Regarding interstitial diffusion, the atom needs to be small enough to occupy the interstitial sites, as solute the atom uses the interstitial sites to travel. According to Porter *et al.* (2009), the atom can jump to another position as much as its thermal energy permits it to overcome the strain energy barrier to migration. As the solute concentration is usually small, the atoms are surrounded by empty interstitials, and therefore the interstitial diffusion occurs much more rapidly than diffusion by vacancy mode.

Figure 5 - (a) A copper–nickel diffusion couple after a high-temperature heat treatment, showing the alloyed diffusion zone. (b) Schematic representations of Cu (red circles) and Ni (blue circles) atom locations within the couple. (c) Concentrations of copper and nickel as a function of position across the couple.

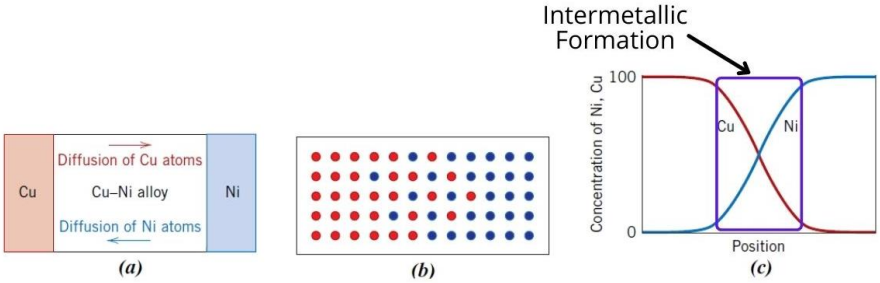

Reference: Adapted from Callister; David (2014)

2.4 Die soldering caused by molten metal

Another wear phenomenon that occurs in the HPDC process is soldering. Die soldering occurs when the molten melt, usually aluminum, solidifies and “sticks” on the surface. This phenomenon is also called die sticking. The molten metal is injected into the die and solidifies. Because of the high temperature and pressure of the process, the molten metal diffuses into the die and vice versa. After cooling, the cast product is extracted from the die. Due to the bonding between the surfaces caused by intermetallic formation, both die and cast surfaces are prone to surface damage. When another cycle of the casting occurs after the soldering, the damaged surface of the die increases the chances of soldering. Die soldering causes not only dimensional problems but also strength issues. Depending on the detached volume material and the region where it comes from, this defect may cause stress concentration, leading to premature failure. Photograph 1 shows an example of soldered aluminum on a die surface. The white arrows show the defects caused by soldering.

Photograph 1: Practical example of die soldering wear on a die surface.

Reference: Pukasiewicz (2021)

There are several mechanisms whereby soldering is generated. Song *et al.* (2012) have studied the soldering mechanisms of AISI H13. They proposed a sequence of the soldering formation for AISI H13 coated with CrN and exposed to molten A380 aluminum alloy at 660 °C, as shown in figure 6. The corrosive process which causes soldering is generated by the incubation of pits after coating failure. As the exposed AISI H13 surface is prone to the intermetallic formation, the pit starts to grow. The pits start to bond, and a curly surface is generated.

Figure 6 - Steps of soldering process (I to X) for surface coated with CrN by PVD. Local coating failure (I to II), pit formation (III to V), in-depth growth of a pit (VI to VIII), pit connection (IX to X), and formation of negative draft (X).

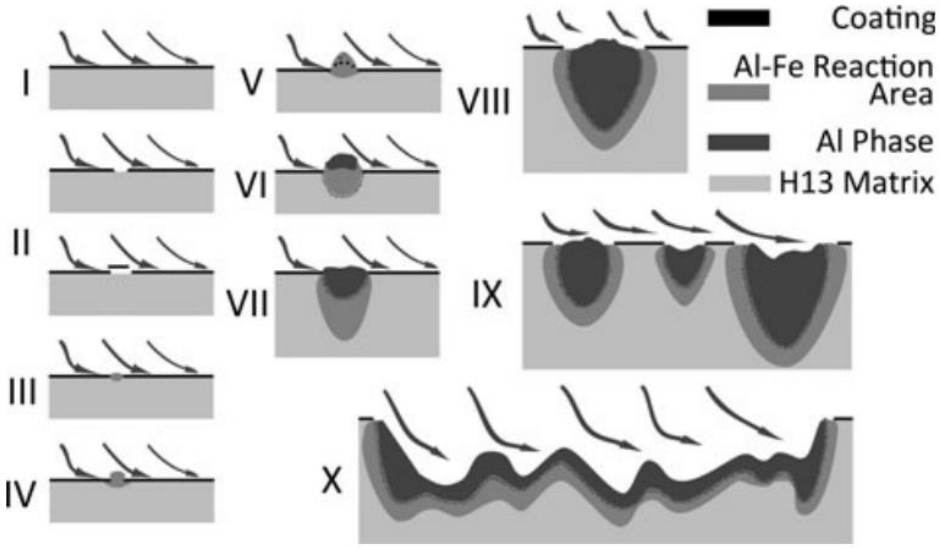

Reference: Song *et al.* (2012)

During die casting processes, dies are protected by a lubricant layer, and die soldering cannot easily occur. Nonetheless, defects in the lubricant coating caused, for instance, by hot spots, expose the die to molten metal. High temperatures induce diffusion of the molten metal to the die surface and vice versa. As the number of cycles increases, the aluminum content diffused into the die increases. After the growth of the intermetallic layer, the harsh environment causes the detachment of these intermetallic and causes micro holes. These micro holes will be expanded by erosion of the molten metal. That way, the contact surface increases to a point where physical-chemical soldering occurs (ZHU *et al.*, 2001). This phenomenon is shown in figure 7.

Figure 7 - Surface soldering due to failure of the lubricant.

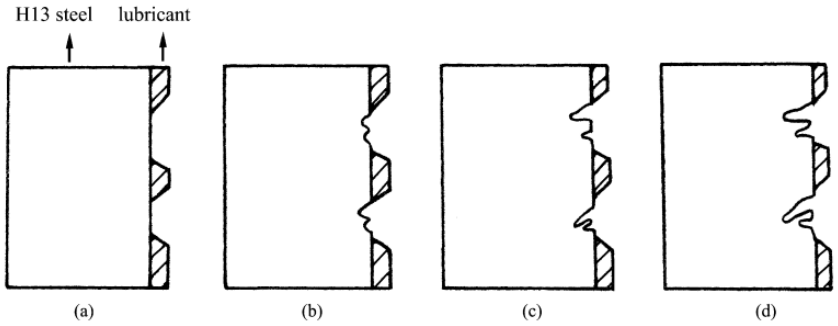

Reference: Zhu *et al.* (2001)

Another critical variable is the surface finish. Gobber *et al.* (2018) studied the effects of the surface roughness regarding soldering with the use of lubricant. They found an optimized spot around 0.8 R_a, and smaller values increased the soldering probability. They justified the increase in soldering due to the poorer wettability of the sprayed lubricant. In another study, Gobber *et al.* (2019) analyzed how the surface finish changes the contact angle with the lubricant and creates failures in the coating, as shown in figure 8.

Figure 8 - Lubricant adhesion for polished and micro sandblasted (rough) surfaces.

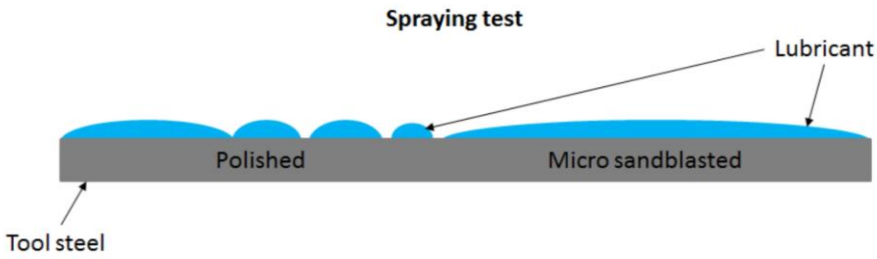

Reference: Gobber *et al.* (2019)

2.5 Thermal spray processes

Thermal spraying is a group of processes where a feedstock material is heated to create molten or semisolid particles. These particles are accelerated towards a surface to create a coating. When hitting the surface, the particles build a coating by spreading and solidifying on the surface, creating strong adhesion forces. Figure 9 shows the main steps of these processes.

Figure 9 - Steps of a thermal spray process.

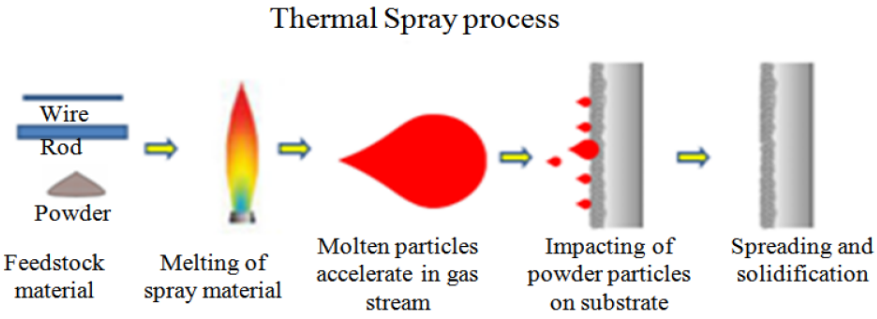

Reference: Kumar *et al.* (2019)

According to Vardelle *et al.* (2016), thermal spray processes are being regarded as an environmentally friendly technology. It is because thermal spraying is used not only to improve surface resistance but also to recover worn components. Another example indicated by Vardelle *et al.* (2016) was the use of thermal spray technology to replace hard chrome coatings with “greener” thermal spray coatings. As thermal spray coatings have a considerable thickness, their use is not limited only to surface enhancement; it may also be used as an additive geometry process. In figure 10 (a) it is shown the structure of a thermally sprayed coating. The structure of the coating depends on the process parameters, the chemical composition of the feedstock material, and the thermal spray process. In figure 10 (b) it is possible to observe the main bonding mechanisms by which thermally sprayed coatings adhere to the surface.

Figure 10 - Structure of (a) thermally sprayed coatings and (b) bonding mechanisms.

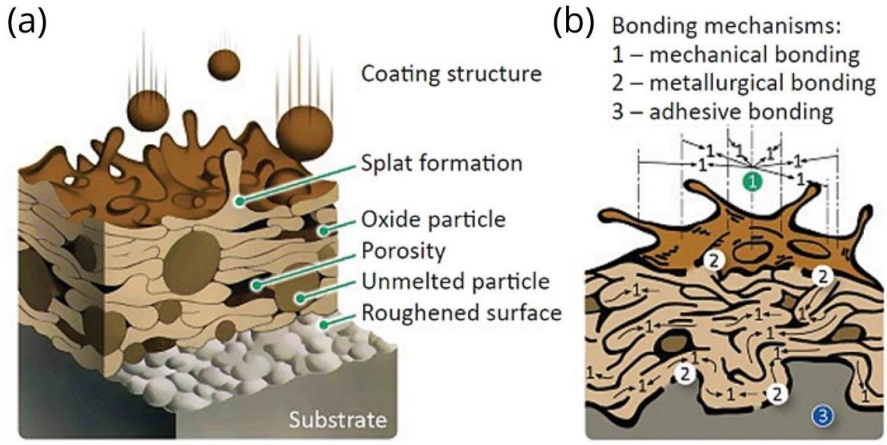

Reference: Kandeva *et al.* (2016)

There are several techniques throughout the coating can be tailored. Depending on the powder composition and desired characteristics, a certain process may be the most suitable one. Some processes are shown in figure 11.

Figure 11 - Comparison of various thermal spray processes in terms of velocity and temperature.

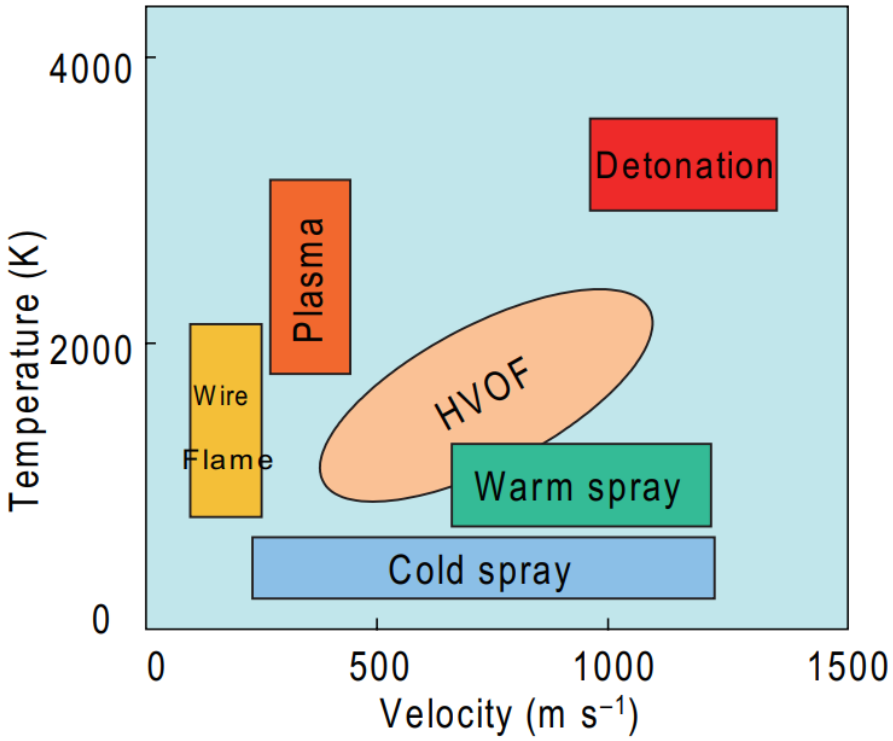

Reference: Kuroda *et al.* (2008)

According to Berger (2014), choosing the right process is critical for the use of thermal spray as a solution. The range of values for a given property is significantly

large for thermally sprayed coatings and diverges from bulk materials with the same chemical composition. It is due to phase transformation and imperfections caused during the deposition process. Also, as the particles reach high temperatures along the process, corrosion products play a big role in coatings mechanical properties.

Among the thermal sprays processes, the main performance of the deposits applied by the high velocity oxygen fuel process is superior to other thermal spraying methods. HVOF spraying is also compatible for applying coatings of materials such as cemented carbides (GHADAMI; AGHDAM, 2019). Figure 12 represents the process for tailoring HVOF coatings. A convergent-divergent nozzle is used to transform pressure energy into velocity energy. The particles are accelerated in the combustion chamber and sprayed towards the substrate. Gas or liquid fuel can be used, and a large variety of powders can be applied. According to El-Eskandarany (2020), HVOF has been receiving great attention as one of the most powerful techniques to deposit fine powder particles on substrates of different types of material.

Figure 12 - HVOF coating process.

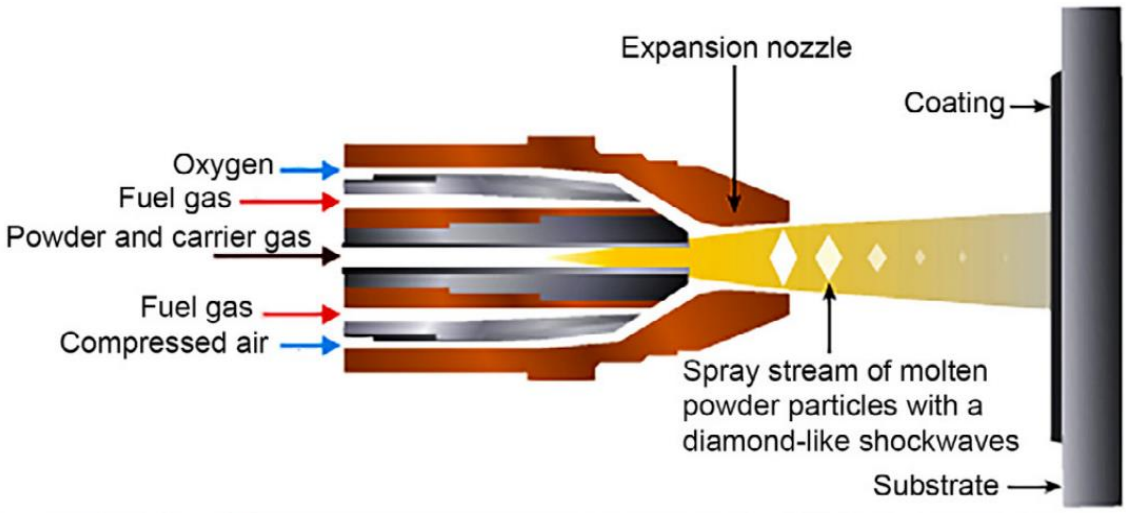

Reference: Adapted from El-Eskandarany (2020)

2.6 Coatings for surface enhancement

There are several studies applied to thermal coatings for a variety of applications. Some characteristics such as coating adhesion, percentage of oxides/porosity, and chemical composition will determine how the coating behaves under stress. A plethora of coatings and materials are available for scenarios where it is required

physical and/or chemical protection (FOTOVVATI *et al.*, 2019). A few types of coatings are discussed below based on their main composition.

2.6.1 Molybdenum boride

As discussed before, there are many wear mechanisms in HPDC. Some studies have brought as solution coatings based on molybdenum boride (MoB) in a cobalt-chrome matrix. The central reason is the close thermal expansion coefficient to the alloys utilized to manufactory dies, as in the case of AISI H13. Mizuno and Kitamura (2007) studied molybdenum boride using a rotational immersion test in molten Al-45wt.%Zn at 900 K. They came to the conclusion that the MoB-based coating has excellent durability in molten Al-rich Al-Zn when compared to WC, Al_2O_3, and ZrO_2 coatings. Mizuno and Kitamura attributed the high resistance of the MoB/CoCr coatings not only to its physical characteristics, such as low porosity and high hardness but also to its chemical resistance, evaluated by the immersion test. For depositions on AISI 316L, it was necessary a bond coating to match the same resistance degree due to the different expansion coefficient.

MoB-based coatings were also analyzed by Khan *et al.* (2011). They compared MoB coatings using CoCr and NiCr as the metallic matrix. Figure 13 shows the results for 25 hours of immersion test in molten aluminum alloy (ADC-12) at 680 °C. As a comparative, it was used SKD61, similar to AISI H13. It is possible to observe the strong resistance the coatings exhibited when compared to bare substrate, using radius reduction as a comparison parameter.

Figure 13 - Reduction ratio of coating thickness during 25 h immersion test molten aluminum alloy (ADC-12) at 680 °C.

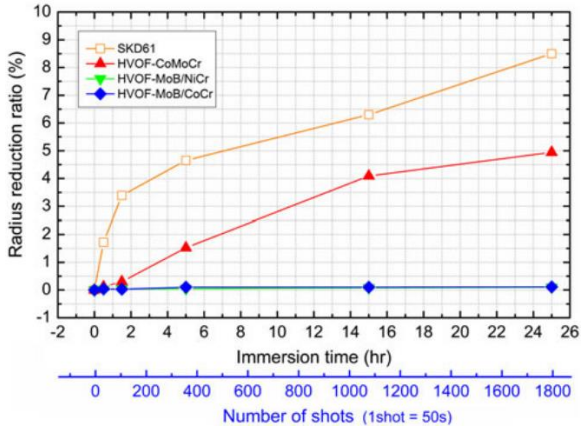

Reference: Khan *et al.* (2011)

2.6.2 Titanium aluminide

Other materials that have been studied in order to coat high pressure dies are titanium aluminides (Ti_3Al, TiAl, and $TiAl_3$). Compared to titanium, these aluminides show some advantages such as higher elastic modulus, lower density, in general higher corrosion resistance, and better behavior under higher temperatures (SALMAN *et al*, 2009). A study by Salman (2011) has shown the efficiency of these coatings to delay the molten aluminum dissolution. Salman has used $Ti(Al,O)/Al_2O_3$ to coat the surface by the HVOF method. Figure 14 and figure 15 show the AISI H13 and coated AISI H13, respectively. It is possible to observe how the coating preserved the geometry of the specimen.

Figure 14 – Photographs of uncoated H13 tool steel coupons after (a) one hour, (b) six hours, (c) 22hours, and (d) 38 hours of immersion in molten aluminum at 700 °C.

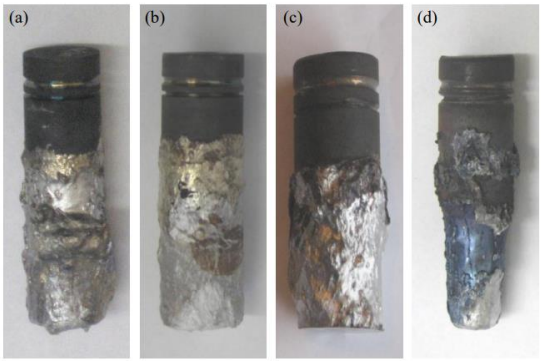

Reference: Salman (2011)

Figure 15 - Photographs of $Ti(Al,O)/Al_2O_3$ coated coupons after (a) one, (b) three, (c) six, (d,e) 22, and (f) 38 hours of immersion in molten aluminum at 700 °C

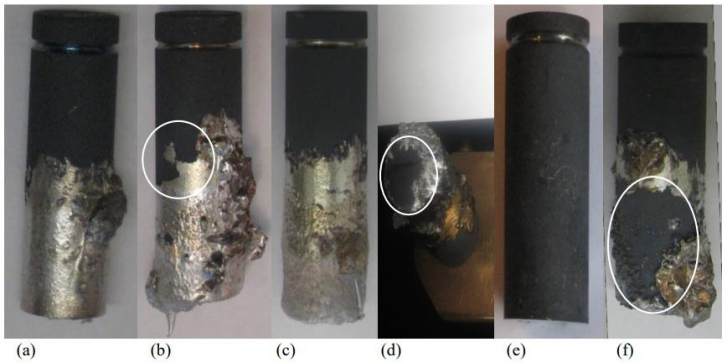

Reference: Salman (2011)

2.6.3 Carbides

Chromium carbide is one of the most popular HVOF coatings studied by literature. Chromium carbides are not only hard but also keep their properties under high temperatures (CHATHA *et al.*, 2012). Usually, it is mixed in a NiCr matrix to create an adhesive coating. There are not enough studies about the use of these materials for the improvement of surfaces exposed to molten metals.

Picas *et al.* (2015) analyzed the use of Cr3C2–CoNiCrAlY coating with a CoNiCrAlY bond coating. The idea was to decrease the fast change of the thermal expansion coefficient from the bulk to the coating, diminishing the thermal stress by using the bond coating. Besides, Picas *et al.* (2015) used a surface heat treatment and obtained a grain refinement on the surface, reaching higher hardness. In the end, Picas *et al.* (2015) suggested the use of these coatings where high temperatures and wear resistance are required, as tooling and high temperature dies. Furthermore, Bolelli *et al.* (2016) measured the thermal expansion coefficient for Cr_3C_2 25NiCr HVOF coating and found it to be 11.08×10^{-6} $°C^{-1}$ in the 30–400 °C range. This result is close to the AISI H13 tool steel. Even so, the literature lacks the analysis of these coatings regarding the molten aluminum chemical attack.

As well as chromium carbide, tungsten carbide (WC) has been wildly used as coatings for several demands. The main reasons are its hardness, wear resistance, and toughness. López and Rams (2015) studied a WC-12Co coating in order not only to enhance the wear resistance of the bulk but also to evaluate the effect of molten metals on the surface. Besides showing weak adhesion with aluminum, the WC-12Co coating improved the corrosion resistance during thermal fatigue tests. After the thermal cycling test, they did not find cracks or delamination.

Singh and Kaur (2019) studied the addition of WC-Co in NiCrSiFeBC powder for HVOF coatings. This composition kept its resistance even under 400 °C. A leading issue with WC-based coatings is dealing with higher temperatures and keeping its mechanical properties. According to Oerlikon Metco (2014), for its Amdry 5843 and WOKA 3903, the maximum working temperature is 500 °C. In case of higher temperatures, it is recommended the use of biceramics, as the mixture of WC and Cr_3C_2, for instance.

Generally, WC-based coatings are inclined to be more resistant and harder than Cr_3C_2-based ones. However, the maximum service temperature for these coatings is

around 500 °C. A potential solution is to combine these carbides to create a more resistant coating as well as minimize high temperatures wear. Zhou *et al.* (2017) studied these coatings behavior and its temperature relationship. Even for the highest temperature studied by them, 650 °C, the addition of tungsten carbide increased the wear resistance. However, the wear rate for the Cr_3C_2-NiCr did not significantly change by increasing the temperature, whereas the Cr_3C_2-WC-NiCoCrMo has almost doubled the wear rate from 450 to 650 °C.

There still are no deep studies of these coatings for molten aluminum alloys. Nevertheless, Cr_3C_2, WC, and its combination show promising properties for this application.

2.6.4 Boron nitrides

Some studies have analyzed the deposition of hexagonal boron nitride by HVOF in reason of its hydrophobic behavior with molten aluminum (FUJII *et al.*, 1993). Besides, h-BN coatings have great thermal shock resistance, high thermal conductivity, and good chemical inertia (ZHANG *et al.*, 2015). As it is a self-lubricant material, its application creates advantages in environments where grease and oil cannot be used (DONNET; ERDEMIR, 2004). Despite its great surface and chemical characteristics, Zhang *et al.* (2015) deposited h-BN with a nickel-based matrix and did not achieve high hardness. This happens due to the low h-BN concentration in the coatings, by increasing the h-BN concentration, Zhang *et al.* (2015) have observed delamination.

Shivalingaiah *et al.* (2020) used cubic boron nitride (c-BN) with Inconel 718 matrix for surface coating and achieved a hardness of about 500 HV. In spite of c-BN coatings having a higher hardness, some characteristics as being a self-lubricant material are lost.

2.6.5 Oxides

Several oxides are available for deposition using thermal sprays. Among them, zirconium oxide exhibits excellent properties to handle molten materials. Peter *et al.* (2015) compared zirconium oxide-based and nickel-based coatings to protect AISI H11 bulk. For zirconium oxide-based (ZrO2–Y2O3 and ZrO2–MgO), a NiCoCrAl bond coating was used to enhance corrosion resistance under high temperatures. Nevertheless, for thermal fatigue tests, the nickel-based coating showed to be more efficient. Both

cases did not show expressive aluminum dissolution; the predominant wear mechanism was stress generated by thermal cycling, which caused cracks and delamination. One of the main reasons zirconium oxide has excellent resistance to molten aluminum is its poor wettability. Yang *et al.* (2016) found a contact angle of 148° for ZrO_2 plates. As the wettability is limited, the chemical reactions are retracted.

Usually, coatings based on ZrO_2 are used in environments where temperatures are high and low thermal conductivity is required. A classic example of its use is as thermal barrier coating. According to Takahashi *et al.* (2019), a thermally grown oxide (TGO), usually alumina-based, is used to improve the effective adhesion between the bond coating and the top coating.

Liu *et al.* (2003) have worked on alumina/titania coatings deposited by HVOF and plasma-sprayed. The HVOF coating showed to be extremely dense, adherent, and wear resistant. Generally, alumina coatings are not suitable for corrosion enhancement. However, the improvement in the density of these coatings has changed their poor corrosion protection by decreasing its permeability (PINZÓN *et al.*, 2018).

Abu-warda *et al.* (2019) analyzed coatings made of Al_2O_3-NiAl deposited by HVOF regarding corrosion and wear under high temperatures. It was possible to obtain good adhesion, with no substrate degradation in thermal fatigue analyses even under 850 °C, although having coating degradation.

2.6.6 Physical vapor deposition

Physical vapor deposition (PVD) is a technique that uses heat, usually from a cathodic arc, to vaporize a solid target in a vacuum and deposits the atoms on the surface. Gulizia *et al.* (2001) showed the improvements achieved by PVD coatings regarding soldering. It was found that the coating did not chemically react with the aluminum. Nonetheless, the soldered area grew in percentage over the cycles. A study performed by Lugscheider *et al.* (1998) compared an H11 substrate after nitriding and several PVD coatings using the polarization technique in die lubricant as environment. The authors reached the conclusion that PVD coatings showed a lower current density and, therefore, diminished the corrosion rate of the samples.

PVD coatings are also widely used due to its high hardness, wear resistance, and corrosion resistance, enabling surfaces to improve their performance (LIU *et al.*,

2012). The characteristics of these coatings make them one of the most common surface enhancements for the HPDC application (KOVAČEVIĆ *et al.*, 2018).

According to Gilewicz *et al.* (2019), AlCrN is one of the most promising PVD coatings. It is because of its high wear resistance by the formation of permanent oxide layers on the worn surfaces. There are two expected aluminum nitrides: c-AlN and h-AlN (Cubic and hexagonal lattice, respectively). Also according to Gilewicz *et al.* (2019), the increase in aluminum promotes the formation of the hexagonal phase, as h-AlN is more stable, reducing the hardness and leading to drastic degradation in strength. The typical cross-sectional TEM image of an AlCrN coating made by Wu *et al.* (2015) is shown in figure 16. It is possible to observe the formation of AlN and CrN phases in alternated distribution with modulation of 18 nm and the presence of CrN layers containing a larger number of particles with 0.5 – 3.0 nm in diameter.

Figure 16 - Magnified TEM image of a typical cross-section from AlCrN coating.

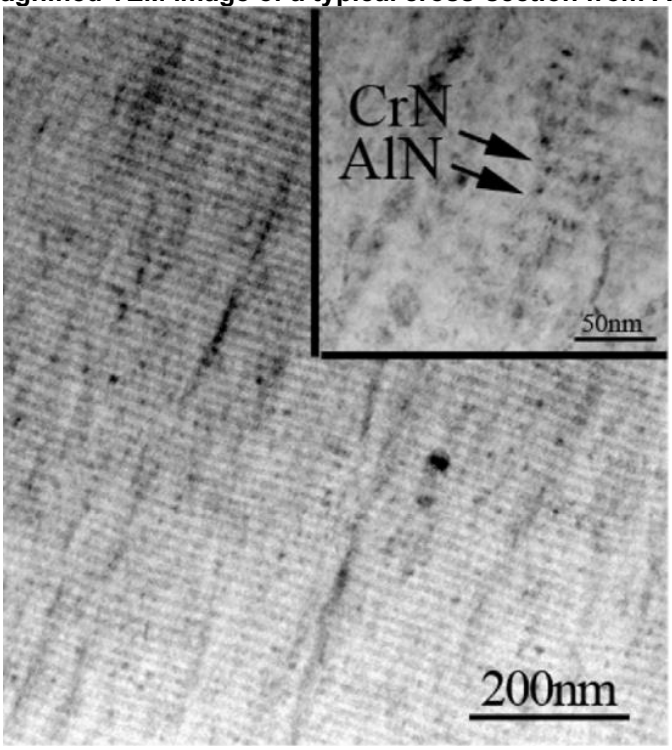

Reference: Adapted from Wu *et al.* (2015)

2.7 Corrosion in molten aluminum tests

Several processes of corrosion in molten metal were described by Zhang and Chen (2015). Most of the equipment described by Zhang and Chen involved the use of rotational samples. A similar equipment was used by Zhu (2014), figure 17, to evaluate several materials regarding corrosion resistance; by changing the temperature of

the molten aluminum, time of exposition, and angular velocity, it was possible to compare several materials with the H13 tool steel.

Figure 17:Rotation test setup. (1) Spindle, (2) sample, (3) crucible containing the molten aluminum and (4) frame structure.

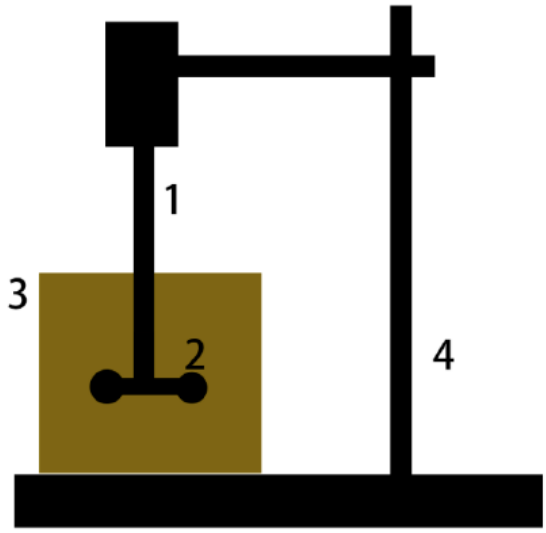

Reference: Zhu (2014)

A different system was used by Salman (2011) to evaluate HVOF coatings. The corrosion results found by Salman were shown in figure 14 and figure 15. Salman used a quiescent corrosion analysis by exposing the specimen to molten aluminum and recording photographs over time. A similar analysis was made by Chen *et al.* (2020). In both studies, the samples were cleaned with NaOH solution before measuring the mass change.

2.8 Soldering in molten aluminum tests

Terek *et al.* (2019) have proposed an ejection test to evaluate soldering effects. They analyzed three different ways to pour the aluminum and found different ejection forces. The methods evaluated by Terek *et al.* are shown in figure 18. The first and second methods are similar, they change with regard to the moment when the aluminum is poured into the crucible. The third analyzed method uses a preheated system. They found the second method to have a smaller coefficient of variation. Another similar methodology was proposed by Fazlalipour *et al.* (2019). They designed pins to evaluate H13 tool steel and proposed the use of nano-composite and nano-multilayer thin films.

Figure 18: Three different methods of pouring the aluminum to evaluate ejection forces.

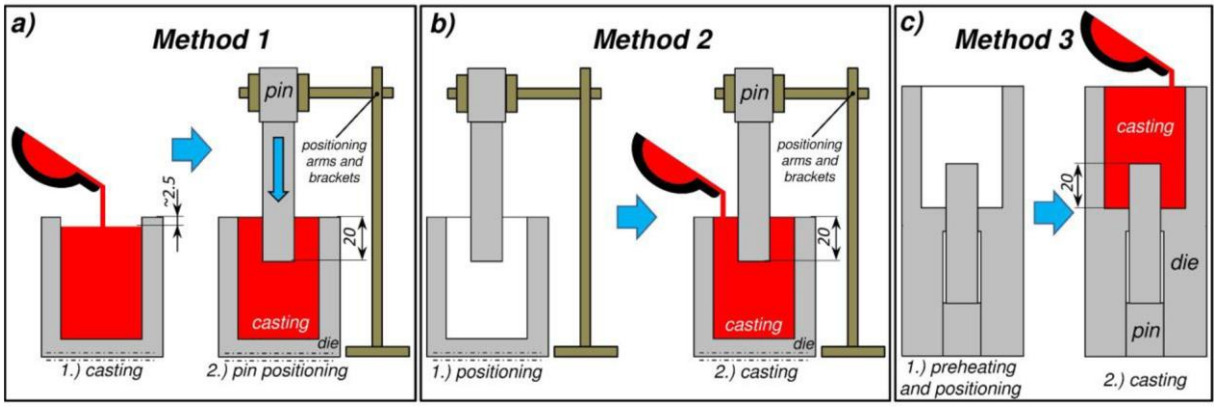

Reference: Terek *et al.* (2019)

Wang *et al.* (2016) proposed a different methodology. Instead of using a pin cast into the aluminum, they cast the pin on a flat surface, as represented in figure 19. First, the boron nitride tube was preheated along with the molten aluminum at 700 °C. After that, the coupon was placed inside the furnace, and the boron nitride tube was positioned on it. The molten aluminum was then poured, and the system was kept inside the furnace for about 15 minutes.

Figure 19: Tensile test proposed by Wang *et al.* for evaluating soldering.

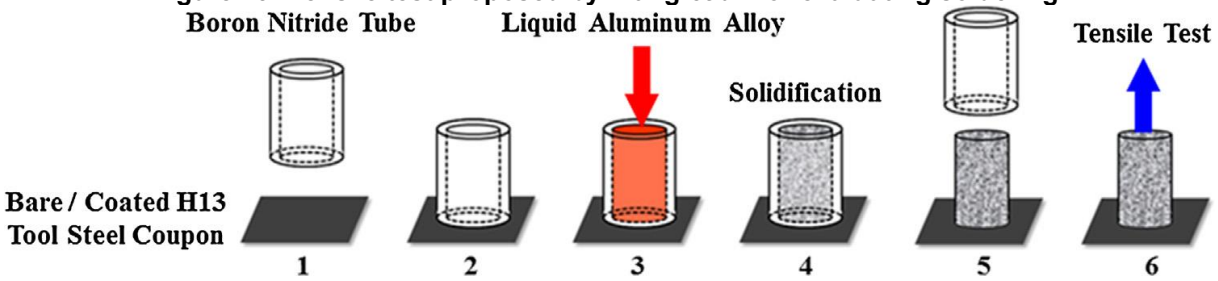

Reference: Wang *et al.* (2016)

3 MATERIALS AND METHODS

Corrosion and soldering analyses were performed to evaluate the resistance of the coatings. The A383 (ADC12) aluminum alloy was used for all tests involving molten aluminum. The composition of the alloy is shown in table 2. Before any test involving molten aluminum, the surface of the samples was prepared using sandpaper to achieve a R_a of 0.8 ± 0.2 µm. For corrosion and soldering, samples were machined according to the requirements of the analyses, which will be discussed later. For metallography, sheets of 3/16” x 1” x 6” were used for HVOF and cylinders of 1” diameter and 1/2” height for physical vapor deposition.

Table 2 - Chemical composition of the A383 aluminum alloy (in wt.%).

Alloy	Al	Si	Cu	Zn	Fe	Mg	Mn	Ni
A383	Bal.	10.5	2.5	1.5 (Max)	1.0 (Max)	0.4 (Max)	0.5	0.3

Reference: Liu *et al.* (2020)

The flowchart in figure 20 summarizes the proceedings for the study of the coatings.

Figure 20 - Flowchart of the experimental procedure for characterization of the coatings.

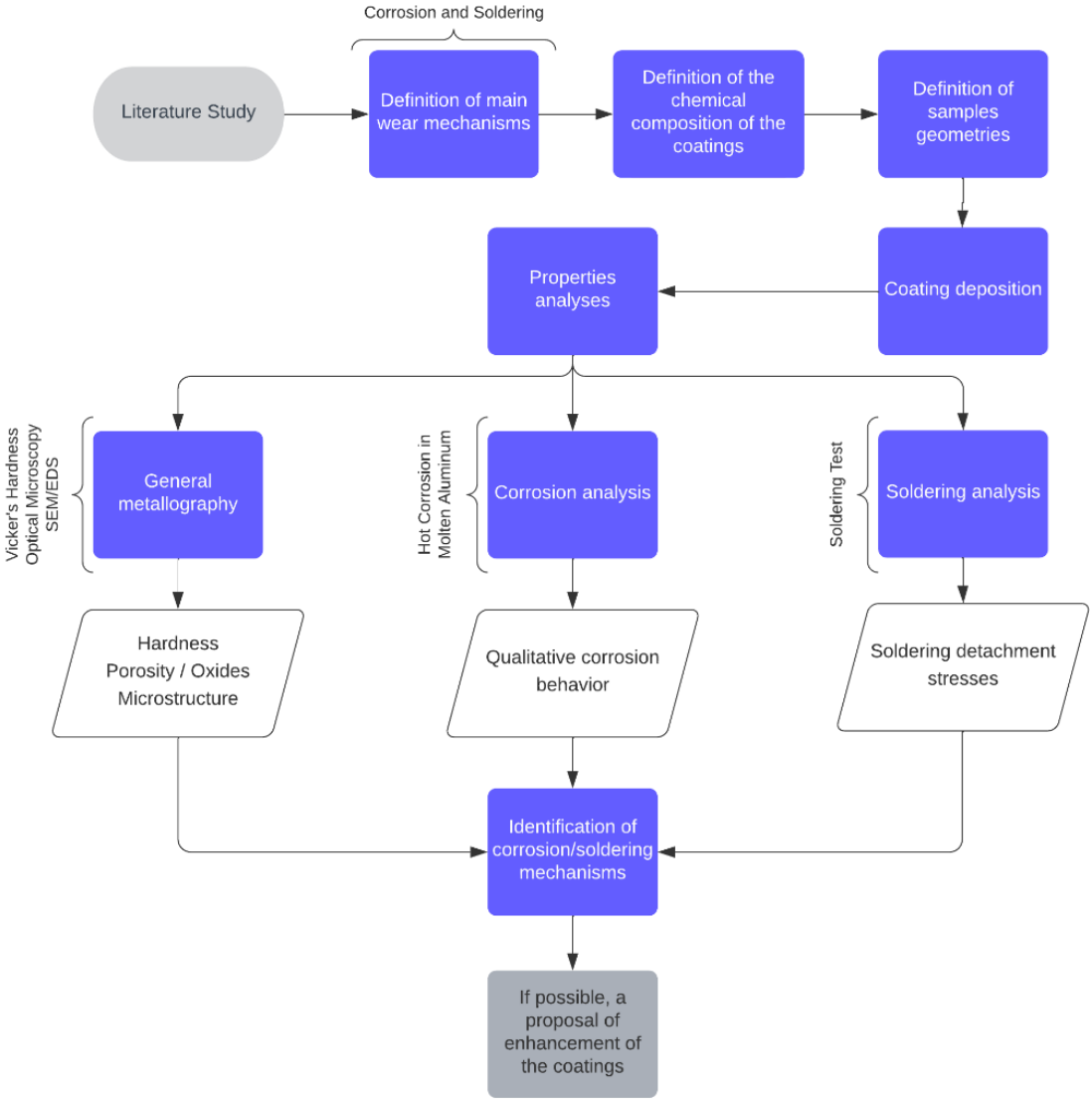

Reference: Author

3.1 Tool steel AISI H13 substrate

The AISI H13 was received as normalized, provided by Villares Metals. Before any coating process, substrates were quenched in the air at room temperature after 1 hour at 1020 °C and double tempered at 620 °C for 2 hours for each temper. A machining allowance of 1 mm was used, and the surface was machined to final dimensions before analyses and surface coating to avoid dealloying caused by oxidation.

3.2 High velocity oxygen fuel (HVOF) deposition

Samples were coated with AISI H13 and Cr_3C_2 25NiCr by HVOF to evaluate corrosion resistance in molten metal. The spraying parameters are shown in table 3.

Before the coating process, the samples were blasted using Al_2O_3 to achieve a rough and clean surface. The coatings were deposited on AISI H13 quenched and double tempered.

Figure 21 shows images of the powders utilized. Both powders present a spheroidal morphology. The MetcoAdd H13-A powder is obtained by gas atomization (Argon), whereas the WOKA 7205 was agglomerated and sintered.

Table 3 - Parameters and powder for HVOF deposition.

Parameter	Cr_3C_2 25NiCr	AISI H13
Oxygen flow	1950 l/min	1950 l/min
Nitrogen flow	23 l/min	23 l/min
Kerosene	56 l/min	56 l/min
Spray Distance	381 mm	381 mm
Gun	JP5000	JP5000
Powder	WOKA 7205	MetcoAdd H13-A

Reference: Author

Figure 21 - SEM images of (a) H13 powder and (b) its cross-section, (c) Cr_3C_2 25NiCr and (d) its cross-section.

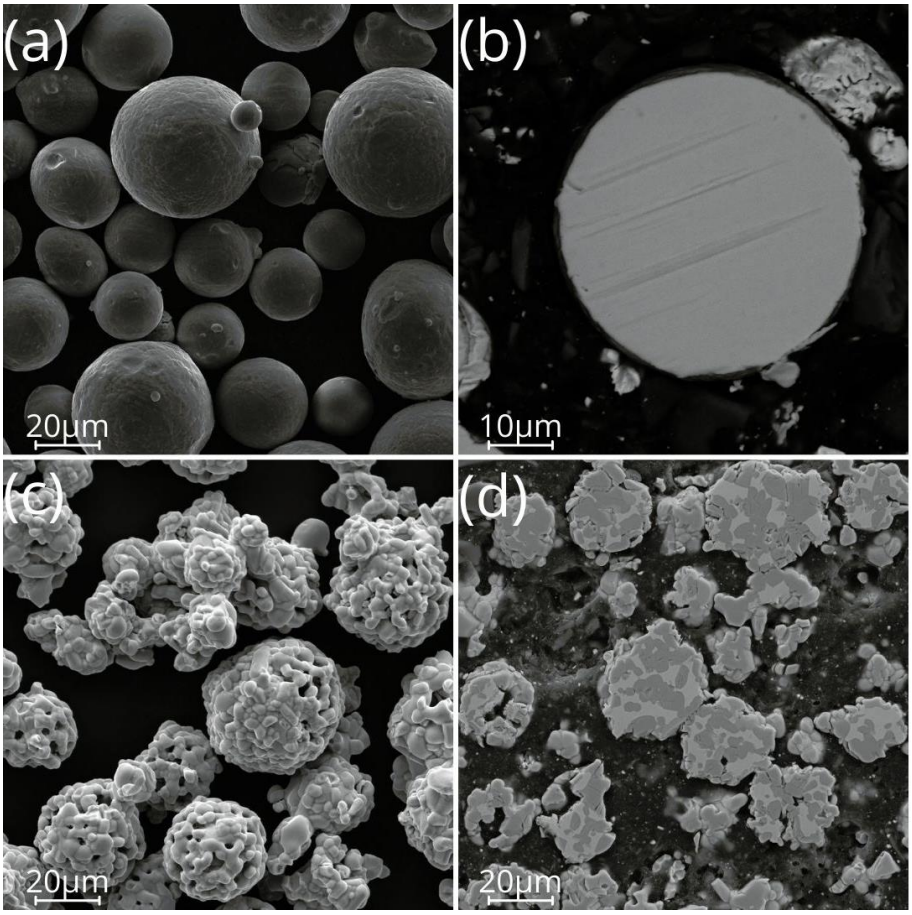

Reference: Author

3.3 AlCrN coating deposition

Physical vapor deposition was made using Balinit Alcrona from Oerlikon Balzers. It was also deposited by Oerlikon Balzers in São José dos Pinhais – PR, Brazil. Before depositing the AlCrN PVD coating, the surface was polished to an average surface roughness (Ra) of 0.1 µm or below. A similar process was used by Biava (2019). The parameters for the deposition are shown in table 4.

Table 4 - Parameters for AlCrN deposition via PVD.

Parameter	AlCrN
Reactive Gas	Nitrogen
Nitrogen deposition pressure (Pa)	3.5
Target Power (kW)	3.5
Substrate bias voltage (V)	-40 to 170
Substrate temperature (°C)	450 ± 5

Reference: Adapted from Biava (2019)

3.4 Hot corrosion in molten aluminum methodology

Corrosion in molten aluminum was analyzed by mass measurement and visual analysis over immersion time in molten aluminum. Figure 22 shows the arrangement utilized and the dimensions of the samples.

Figure 22 – (a) Coated crucible used for corrosion tests and (b) standardized dimensions of the samples.

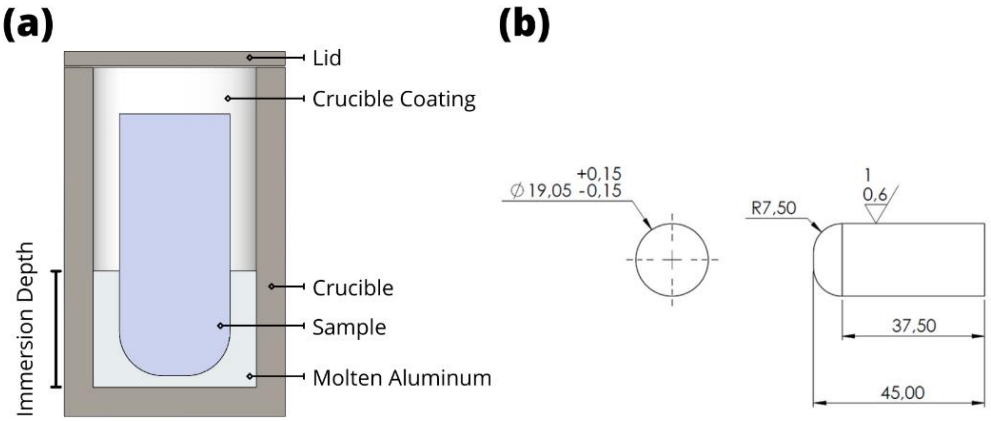

Reference: Author

The bullet profile of the sample was chosen to avoid any coating defects caused due to sharp edges. The immersion depth was 20 mm, and a lid was used to minimize oxygen interactions. For every interval, the mass was measured and the sample photographed. Before measuring the mass, the samples were ultrasonic cleaned in 99.8% ethyl alcohol. The total corrosion time was 40 hours, and the intervals chosen were 1-1-2-4-8-8-8-8 hours. After corrosion, cross-section images using SEM and chemical analyses using EDS were performed.

3.5 Die soldering testing methodology

The apparatus to make samples for soldering analyses are shown in figure 23.

Figure 23 - (a) Finned graphite crucible, (b) graphite crucible and (c) standardized dimensions of the samples.

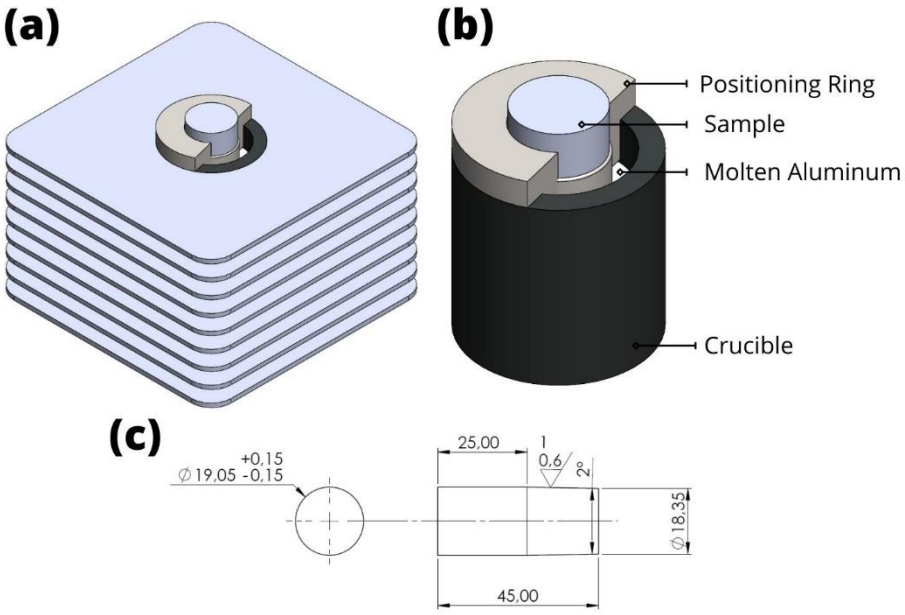

Reference: Author

Two different processes were used to make the samples. The first one, figure 23 (a), was made using a finned graphite crucible to perform a simple cast. The pins were positioned in the middle of the crucible using a positioning ring. Molten aluminum at 720 °C was poured into the crucible and heat removed by the fins. The second one, figure 23 (b), was a graphite crucible used to put the pin in molten aluminum and return the system to the furnace at 720 °C, keeping the molten metal in contact with the sample surface. Figure 23 (c) shows the dimension of the sample. The pin was manufactured with a cylindrical shape and had all the contact surface coated. In addition, a draft angle was used to assist with releasing. For both systems, the sample was cooled at room temperature. After cooling, the samples were machined to standardized dimensions, as shown in figure 24 (a). The aluminum ring was machined to 10 ± 0.1 millimeters in height and 28 ± 2 millimeters of external diameter.

Figure 24 - (a) Sample after turning process and (b) extraction system.

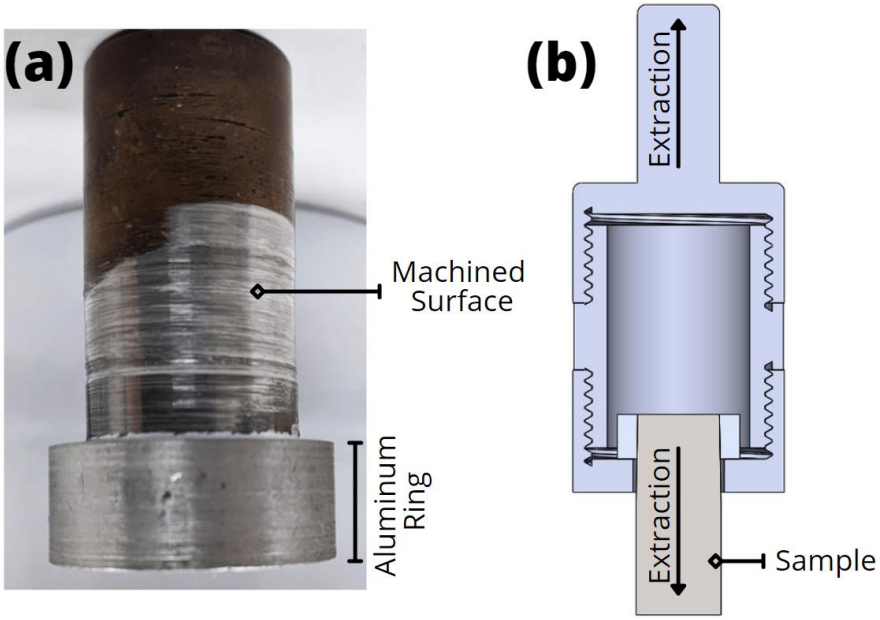

Reference: Author

After the machining process, the samples were attached to a tensile testing machine using the coupling system shown in figure 24 (b), and the extraction stresses were measured. To avoid any machinery influence, only facing operation was used during the turning process to standardize the height of the samples. After extraction, the aluminum ring and pin were analyzed.

3.6 Microstructural characterization

Optical microscopy (OM) was performed using Zeiss A2.m (Zeiss, Zeiss Microscopy, Oberkochen, Germany) with Axio Vision software for image analysis. For scanning electron microscopy (SEM), a Tescan VEGA3 (Tescan, Brno, Czech Republic) was used with an x-act silicon drift detector (Oxford Instruments, Abingdon-on-Thames, United Kingdom) for energy dispersive spectroscopy (EDS). Seven OM images were used to evaluate porosity according to ASTM E 2109-01. Prior to any analysis, the samples were grinded with sandpaper and polished with 0.25 μm diamond suspension. Polishing was done using an automated polisher, using 25 newtons of applied force. Chemical etching for metallic samples was performed using nital 5% concentration for 20 seconds. Vickers hardness was measured with a Shimadzu HMV-G20 (Shimadzu Corporation, Kyoto, Japan) in accordance with ASTM E 384-99 and 500 gf load. For XRD analyses, a Bruker ECO D8 Advance X-ray diffractometer (Bruker AXS Inc., Madison, WI, USA) and a Diffract.EVA v4.2.2 were used. The

wavelength was 1.54 Å (Cu-Kα) for HVOF and PVD coatings. Other parameters are shown in table 5. Nanoindentation was performed using Asmec UNAT (Dresden, Germany) equipment with a Berkovich-type pyramidal diamond tip. The method used was quasi-continuous stiffness measurement (QCSM) with a maximum load of 400 mN.

Table 5: Parameter used in the XRD analyses for HVOF and PVD coatings.

Parameter	HVOF coating	PVD coating
Voltage (kV)	30	40
Current (mA)	30	25
Incidence angle (°)	30	5
Sampling pitch (°)	0.02	0.025
Time per pitch (s)	4	0.2

Reference: Author

4 RESULTS AND DISCUSSION

4.1 HVOF and PVD coatings

The microstructure of the AISI H13 used for the analyses is shown in figure 25. After heat treatment, the H13 tool steel disclosed a hardness of 477.9 ± 12.6 HV_{500g}. It is possible to observe that the microstructure achieved a predominant martensite composition. According to the heat treatment quality microstructure chart found in NADCA Die Materials Committee (2006), this microstructure is similar to HS4 and HS7 microstructures.

Figure 25: (a) 500x and (b) 1000x optical microscopy images of the microstructure of the AISI H13 used as substrate for the analyses after heat treatment.

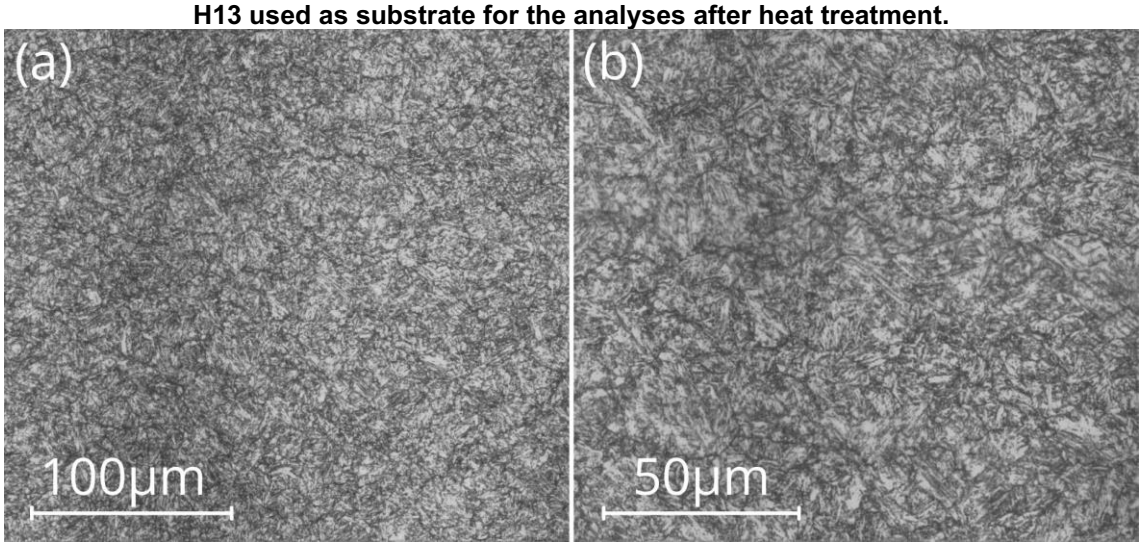

Reference: Author

Figure 26 shows the coatings deposited by HVOF. It is possible to observe morphological differences between them. Figure 26 (b) shows the chromium carbide coating. It is possible to discern carbides, metallic matrix, and porosity. Meanwhile, the AISI H13, figure 26 (c), shows a lamellar distribution of metallic phase with oxides and a small amount of porosity. It is also possible to observe the martensite presence in the substrate, figure 26 (a and c). Several measured characteristics of the HVOF coatings are shown in table 6.

Figure 26 – Cross-section optical microscopy images of (a) Cr_3C_2 25NiCr and (c) AISI H13 HVOF coatings after chemical etching and SEM images of (b) Cr_3C_2 25NiCr and (d) AISI H13 HVOF coatings before chemical etching deposited on AISI H13.

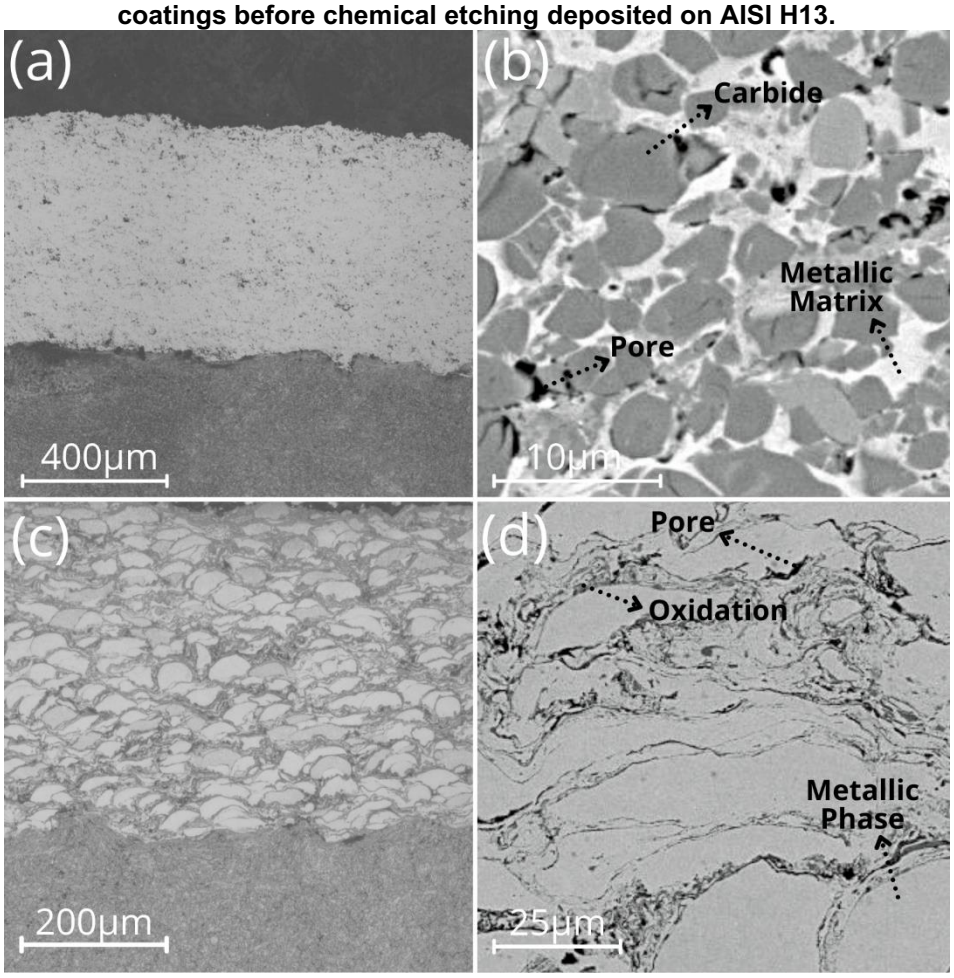

Reference: Author

Table 6 - Composition of the thermally sprayed coatings.

Property	Cr_3C_2 25NiCr	AISI H13
Porosity (%)	3.6±1.4	1.11±0.22
Oxides (%)	*	3.35±1
Hardness (HV_{500g})	707.2 ± 89.9	560.0±22.5
Coating Thickness (µm)	545.1±41.5	412.1±27.5

Reference: Author

Figure 27 shows the SEM images of the AlCrN PVD coating. In figure 27 (a), it is possible to observe some defects on the surface, such as microdroplets/macrodroplets and pores. These defects are well known, as shown in some studies (ADESINA *et al.*, 2019; BARONINS *et al*, 2018; MISHRA *et al.*, 2021). According to Adesina *et al.* (2019), the surface defects are the main setbacks of PVD coatings. These defects affect the corrosion properties causing sticking to the workpiece, localized coating failure, and pitting corrosion. Figure 27 (b) shows the cross-section image of the AlCrN PVD coating. After the deposition, the AlCrN PVD coating resulted in a thickness of 2.05 ± 0.057 µm. Graph 1 shows the hardness of the AlCrN PVD and the H13 tool

steel after heat treatment. The hardness exhibits a plateau up to approximately 200 nm. It corresponds, as expected, to about 10% of the measured thickness of the AlCrN PVD coating. In this range of contact depth, the plastic deformation does not reach the substrate, as shown by Saha and Nix (2002). Therefore, this value corresponds to the hardness of the film, which the average is 29 ± 6 GPa.

Figure 27: (a) Surface and (b) Cross-section SEM images of the AlCrN PVD coating.

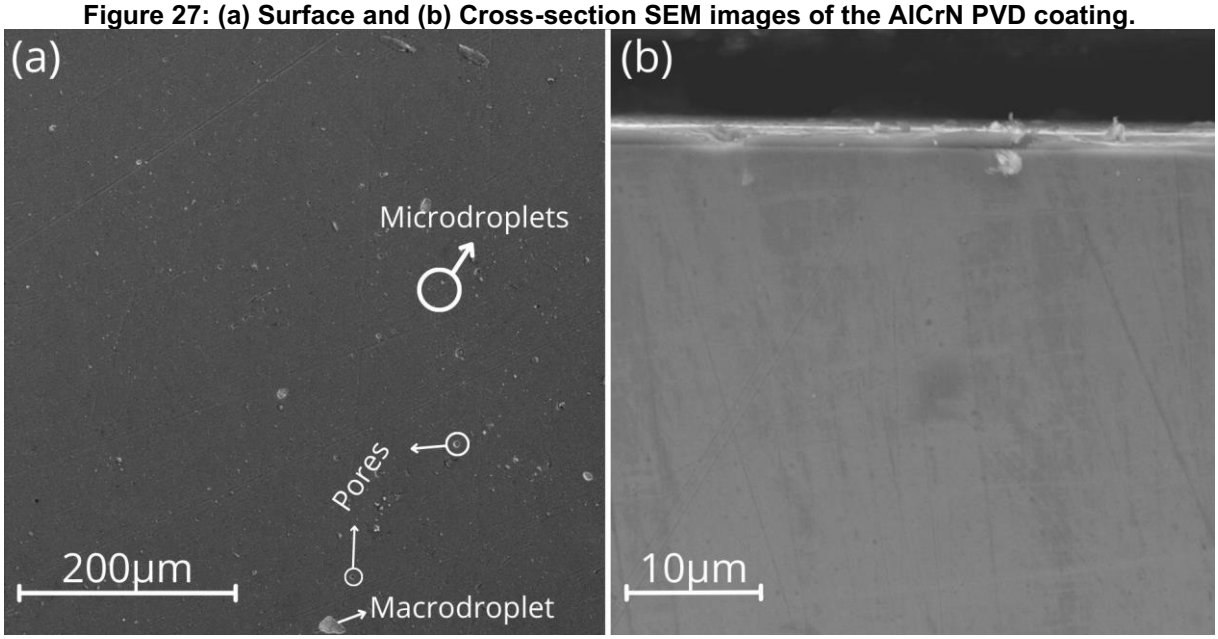

Reference: Author

Graph 1: Hardness of the AlCrN PVD coating and AISI H13 substrate after heat treatment.

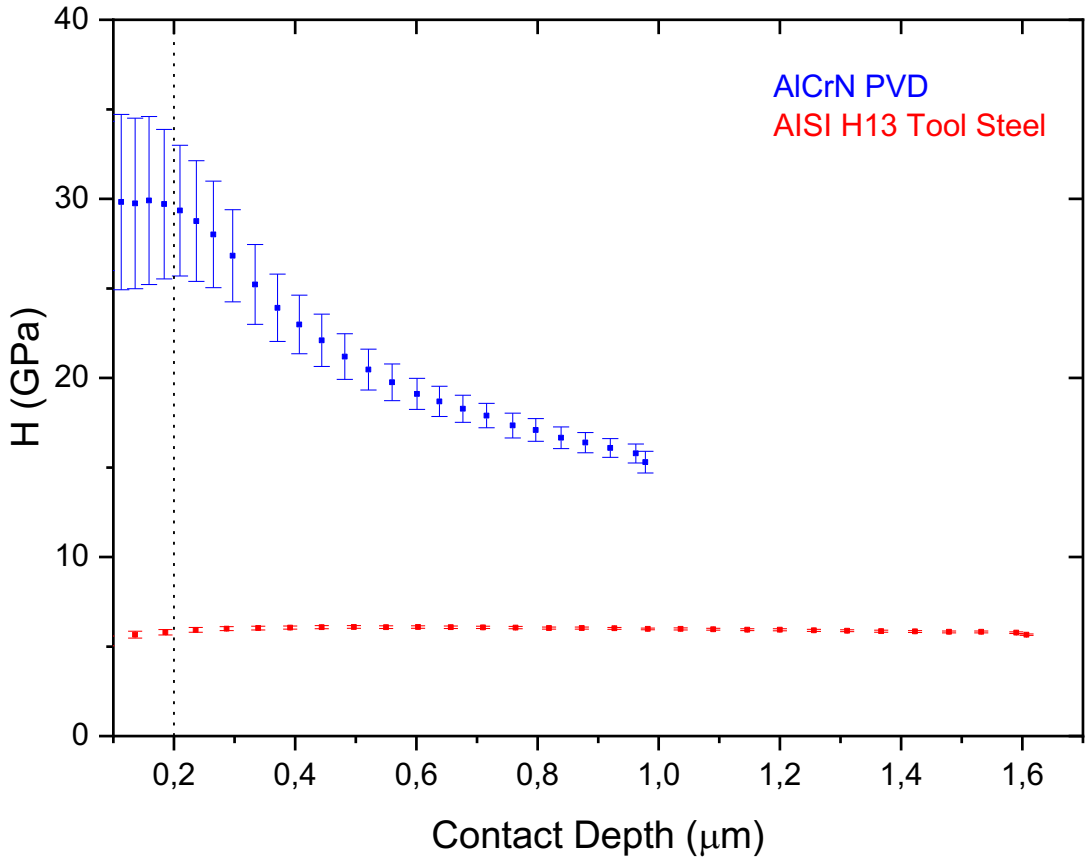

Reference: Author

Graph 2 shows the XRD diffractogram for HVOF coatings. The H13 HVOF coating showed peaks of martensite (α') and some retained austenite (γ). The main martensite structure is because of the high cooling rates. The Cr_3C_2 25NiCr showed the main peaks of nickel at 43° and 44°. It also disclosed many Cr_3C_2 peaks, showing the strong retention of the carbide. Other Cr_xC_y were not found in this analysis. Graph 3 shows the XRD diffractogram for AlCrN PVD coating. Peaks for c-CrN and c-AlN are represented in the diffractogram. The peaks are found in the between due to the good solubility of c-CrN into c-AlN, according to Biava *et al.* (2022).

Graph 2: XRD diffractograms of the HVOF coatings.

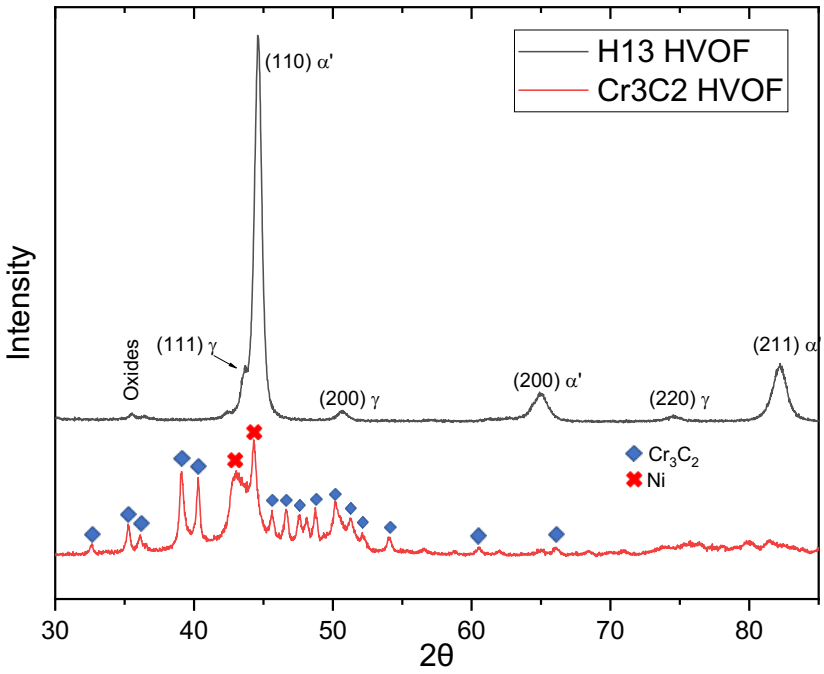

Reference: Author

Graph 3: XRD diffractogram of the AlCrN PVD coating.

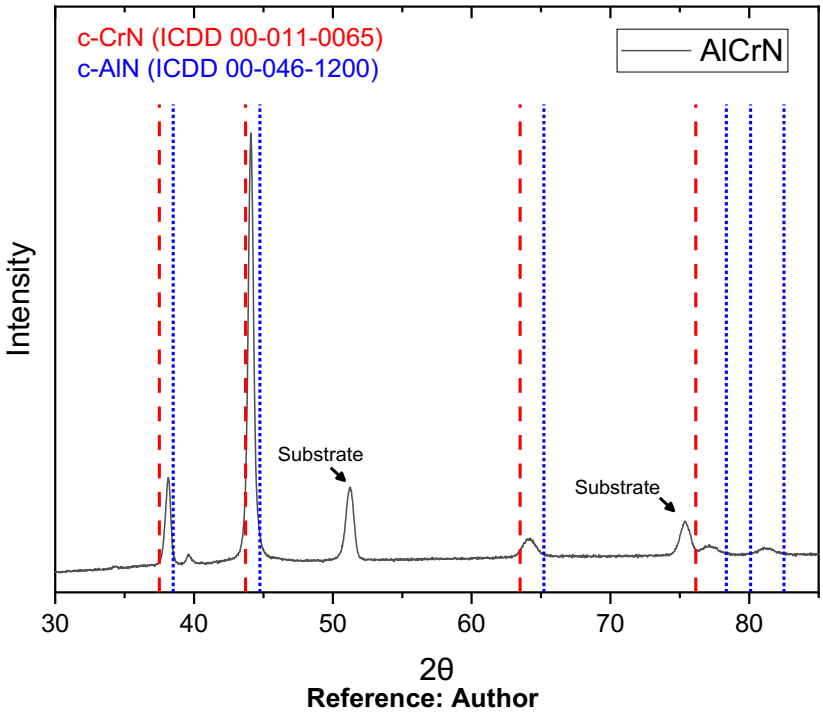

Reference: Author

Energy dispersive spectroscopy was also applied to analyze the chemical composition of the coatings after deposition, as shown in table 7. Oxygen is found in AISI H13 composition due to the spraying process, as the particles react during its

projection and the atmosphere exposition between the deposition layers (LIMA; TREVISAN, 2007).

Table 7 - EDS measurement of the chemical composition after coating processes.

Cr_3C_2 25NiCr HVOF(Wt%)	Chromium	Nickel	Carbon			
	65.0	21.9	13.2			
AISI H13 HVOF (Wt%)	**Iron**	**Chromium**	**Oxygen**	**Silicon**	**Vanadium**	**Molybdenum**
	88.5	5.1	3.7	1.2	0.91	0.6
AlCrN PVD (Wt%)	**Chromium**	**Aluminum**	**Nitrogen**			
	35.0	31.8	29.6			

Reference: Author

4.2 Molten aluminum corrosion

Graph 4 shows the mass change for all analyzed samples. Some mechanisms change the mass of the samples; the first one is the aluminum adhesion. At the beginning of the curve, it is possible to observe the mass gain due mechanical and chemical adhesion of the aluminum alloy. Chemical bonding occurs between the sample surface and the molten aluminum. Depending on the bonding forces of the corrosion products, the material starts to gain more or less mass. During the test, the chemical reaction between the molten aluminum alloy and the sample surface reduces the adhesion strength, and the aluminum intermetallic detaches from the surface. A new surface is created, promoting new reactions, and the corrosion of the material continues until the mass change reaches negative values.

From figure 28 to figure 31, the specimens are shown; in the top left-hand corner of each figure, the accumulated corrosion time in hours can be observed. Figure 28 shows the corrosion behavior of AISI H13, which is being used as a standard. In the photograph after 24 hours of corrosion, it is possible to observe a change in the diameter of the sample at its tip. A blue oxide has been shown after 32 hours, and the same oxide has appeared for AISI H13 HVOF and H13 with PVD. In the case of the Cr_3C_2 25NiCr, the bonding forces were great that at 40 hours of corrosion it had not reached negative mass change, graph 4. Nonetheless, it does not mean superior corrosion resistance to molten aluminum. As shown in figure 31, the adhesion of aluminum and corrosion products create an increase in diameter. As HVOF AISI H13 is concerned, the photographs have shown similar results compared to AISI H13. The results were also similar for mass change from 0 to 8 hours, with a deviation for higher corrosion time.

Graph 4 - Mass change over time for corrosion in molten aluminum (A383) at 720 °C.

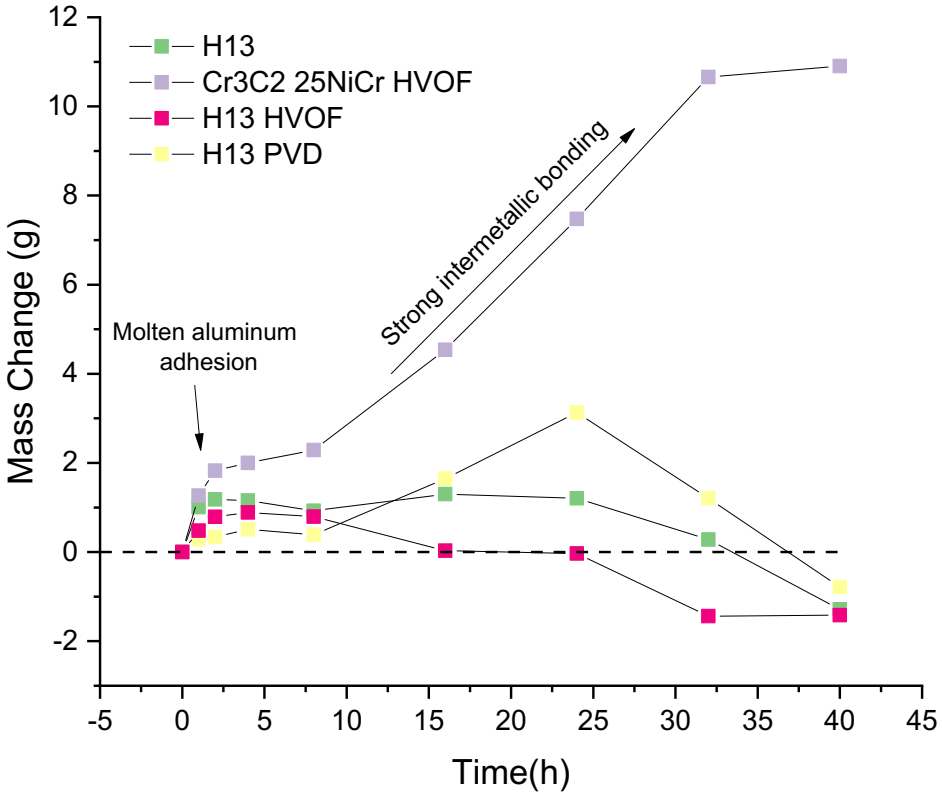

Reference: Author

Figure 28 - Photographs of AISI H13 after corrosion in molten aluminum (A383) at 720 °C and EDS of blue oxidation after 40 hours of immersion.

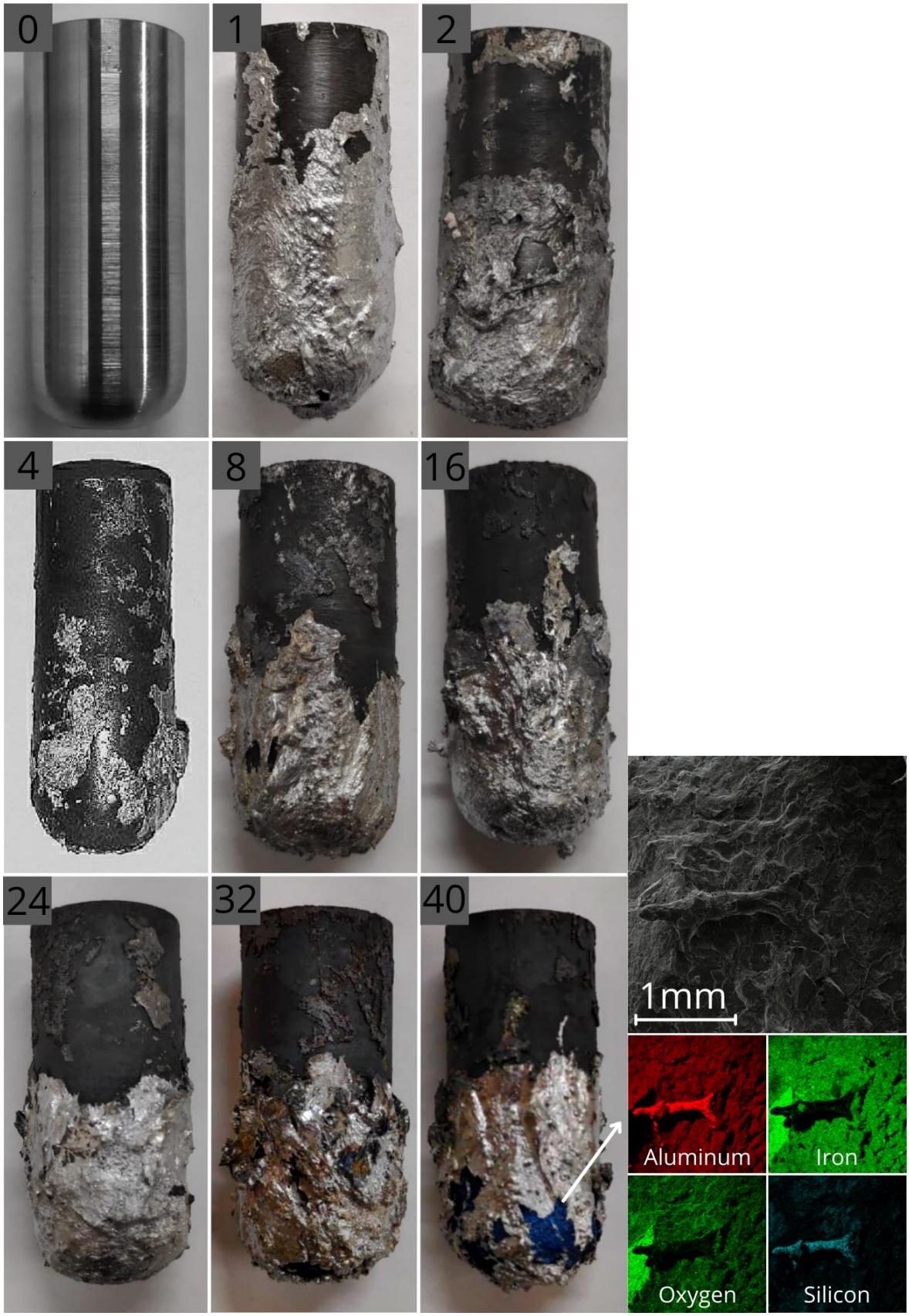

Reference: Author

Figure 29 - Photographs of AISI H13 coated with AlCrN by PVD process after corrosion in molten aluminum (A383) at 720 °C.

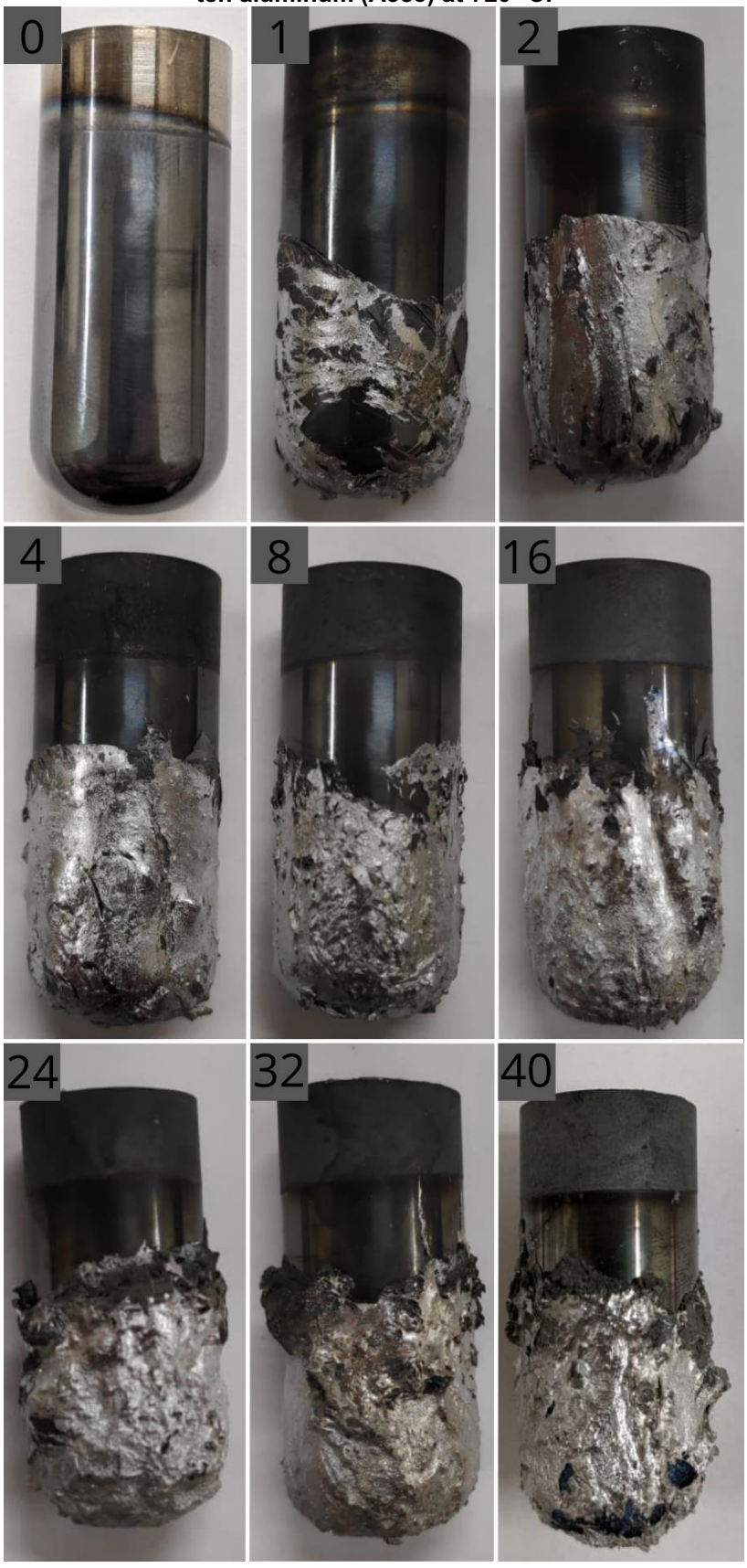

Reference: Author

Figure 30 - Photographs of AISI H13 coated with AISI H13 by HVOF process after corrosion in molten aluminum (A383) at 720 °C.

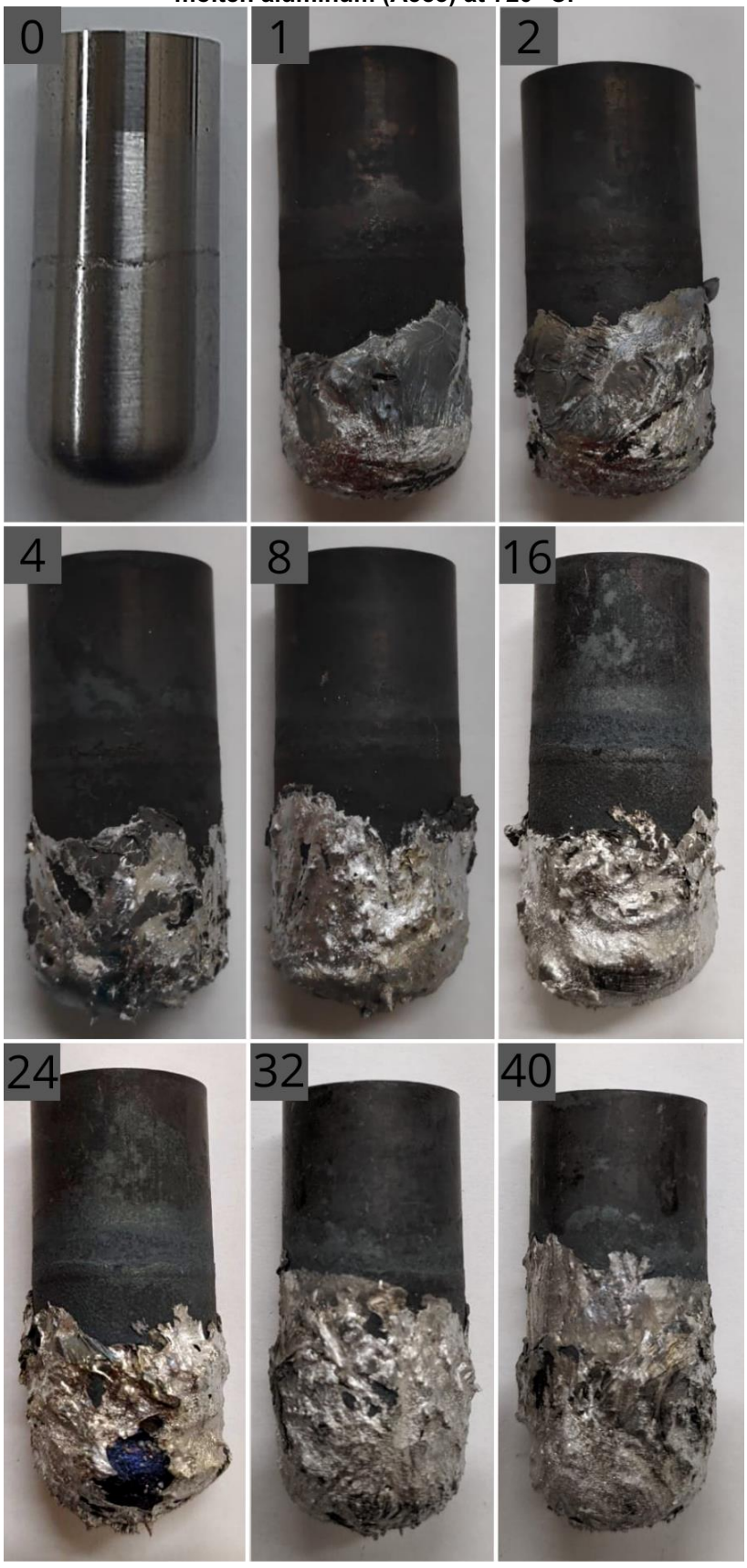

Reference: Author

Figure 31 - Photographs of AISI H13 coated with Cr_3C_2 25NiCr by HVOF process after corrosion in molten aluminum (A383) at 720 °C.

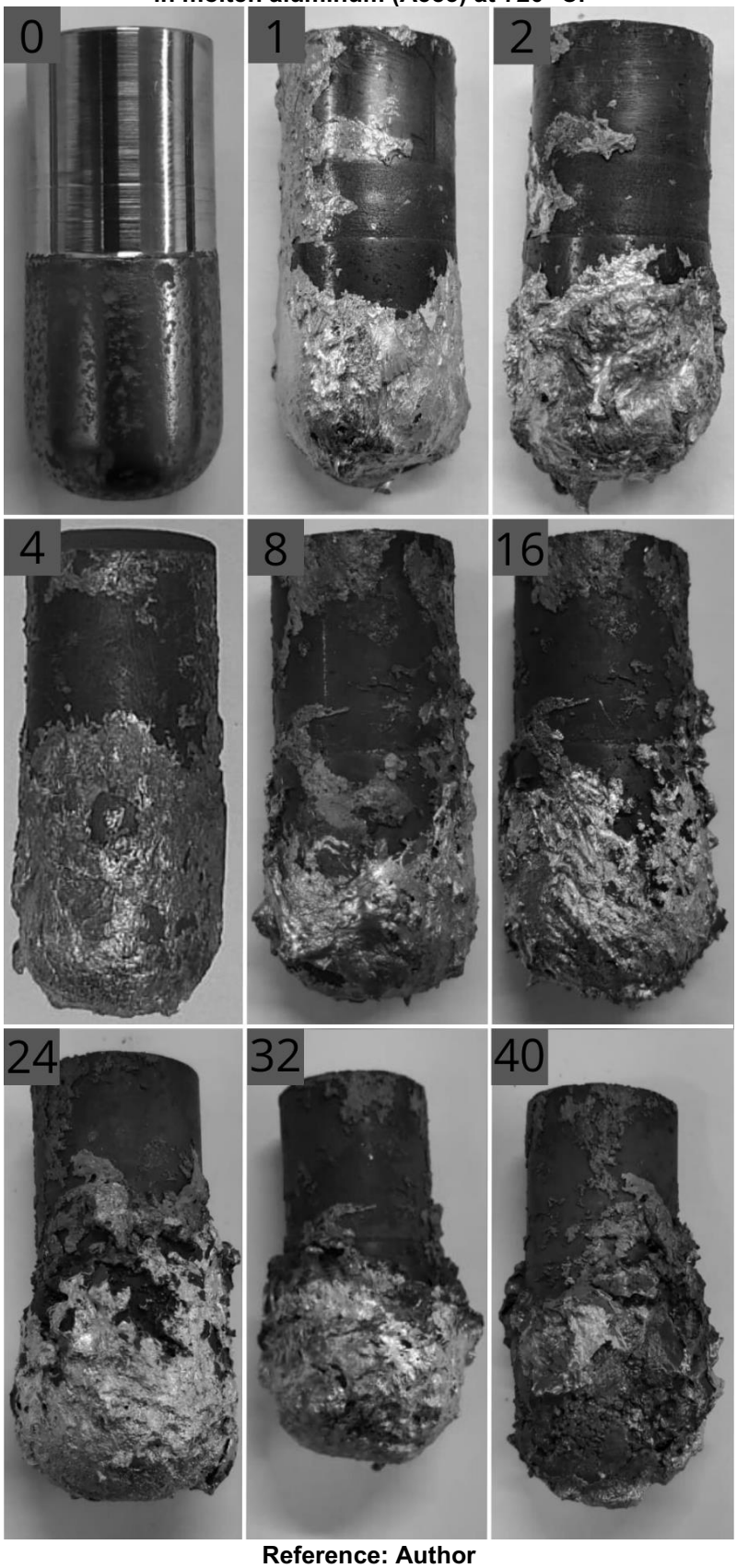

Reference: Author

A second run of samples was performed until 8 hours to evaluate the cross-section, shown in figure 32. All coated specimens had the substrate totally exposed after 40 hours of corrosion. AlCrN PVD has shown great protection for up to 8 hours. Nonetheless, pitting incubation has been observed. Furthermore, similar behavior is shown in the cross-sectioned sample after 40 hours, comparing it to AISI H13. The AISI H13 deposited with HVOF has shown some coating remnants after 8 and 40 hours of corrosion. These remnants were found surrounded by iron oxides formed during the corrosion test, shown in figure 33. The coating that was not protected by oxides was consumed after 8 hours. EDS analysis has shown an average composition of 40.7At% Fe and 59.3At% O of the oxide after 40 hours in molten aluminum, indicating a composition of Fe_2O_3. Concerning Cr_3C_2 25NiCr, a thin layer of the coating resisted after 8 hours, and it is possible to observe the beginning of the strongly adhered layer (g). After 40 hours (h), the coating was completely consumed.

Figure 32 - Cross section image for AISI H13 after 8 (a) and 40 (b) hours, (b) PVD AlCrN after 8 (c) and 40 (d) hours, AISI H13 by HVOF after 8 (e) and 40 (f) hours and Cr3C2 25NiCr by HVOF after 8 (g) and 40 (h) hours.

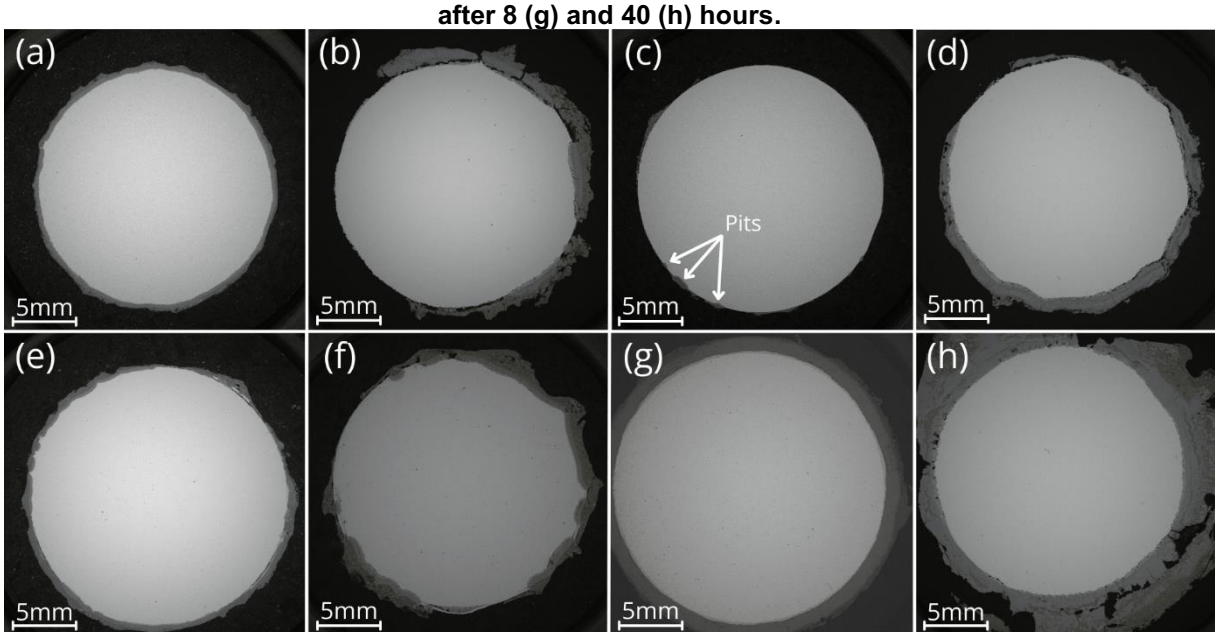

Reference: Author

Figure 33 - Remaining AISI H13 coating after 40 hours of corrosion in molten aluminum (A383) at 720 °C.

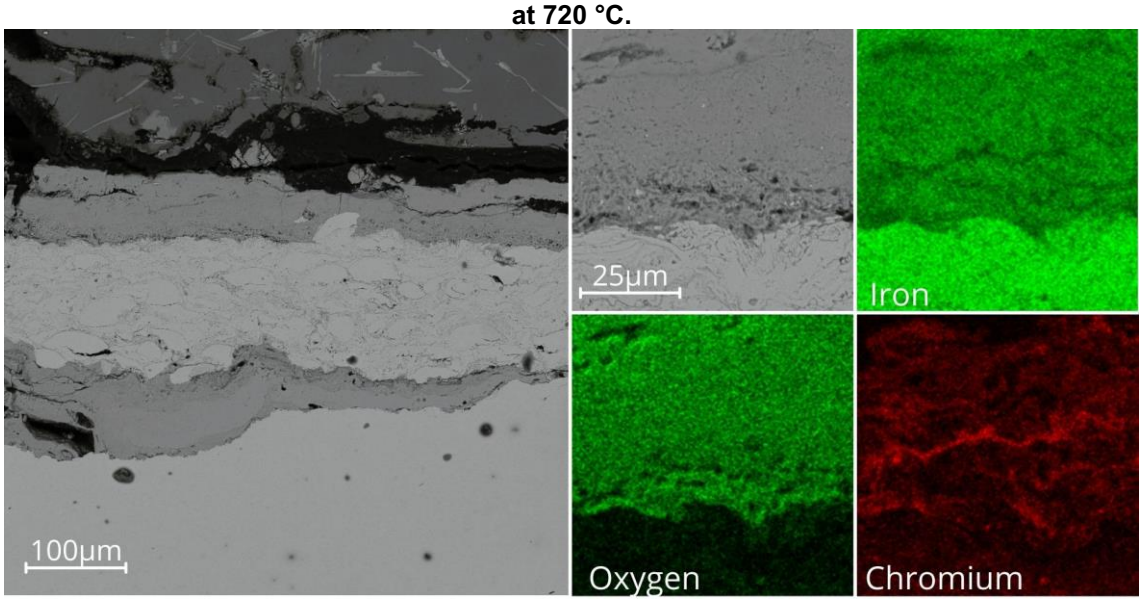

Reference: Author

4.3 Molten aluminum soldering

The results of die soldering tests are shown in graph 5, and the samples images after extraction are shown in figure 34. The extraction resistance of the simple cast samples (a) is similar for every sample, except for the H13 coated with AlCrN PVD. After 10 minutes at 720 °C (b), the extraction resistance changed significantly, and H13 HVOF had the highest extraction resistance. However, extraction resistances for H13 HVOF after 10 and 30 minutes are not valid, as the coating could not bear the forces and detached from the substrate, as shown in figure 34 (c). Also, the presence of oxidation underneath the coating was visible in the sample after 30 minutes of exposition to molten aluminum. This underneath corrosion is believed to be the main reason for the drop from 34.86 MPa to 29.85 MPa in extraction resistance. The Cr_3C_2 25NiCr coating has shown the second lower extraction stress for 10 minutes. However, after 30 minutes, bonding forces widely changed the results. For all tests, PVD coating showed the best results. Figure 35 shows SEM images of the surface after extraction of the aluminum ring; it is clear the difference on PVD surface after aluminum corrosion in figure 35 (b). In a similar way, the PVD surface has changed in the figure 34 (b). Regarding H13, the results for 10 and 30 minutes are close, with 10 minutes being strongly adhered to the surface. This result will be further discussed based on SEM and EDS analyses. Also, these graphs showed the importance of evaluating soldering over time, as the extraction resistance has significantly changed over time.

Graph 5 - Soldering extraction resistances. (a) Simple cast, (b) after 10 minutes in molten aluminum and (c) after 30 minutes in molten aluminum.

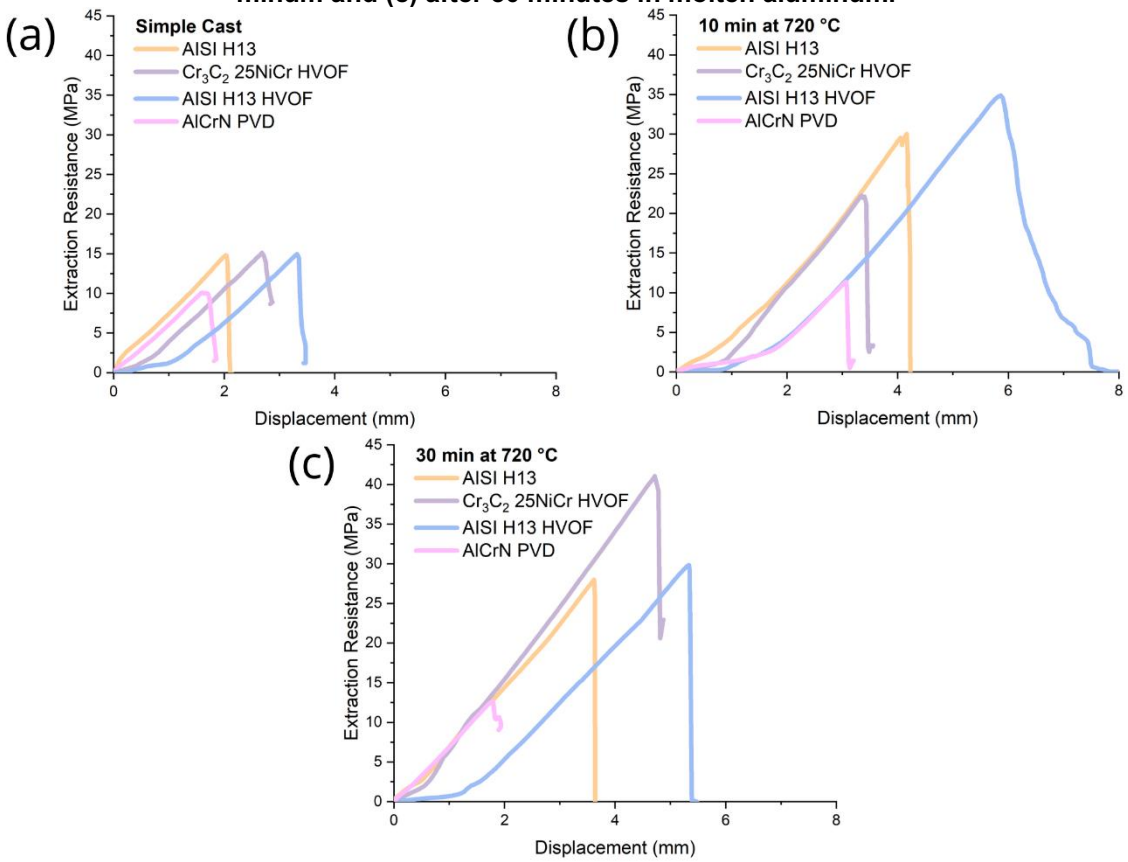

Reference: Author

Figure 34 - Samples after aluminum ring extraction. From left to right: simple cast, 10 minutes and 30 minutes aluminum contact. (a) AISI H13, (b) AISI H13 coated with AlCrN PVD, (c) AISI H13 coated with H13 by HVOF and (d) AISI H13 coated with Cr_3C_2 25NiCr by HVOF.

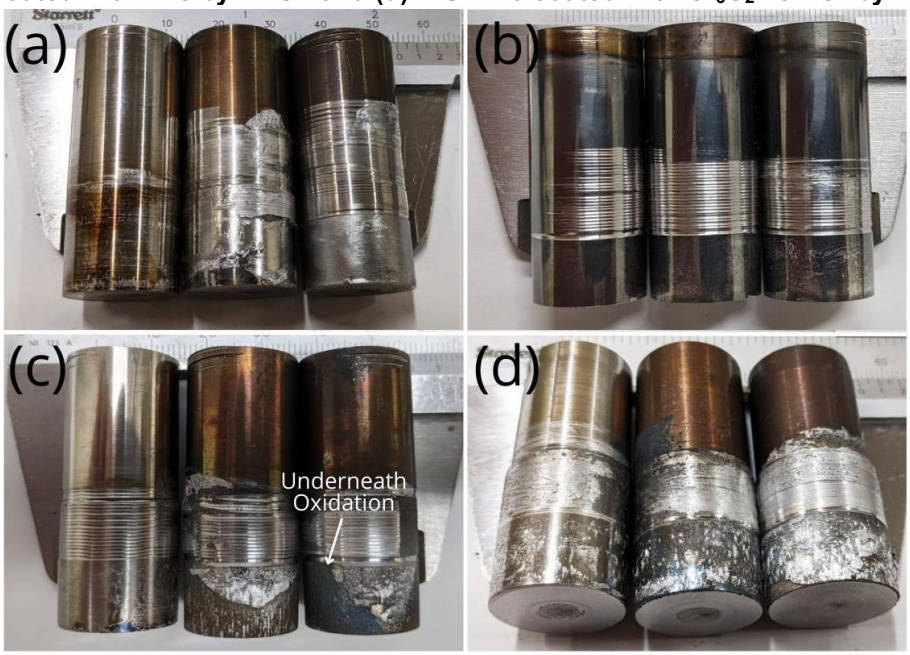

Reference: Author

For simple cast AISI H13 (a-0), it is possible to observe the grooves from griding the sample to reach the desired roughness, along with aluminum adhesion. After 10 minutes at 720 °C (a-1), the surface shows a drastic change in surface roughness. Notwithstanding, the intermetallic detached after aluminum ring extraction. After 30 minutes at 720 °C (a-2), the surface is completely covered by intermetallic formed by the corrosion process between the substrate and aluminum alloy. For both HVOF coatings, surfaces have shown corrosion products after 10 minutes. In spite of being the most resistant surface for soldering, it is possible to notice in the AlCrN PVD images a change throughout the time. The EDS analyses from the images in figure 35 are shown in appendix A.

Figure 35 - SEM images of the surface after aluminum ring extraction. (x-0) Simple cast, (x-1) 10 minutes and (x-2) 30 minutes. (a) AISI H13, (b) AlCrN PVD, (c) AISI H13 HVOF and (d) Cr_3C_2 25NiCr HVOF.

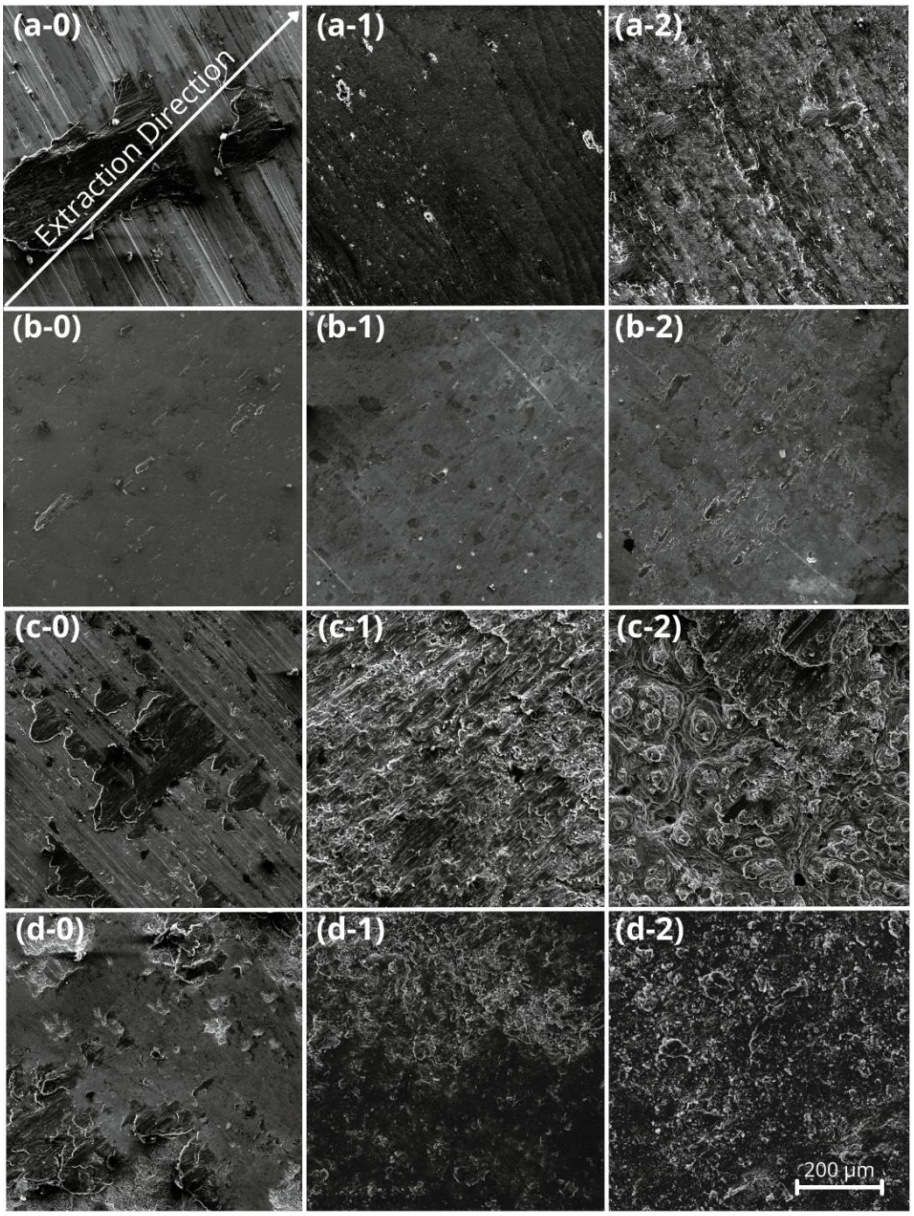

Reference: Author

Table 8 summarizes all the information regarding soldering for the surfaces. The diffusional layer thickness was calculated using the extracted rings and pins, shown in

figure 61 in appendix A. Due to the adhesion forces of the chromium carbide coating, the diffusional layer was measured using the pins, since the intermetallics were totally detached from the aluminum ring. For the AlCrN PVD, no diffusion was observed.

Table 8 - Results summary for soldering.

	Detachment Stress (MPa)			Diffusional Layer Thickness (µm)	
Surface	Simple cast	10 min	30 min	10 min	30 min
H13	14.81	30.03	27.99	51.9 ± 3.1	145.7 ± 6.4
AlCrN PVD	10.08	11.40	12.61	Null	Null
H13 HVOF	14.98	34.86	29.85	12.5 ± 5.1	23.2 ± 3.8
Cr_3C_2 25NiCr HVOF	15.12	22.24	41.05	8.2 ± 2.3	55.1 ± 9.2

Reference: Author

4.4 High temperature aluminum corrosion mechanisms

In this section, the mechanisms of corrosion by A383 aluminum alloy will be discussed. As soldering and corrosion are intrinsically the same phenomenon, both corrosion and soldering specimens will be used to explore the corrosion mechanisms. As the main focus is to identify the mechanisms for each surface, the chapters are divided based on the materials and coatings used. Furthermore, no chemical reactions were found for simple cast samples, as shown in figure 58 and figure 59 in appendix A.

4.4.1 AISI H13

Figure 36 shows the surface after aluminum ring extraction of the AISI H13 samples for both 10 and 30 minutes in molten aluminum. It is possible to observe the nucleation of generalized corrosion. Even being generalized, there is a curling pattern creating the bonding connection between the H13 tool steel and intermetallic. Similar morphology was found by Chen *et al.* (2019). Also, EDS point analyses were made on the surface to measure the chemical composition of the intermetallic layer in contact with the H13 surface, the chemical composition of the H13 samples is shown in table 9.

Figure 36 - SEM and EDS images of AISI H13 (a and b) After 10 minutes and (c and d) after 30 minutes.

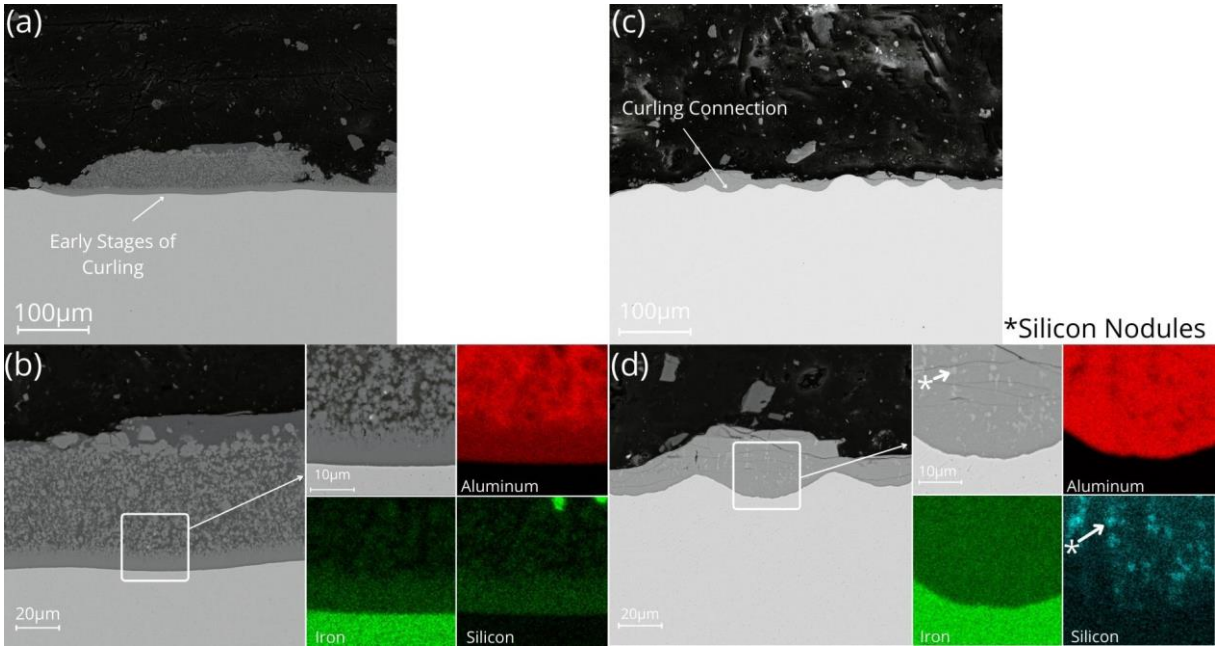

Reference: Author

Table 9 - Chemical composition of the intermetallic layer after the surface in function of time in molten aluminum.

Time (min)	Fe (At%)	Al (At%)	Si (At%)
10	18.0 ± 1.0	67.2 ± 1.0	13.7 ± 0.2
30	26.3 ± 0.4	67.9 ± 2.1	5.8 ± 2.4

Reference: Author

It is possible to observe an increase in iron and a decrease in silicon contents. The chemical composition calculated and EDS images suggest the formation of a $FeAl_3$ phase after 10 minutes of testing at 720 °C, as also found by Han and Viswanathan (2003). After 30 minutes, a phase of Fe_2Al_5 stabilized with the presence of silicon nodules. Even after the surface contact increase between AISI H13 and the intermetallic phase after 30 minutes, the extraction stresses for the H13 in graph 5 were similar due to the more brittle nature of the Fe_2Al_5 phase, as evaluated by Matysik *et al.* (2015). It is also possible to find cracks in the intermetallic formed after 30 minutes. Furthermore, the diffusional layer thickness grows from 51.9 ± 3.1 µm after 10 minutes to 145.7 ± 6.4 µm after 30 minutes. This linear growth behavior means that the diffusion, for this interval of time, can be modeled using Fick's first law. Nonetheless, the growth of the new phase of Fe_2Al_5 will probably change the diffusion rate for longer periods.

Therefore, the main mechanism of soldering is simple dissolution corrosion, driven by diffusion, with well-distributed dissolution in a curling pattern. As time is given, new phases are stabilized because of the saturation of the aluminum alloy with iron.

The curling pattern of corrosion grows, but soldering extraction stresses do not significantly change from 10 to 30 minutes due to the mechanical properties of the intermetallic grown.

4.4.2 Corrosion mechanisms of the AlCrN PVD coating

AlCrN PVD coating has successfully been able to diminish the aluminum reaction along the 8 hours of molten aluminum exposition, figure 32. Also, soldering extraction resistances were the smallest. The coating thickness has also not changed until 8 hours. Nonetheless, EDS analysis on the surface after aluminum ring extraction has shown a chemical composition change after only 30 minutes. Graph 6 shows the surface composition over time for aluminum corrosion. The molten aluminum has a clear effect on the nitrogen concentration of the coating on the surface of the sample. As shown by Wu *et al.* (2015), AlCrN coatings have a typical alternated structure of AlN and CrN. Therefore, by diffusing the nitrogen, the phases of the coating are degraded, and the remaining surface is more prone to corrosion. Furthermore, figure 37 and figure 38 show some defects found in the cross-section of the sample after 30 minutes and 8 hours, respectively. From 30 minutes to 8 hours, the occurrence and size of defects increased. Some of these defects were described by Song *et al.* (2012), where they described the steps for the CrN PVD coating failure and soldering. It is also possible to observe the presence of initial pits, figure 32 (c). The pits are described by Song *et al.* (2012) in figure 6 and are the leading defect to reach the curly surface shown in figure 32 (d).

Graph 6 - Chemical composition of AlCrN PVD coating over corrosion time.

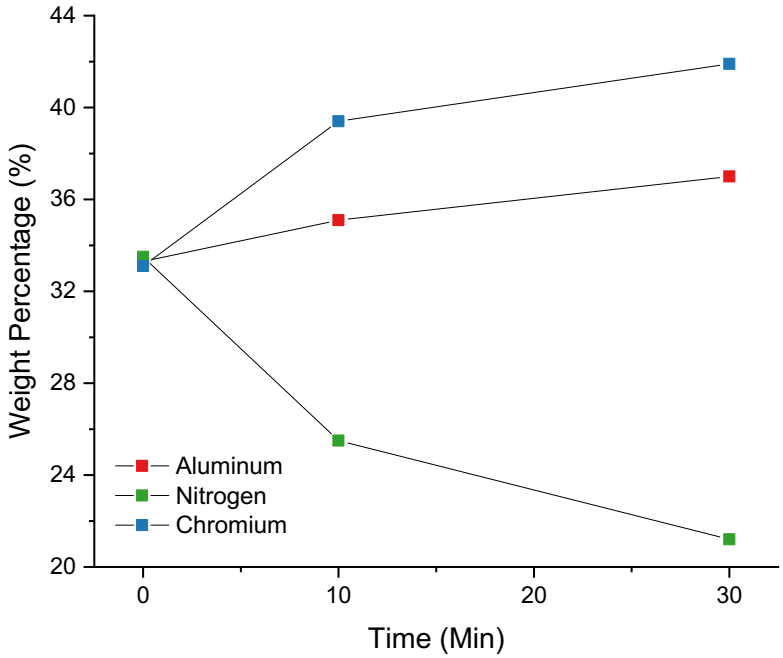

Reference: Author

Figure 37 - (a-d) Surface defects of AlCrN PVD after molten aluminum corrosion for 30 minutes.

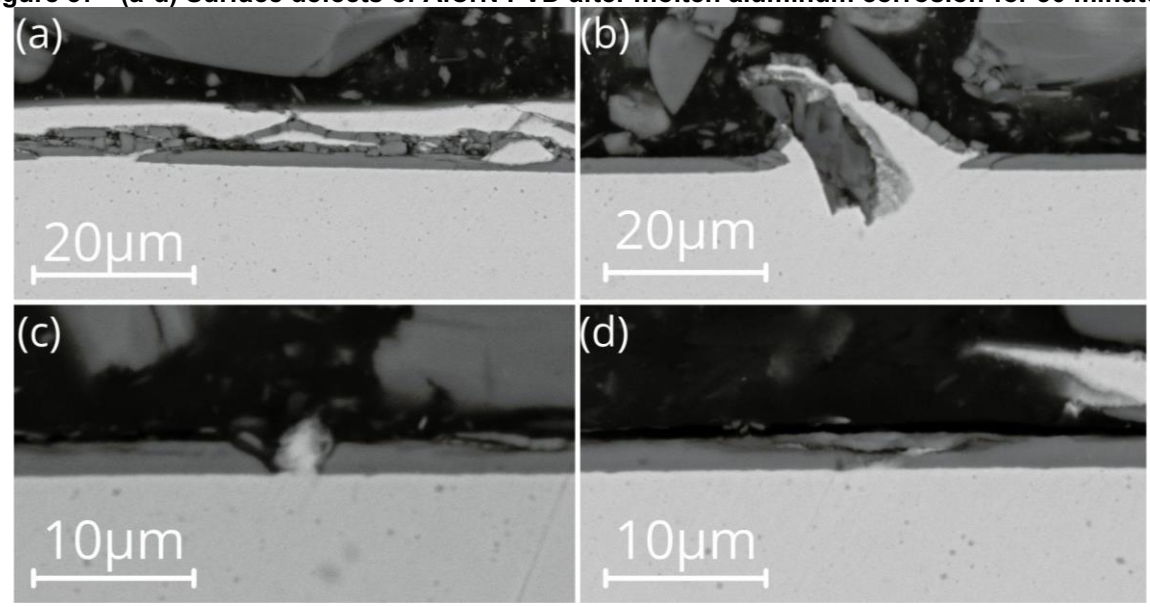

Reference: Author

Figure 38 - (a-c) Surface defects of AlCrN PVD after molten aluminum corrosion for 8 hours. Arrows are pointing to coating defects.

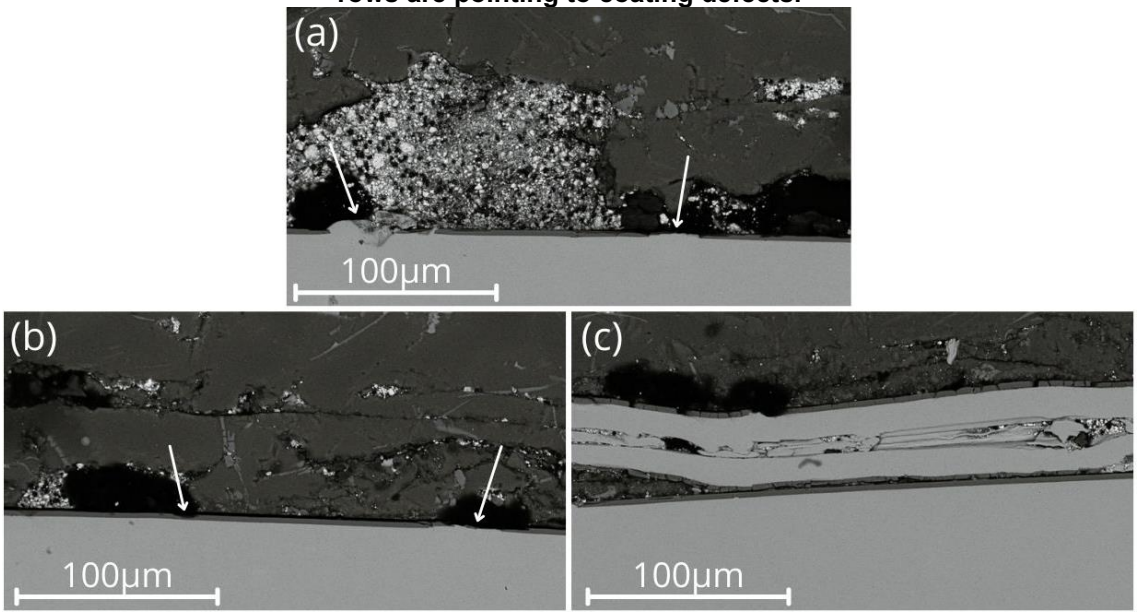

Reference: Author

It was also possible to observe a small degree of wettability for AlCrN coating, due to the presence of voids after the solidification of the aluminum. The presence of non-wet spots after the solidification of the aluminum was found by Gobber *et al.* (2019) for the surface that disclosed better adhesion of lubricant. Figure 39 shows two examples found in the samples analyzed after 8 hours in molten metal. In the first example, figure 39 (a), it is shown a void space between the AlCrN PVD coating and the solidified aluminum. The second example, figure 39 (b), shows a spot where the aluminum is touching the coating. It is also possible to observe nonwetted spots in figure 38 (b).

Figure 39 - AlCrN PVD coating after 8 hours of immersion in molten aluminum at 720 °C. (a) Example of a poor wettability region and (b) a region where the aluminum wets the coating.

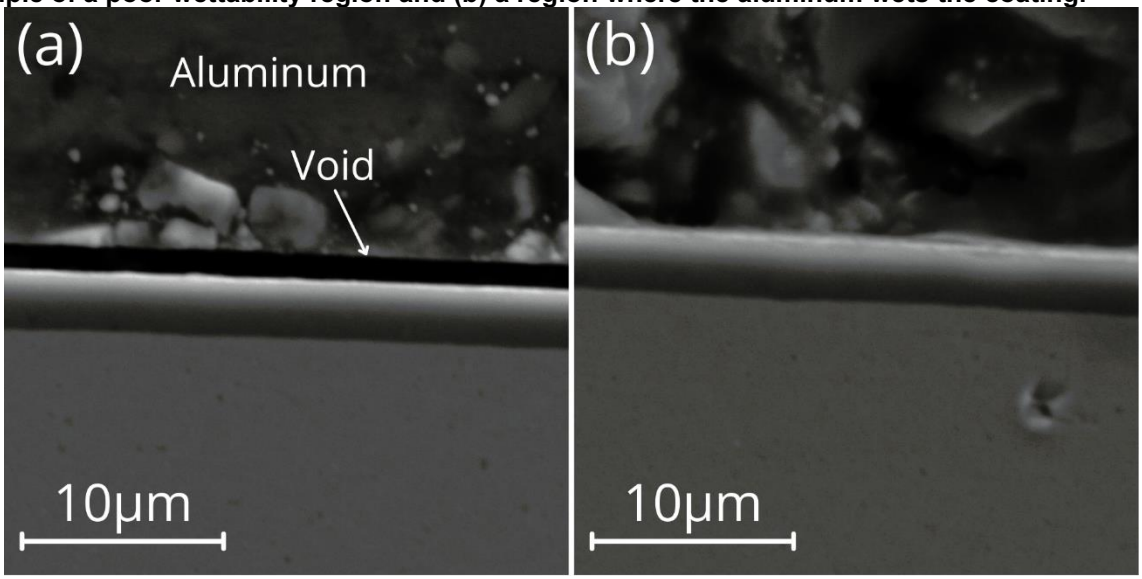

Reference: Author

The aluminum corrosion decreased the nitrogen content on the coating surface. As nitrogen atom has a relatively small diameter, its diffusion to the molten aluminum is the most probable mechanism. Also, the cross-section images have shown some defects in the coating. These defects are pre-existing defects that increase in size after molten aluminum corrosion. It is also possible to observe in figure 34 (b) the increase in adhered aluminum. Soldering has increased due to the defects created on the surface, allowing the molten aluminum to have contact with the substrate.

4.4.3 Corrosion mechanisms of the AISH H13 HVOF coating

Figure 40 shows the H13 HVOF surfaces after aluminum ring extraction for 10 and 30 minutes. EDS images of both regions are shown in appendix A. It is possible to observe the formation of circular regions rich in iron and silicon. This is caused by the iron-rich phases in the rupture region. Furthermore, the intermetallic formation exhibits a high adhesion and spiky form.

Figure 40 - SEM images (Backscattered-Electron) of AISI H13 HVOF from top surface (a) 10 minutes and (b) 30 minutes of corrosion in molten aluminum and cross-section (c) 10 minutes and (d) 30 minutes of corrosion in molten metal.

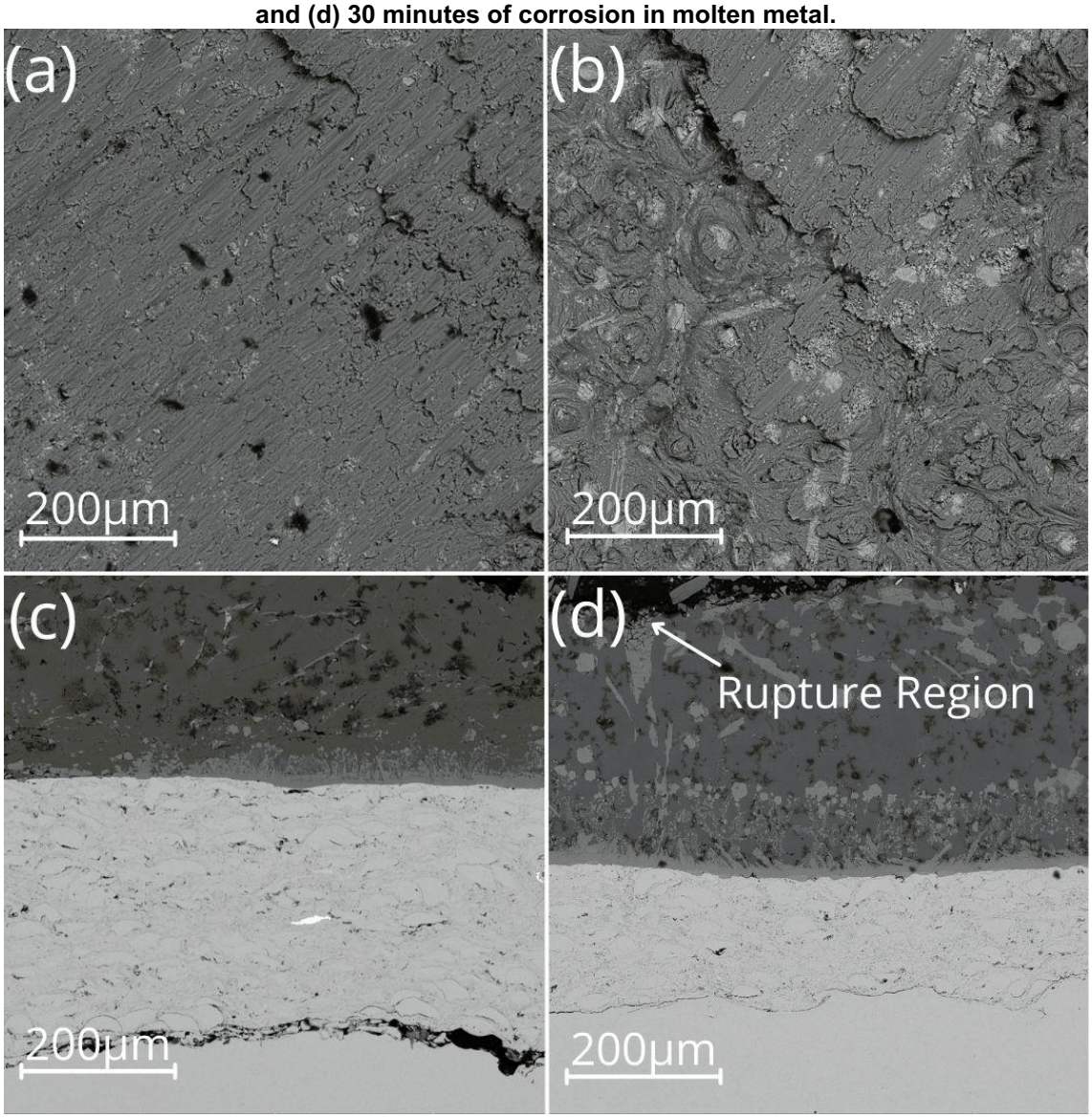

Reference: Author

EDS analysis shown in figure 41 indicates the composition map of the first diffusion layer between H13 HVOF coating and cast aluminum. It can be observed a higher concentration of iron in the inner layer. It is also possible to observe preferential corrosion behavior on the surface. The particle oxidation during the HVOF deposition process formed a protective intersplat oxide layer. These layers, along with the metallic phase, are shown in figure 42. This phenomenon has been explained by Chen *et al.* (2019, 2020), where iron oxides (Fe_2O_3 and Fe_3O_4) were induced by air oxidation. As the main mechanism passes from dissolution to oxidation for the AISI H13 HVOF coating, the corrosive process is decelerated. Even the soldering forces being higher due morphology of the intermetallic formed, the corrosion was decelerated. Oxidation of

the particles during deposition process could be used to enhance the coating resistance with respect to molten aluminum corrosion. Additionally, some studies have shown these iron oxides being used as a solid lubricant for HVOF coatings (ŻÓRAWSKI *et al.*, 2017 AND ZÓRAWSKI; SKRZYPEK, 2013).

Figure 41 - SEM and EDS images of diffusional layers observed on the H13 HVOF sample in die soldering tests after 30 minutes in molten aluminum at 720 °C.

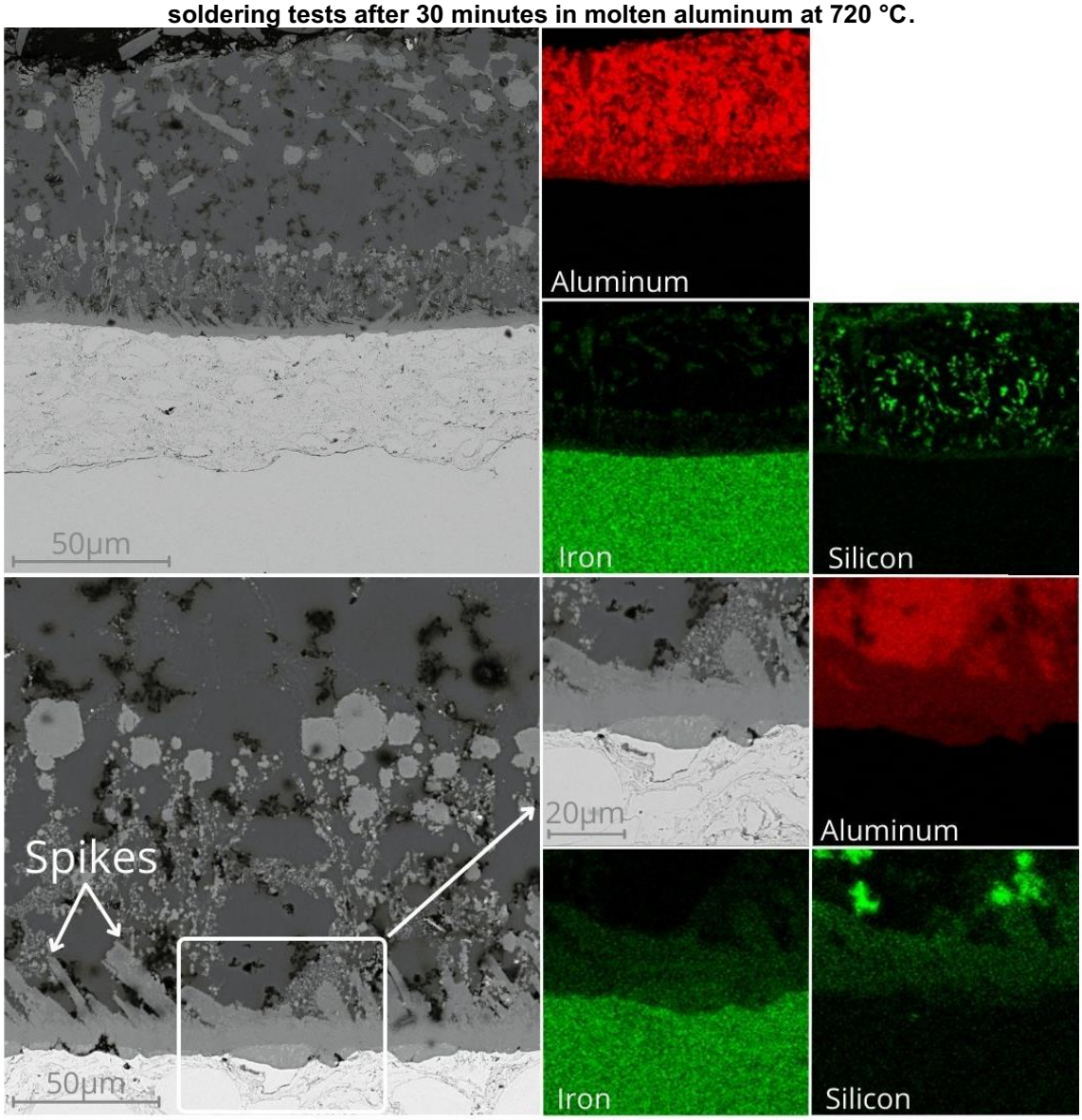

Reference: Author

Figure 42 - HVOF of AISI H13 after 30 minutes of corrosion in molten metal. (a) Diffusional layers, (b) oxide layers acting as protection and (c) metallic particles being dissolved.

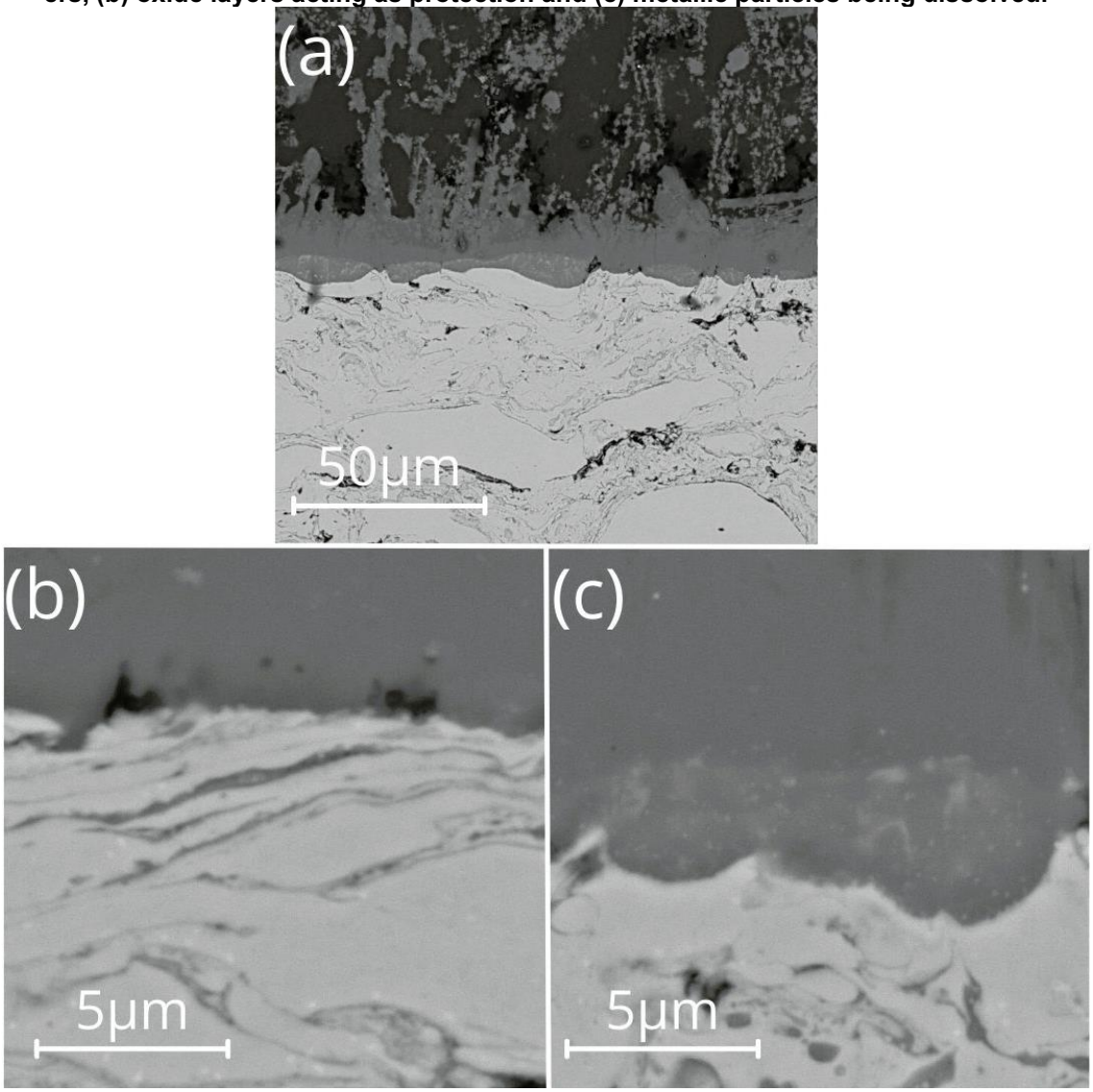

Reference: Author

To summarize, the soldering mechanism for AISI H13 deposited via HVOF is a mixture of dissolution of metallic phases and reaction of the oxides formed during the spraying process. Spiky intermetallics are observed between the intermetallic structure and aluminum molten alloy, likely due to the non-homogeneous diffusion process. A smaller amount of iron is consumed when compared to bulk material, as most of the iron content is concentrated in the inner diffusion layer. Therefore, even with the corrosion rate being lower than H13 tool steel, the soldering effect is strong because of the spiking formation.

4.4.4 HVOF of Cr3C2 25NiCr

Figure 43 and figure 44 show the cross-section images of the H13 tool steel with Cr_3C_2 25NiCr HVOF coating succeeding die soldering tests after 10 and 30 minutes in molten aluminum at 720 °C. It is possible to observe that the initial corrosion depth is small after 10 minutes and suddenly grows after 30 minutes. Also, the die soldering extraction resistance at 10 minutes is higher only than AlCrN PVD coating. However, the extraction resistance became the highest value with the increase in time.

The initial detachment of chromium carbides from the matrix started after 10 minutes at 720 °C. This mechanism is more evident after 30 minutes at 720 °C, shown in figure 45. After the dissolution, an Al-Si-Cr phase was formed. The measured intermetallic and coating compositions are shown in table 10. After breaking the chemical bonding of the chromium carbide, the aluminum forms an intermetallic phase, and the carbon is free to diffuse via interstitials. Figure 60, in appendix A, shows the amount of carbon being diffused.

Additionally, the intermetallic creates spikes, with different morphology than observed in the H13 HVOF. In this case, the spikes are smaller and in higher density. These spikes create a strong bonding by increasing the surface area and, consequently, the contact of the intermetallic and aluminum. Furthermore, the hardness of the intermetallic layer has shown a value of 1,235.8 ± 92.14 HV_{500g}.

Figure 43 - Cross section of Cr_3C_2 25NiCr after 10 minutes of corrosion in molten metal.

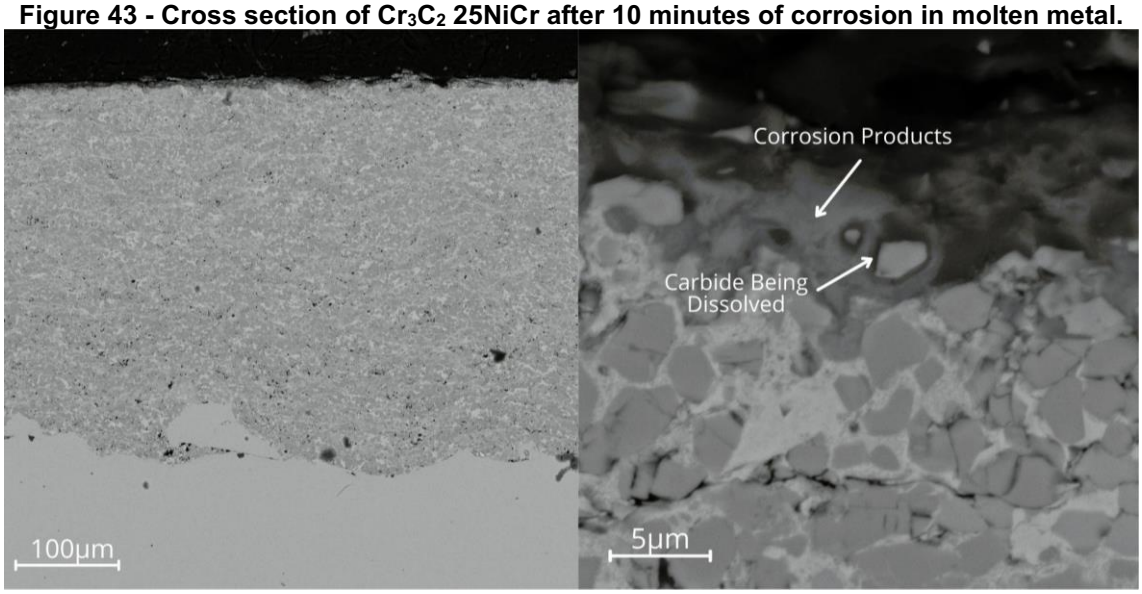

Reference: Author

Figure 44 - Cross section of Cr3C2 25NiCr after 30 minutes of corrosion in molten metal.

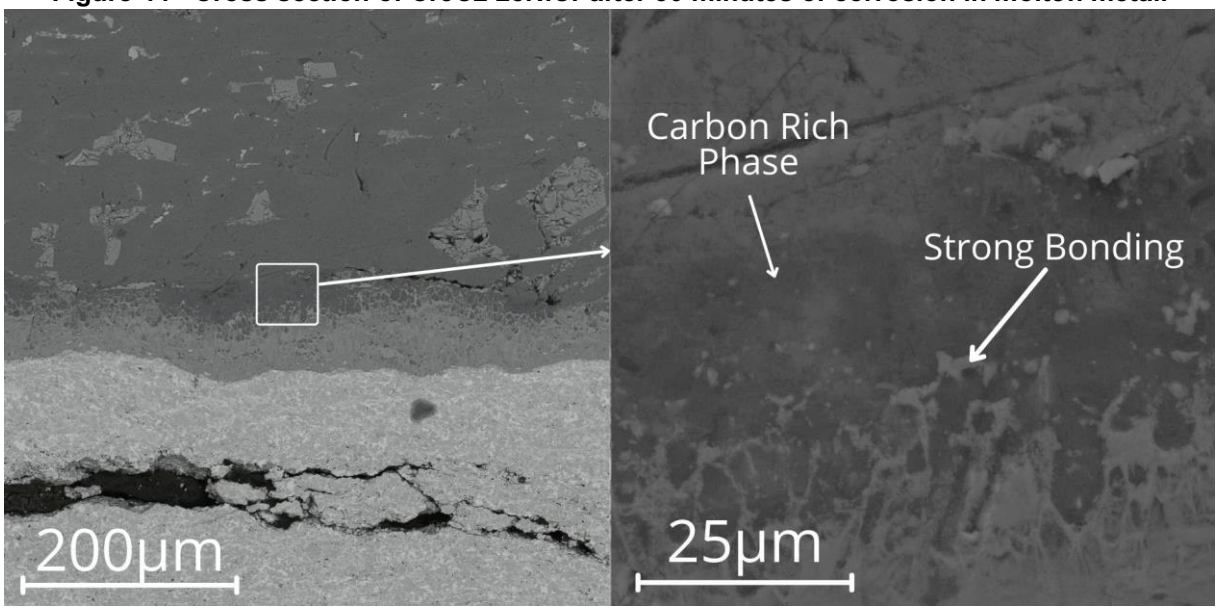

Reference: Author

Figure 45 - (a) Carbide detachment and dissolution and (b) linear EDS for Cr_3C_2 25NiCr after 30 minutes of corrosion in molten aluminum.

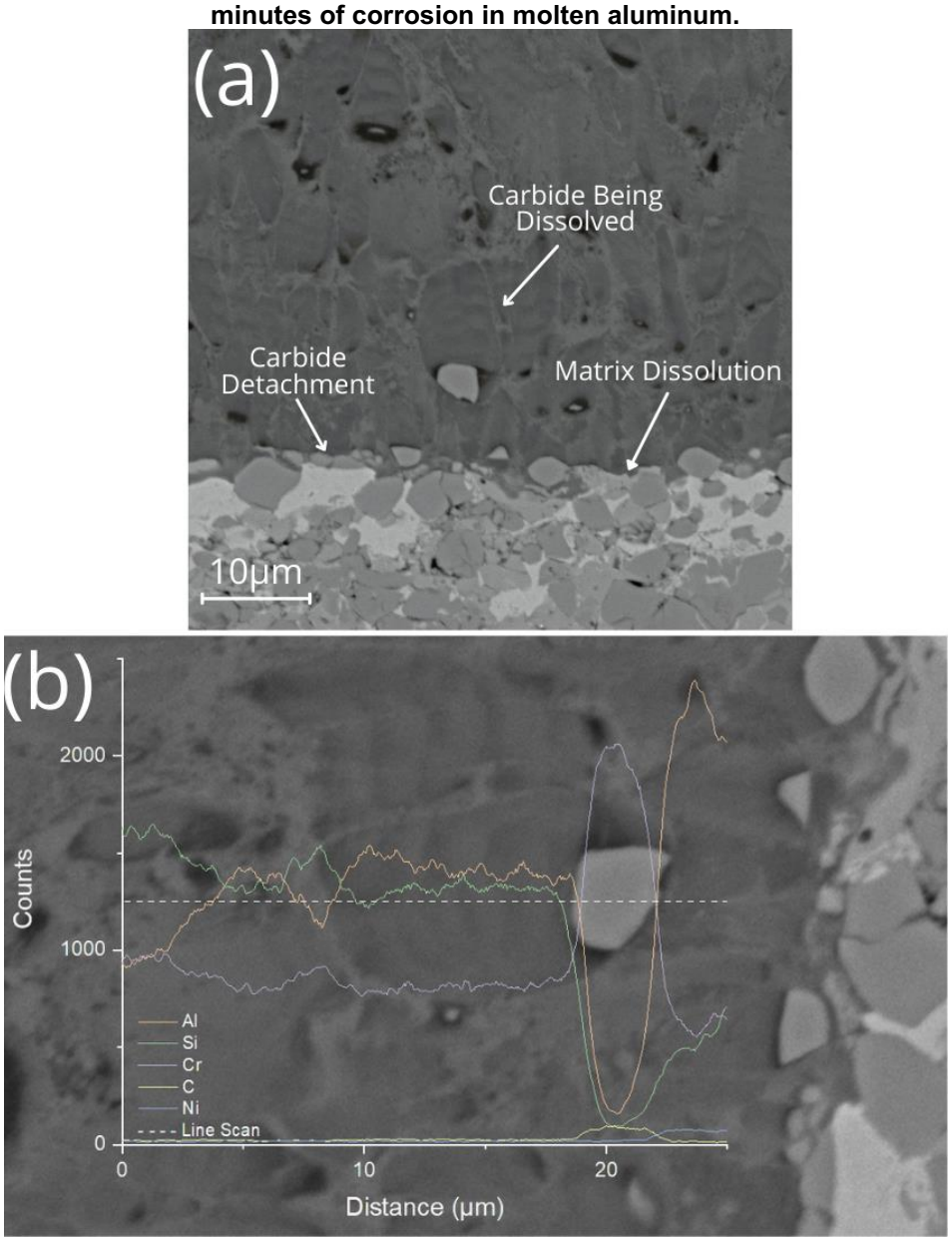

Reference: Author

Table 10 - Chemical composition in weight percentage of the Cr_3C_2 25NiCr HVOF coating and the intermetallic layer formed after corrosion for 30 minutes in molten A383 at 720 °C.

	Cr (wt%)	Ni (wt%)	C (wt%)	Al (wt%)	Si (wt%)
Nominal Cr_3C_2 25NiCr	65.9	20	14.1	*	*
Measured Cr_3C_2 25NiCr	64.05 ± 2.33	23.5 ± 2.97	12.2 ± 0.7	*	*
Intermetallic	35.35 ± 0.78	0.4 ± 0.1	7.85 ± 0.91	26.0 ± 0.99	30.2 ± 1.41

Reference: Author

It was seen that the molten aluminum first dissolves the NiCr metallic matrix of the coating. After dissolving it, the chromium carbide reacts with the aluminum, losing its chromium and creating a tough intermetallic interface. The interface also shows spikes, which contributes to the adhesion phenomena. After chromium carbide dissolution, the carbon diffuses fasters, and it is found in the molten aluminum. As the carbides move by concentration gradient, the molten aluminum degrades its chemical bond. As the chromium carbide has shown a superior resistance, compared to the metallic matrix, a better relation of carbide/matrix may be found.

5 CONCLUSIONS

Corrosion and soldering properties for different coatings were evaluated and compared to AISI H13. The mechanisms of corrosion and soldering were evaluated and described using SEM and EDS analyses, and the main conclusions are shown below.

- Corrosion has been decelerated for all coatings. None of the coatings were able to withstand the total of 40 hours of corrosion. After coating failure, AlCrN PVD and H13 HVOF showed a similar behavior compared to H13 tool steel. The Cr_3C_2 25NiCr coating showed a higher adhesion of intermetallics.
- AlCrN PVD coating has shown the best performance regarding soldering. A strong adhesion was observed for Cr_3C_2 25NiCr coating, even having relatively low corrosion rate. The HVOF H13 coating has shown a better corrosion resistance compared to AISI H13. Nevertheless, the soldering increased. For both HVOF coatings, a spiking phenomenon, due to non-homogeneous corrosion, increased soldering extraction stresses.
- Corrosion/soldering mechanisms were described for all the surfaces. The carbide detachment followed by aluminum corrosion was described in detail for the Cr_3C_2 25NiCr coating. Also, the oxides in the H13 HVOF coating decreased the corrosion rate. However, the spiking phenomenon was the main cause of soldering for both HVOF coatings by increasing the surface contact area of the intermetallics and the aluminum. Regarding AlCrN PVD coating, the decrease in nitrogen and growth of defects were attributed as the main mechanisms of coating degradation.
- The proposed methodology to evaluate soldering has shown to be extremely solid by the amount of information given. It was possible to evaluate soldering forces, corrosion/soldering mechanisms, corrosion rate, and intermetallic formation. When combined with corrosion analysis, the corrosive behavior of the surface was evaluated, and mechanisms were proposed.
- Nanolayers of iron oxide were found in the H13 HVOF coating. These nanolayers were capable of retard corrosion. The increase of the oxide content could be used to improve the corrosion resistance to a point where the spiking effect would be less significant. Finding a relation between the amount of oxidation and mechanical resistance of the coating by changing parameters could improve the resistance of

the coating. Whereas for C_3C_2 25NiCr, the matrix has shown a smaller resistance than the carbides. A better relation of carbide/matrix may be found.

REFERENCES

ABU-WARDA, N.; LÓPEZ, M. D.; UTRILLA, M. V. High temperature corrosion and wear behavior of HVOF-sprayed coating of Al2O3-NiAl on AISI 304 stainless steel. **Surface and Coatings Technology**, v. 359, p. 35–46, 2019.

ADESINA, A. Y.; IQBAL, Z.; AL-BADOUR, F. A.; GASEM, Z. M. Mechanical and tribological characterization of AlCrN coated spark plasma sintered W-25%Re-Hfc composite material for FSW tool application. **Journal of Materials Research and Technology**, v. 8, n. 1, p. 436–446, 2019.

ASTM. E384 - Microindentation Hardness of Materials. **ASTM standard**, v. E384, p. 1–24, 1999.

ASTM. ASTM E2109-01 - Standard test methods for determining area percentage porosity in thermal sprayed coatings. **ASTM standard**, v. E2109-01, p. 1–8, 2014.

BARONINS, J.; ANTONOV, M.; BEREZNEV, S.; RAADIK, T.; HUSSAINOVA, I. Raman spectroscopy for reliability assessment of multilayered AlCrN coating in tribo-corrosive conditions. **Coatings**, v. 8, n. 7, 2018.

BERGER, L. M. Coatings by Thermal Spray. **Comprehensive Hard Materials**. v. 1, p.471–506, 2014.

BIAVA, G. **Estudo da Resistência à Corrosão a Baixa e Alta Temperatura de Revestimentos PVD Depositados em Uma Superliga de Níquel**, 2019. Thesis (Master's degree in Mechanical Manufacturing and Materials) - Postgraduate Program in Mechanical Engineering, Federal University of Technology, Ponta Grossa, 2019.

BIAVA, G.; DE ARAUJO FERNANDES SIQUEIRA, I. B.; VAZ, R. F.; *et al.* Evaluation of high temperature corrosion resistance of CrN, AlCrN, and TiAlN arc evaporation PVD coatings deposited on Waspaloy. **Surface and Coatings Technology**, v. 438, p. 1-15, 2022.

BOLELLI, G.; BERGER, L. M.; BÖRNER, T.; *et al.* Sliding and abrasive wear behaviour of HVOF- and HVAF-sprayed Cr3C2-NiCr hardmetal coatings. **Wear**, v. 358–359, p. 32–50, 2016.

BONOLLO, F.; GRAMEGNA, N.; TIMELLI, G. High-pressure die-casting: Contradictions and challenges. **Jom**, v. 67, n. 5, p. 901–908, 2015.

BORREGO, L. P.; PIRES, J. T. B.; COSTA, J. M.; FERREIRA, J. M. Mould steels repaired by laser welding. **Engineering Failure Analysis**, v. 16, n. 2, p. 596–607, 2009.

CALLISTER, W. D.; DAVID, R. J. G. **Materials Science and Engineering**.9. ed. 2014.

CHATHA, S. S.; SIDHU, H. S.; SIDHU, B. S. High temperature hot corrosion behaviour of NiCr and Cr 3C 2-NiCr coatings on T91 boiler steel in an aggressive environment at 750°C. **Surface and Coatings Technology**, v. 206, p. 3839–3850, 2012.

CHEN, G.; WANG, J.; FAN, H.; *et al.* Combat molten aluminum corrosion of AISI H13 steel by low-temperature liquid nitrocarburizing. **Journal of Alloys and Compounds**, v. 776, p. 702–711, 2019.

CHEN, G.; XUE, L.; WANG, J.; *et al.* Investigation of surface modifications for combating the molten aluminum corrosion of AISI H13 steel. **Corrosion Science**, v. 174, 2020.

DADIĆ, Z.; ŽIVKOVIĆ, D.; ČATIPOVIĆ, N. Tribological wear mechanisms of molds for high pressure die casting. **Metalurgija**, v. 55, n. 2, p. 249–252, 2016.

DONNET, C.; ERDEMIR, A. Solid lubricant coatings: Recent developments and future trends. **Tribology Letters**, v. 17, n. 3, p. 389–397, 2004.

EL-ESKANDARANY, M. S. Utilization of ball-milled powders for surface protective coating. **Mechanical Alloying**. p.309–334, 2020.

EUROPEAN ALUMINIUM ASSOCIATION. Aluminium Design for Cost Optimization. , p. 1–47, 2011.

FAZLALIPOUR, F.; NAGHASHNEJAD, M.; NIKI NUSHARI, M. Evaluation of adhesion and erosion/corrosion resistance of nano-composite and nano-multilayer thin films in molten aluminum alloy. **SN Applied Sciences**, v. 1, n. 10, 2019.

FOTOVVATI, B.; NAMDARI, N.; DEHGHANGHADIKOLAEI, A. On coating techniques for surface protection: A review. **Journal of Manufacturing and Materials Processing**, v. 3, n. 1, 2019.

FUJII, H.; NAKAE, H.; OKADA, K. Interfacial reaction wetting in the boron nitride/molten aluminum system. **Acta Metallurgica Et Materialia**, v. 41, n. 10, p. 2963–2971, 1993.

GHADAMI, F.; AGHDAM, A. Improvement of high velocity oxy-fuel spray coatings by thermal post-treatments: A critical review. **Thin Solid Films**, 31. May 2019.

GILEWICZ, A.; JEDRZEJEWSKI, R.; MYSLINSKI, P.; WARCHOLINSKI, B. Structure, Morphology, and Mechanical Properties of AlCrN Coatings Deposited by Cathodic Arc Evaporation. **Journal of Materials Engineering and Performance**, v. 28, n. 3, p. 1522–1531, 2019.

GOBBER, F.; PISA, A.; UGUES, D.; *et al.* Study of the Effect of Surface—Roughness of Dies and Tooling for HPDC on Soldering. Minerals, Metals and Materials Series. **Anais...** . v. Part F4, p.977–981, 2018.

GOBBER, F. S.; UGUES, D.; ROSSO, M. Analysis of the influence of surface finishing on the performances of dies for hpdc. Solid State Phenomena. v. 285 SSP, p.459–463, 2019.

GULIZIA, S.; JAHEDI, M. Z.; DOYLE, E. D. Performance evaluation of PVD coatings for high pressure die casting. **Surface and Coatings Technology**, v. 140, p. 200–205, 2001.

HAN, Q.; VISWANATHAN, S. Analysis of the Mechanism of Die Soldering in Aluminum Die Casting. **Metallurgical and Materials Transactions A**, v. 34A, 2003.

HUGH BAKER; HIROAKI OKAMOTO; SCOTT D. HENRY; *et al.* **Alloy Phase Diagrams**. ASM International, 1992.

KANDEVA, M.; VENCL, A.; KARASTOYANOV, D. **Advanced Tribological Coatings for Heavy-Duty Applications:** Case Studies. 2016.

KHAN, F. F.; BAE, G.; KANG, K.; *et al.* Evaluation of die-soldering and erosion resistance of high velocity oxy-fuel sprayed MoB-based cermet coatings. **Journal of Thermal Spray Technology**, v. 20, n. 5, p. 1022–1034, 2011.

KOVAČEVIĆ, L.; TEREK, P.; MILETIĆ, A.; *et al.* Industrial evaluation of duplex PVD hard coatings for HPDC. **Journal of the Brazilian Society of Mechanical Sciences and Engineering**, v. 40, n. 5, 2018.

KUMAR, S.; HANDA, A.; KUMAR, R. Overview of Wire Arc Spray Process: A Review. **A Journal of Composition Theory**, v. 12, n. 7, p. 900–907, 2019.

KURODA, S.; KAWAKITA, J.; WATANABE, M.; KATANODA, H. Warm spraying - A novel coating process based on high-velocity impact of solid particles. **Science and Technology of Advanced Materials**, v. 9, p. 1–17, 2008.

LIMA, C. C.; TREVISAN, R. **Aspersão Térmica : Fundamentos e Aplicação.** 2° ed. São Paulo, 2007.

LIU, A.; DENG, J.; CUI, H.; CHEN, Y.; ZHAO, J. Friction and wear properties of TiN, TiAlN, AlTiN and CrAlN PVD nitride coatings. **International Journal of Refractory Metals and Hard Materials**, v. 31, p. 82–88, 2012.

LIU, T.; KARKKAINEN, M.; NASTAC, L.; *et al.* Iron-rich intermetallics in high pressure die cast A383 aluminum alloys. **Intermetallics**, v. 126, 2020.

LIU, Y.; FISCHER, T. E.; DENT, A. Comparison of HVOF and plasma-sprayed alumina/titania coatings - Microstructure, mechanical properties and abrasion behavior. **Surface and Coatings Technology**, v. 167, n. 1, p. 68–76, 2003.

LÓPEZ, A. J.; RAMS, J. Protection of carbon steel against molten aluminum attack and high temperature corrosion using high velocity oxygen-fuel WC-Co coatings. **Surface and Coatings Technology**, v. 262, p. 123–133, 2015.

LUGSCHEIDER, * E; BARIMANI, C.; GUERREIRO, S.; BOBZIN, K. Corrosion tests of PVD coatings with die lubricant used for Al high-pressure die-casting dies. **Surface and Coatings Technology**, v. 108-109, p. 408–412, 2003.

MATYSIK, P.; JÓZWIAK, S.; CZUJKO, T. Characterization of low-symmetry structures from phase equilibrium of Fe-Al system-microstructures and mechanical properties. **Materials**, v. 8, n. 3, p. 914–931, 2015.

MISHRA, S. K.; TALWAR, D.; SINGH, K.; *et al.* Micromechanical characterization and dynamic wear study of DC-Arc coated cemented carbide cutting tools for dry titanium turning. **Ceramics International**, v. 47, n. 22, p. 31798–31810, 2021.

MIZUNO, H.; KITAMURA, J. MoB/CoCr cermet coatings by HVOF spraying against erosion by molten Al-Zn alloy. **Journal of Thermal Spray Technology**, v. 16, n. 3, p. 404–413, 2007.

NADCA DIE MATERIALS COMMITTEE. **Special Quality Die Steel & Heat Treatment Acceptance Criteria for Die Casting Dies**. 2006.

NING, A.; YUE, S.; GAO, R.; LI, L.; GUO, H. Influence of tempering time on the behavior of large carbides' coarsening in aisi h13 steel. **Metals**, v. 9, n. 12, 2019. MDPI AG.

OERLIKON METCO. Material Product Data Sheet Tungsten Carbide – 12 % Cobalt Sintered and Crushed Powders for Thermal Spray. , 2014.

PERSSON, A. **On Tool Failure in Die Casting**, 3. Jun. 2003. Dissertation, Uppsala: Uppsala University.

PETER, I.; ROSSO, M.; GOBBER, F. S. Study of protective coatings for aluminum die casting molds. **Applied Surface Science**, v. 358, p. 563–571, 2015.

PICAS, J. A.; PUNSET, M.; MENARGUES, S.; MARTÍN, E.; BAILE, M. T. Microstructural and tribological studies of as-sprayed and heat-treated HVOF Cr3C2-CoNiCrAlY coatings with a CoNiCrAlY bond coat. **Surface and Coatings Technology**, v. 268, p. 317–324, 2015.

PINZÓN, A. V.; URREGO, K. J.; GONZÁLEZ-HERNÁNDEZ, A.; RINCÓN ORTIZ, M.; VARGAS GALVIS, F. Corrosion protection of carbon steel by alumina-titania ceramic coatings used for industrial applications. **Ceramics International**, v. 44, n. 17, p. 21765–21773, 2018.

PORTER, D. A.; EASTERLING, K. E.; SHERIF, M. Y. **Phase Transformation in Metals and Alloys**. Third ed. 2009.

PUKASIEWICZ, A. G. M. High Pressure Die Casting Die Damaged by Soldering. Author's Photograph. , 2021.

RICCARDO, G.; RIVOLTA, B.; GORLA, C.; CONCLI, F. Cyclic behavior and fatigue resistance of AISI H11 and AISI H13 tool steels. **Engineering Failure Analysis**, v. 121, 2021.

SAHA, R.; NIX, W. D. Effects of the substrate on the determination of thin film mechanical properties by nanoindentation. **Acta Materialia**, v. 50, n. 1, p. 23-38, 2002.

SALMAN, A. **Study of Titanium based Composite Coatings for Resistance against Molten Aluminium Soldering on H13 Tool Steel**, 2011. Thesis (Doctor of Philosophy in Engineering), The University of Waikato, Hamilton, 2011.

SALMAN, A.; GABBITAS, B. L.; CAO, P.; ZHANG, D. L. The performance of thermally sprayed titanium based composite coatings in molten aluminium. **Surface and Coatings Technology**, v. 205, n. 21–22, p. 5000–5008, 2011.

SALMAN, A.; GABBITAS, B.; LI, J.; ZHANG, D. Tribological properties of thermally sprayed TiAl-Al2O 3 composite coating. **IOP Conference Series: Materials Science and Engineering**, v. 4, 2009.

SEQUEIRA, C. A. C. **High Temperature Corrosion: Fundamentals and Engineering**. 1. ed. 2018.

SHIVALINGAIAH, K.; SRIDHAR, K. S.; SETHURAM, D.; KOPPAD, K. V. S. M. P. G.; RAMESH5, C. S. HVOF sprayed Inconel 718/cubic boron nitride composite coatings: microstructure, microhardness and slurry erosive behaviour. **Materials Research Express**, v. 6, n. 12, 2020.

SIDHU, M. S. **Liquid Aluminium Corrosion Characteristics of Cast Iron and Steel**, 2012. Thesis (Doctor of Philosophy in Mechanical Engineering) - Department of Mechanical Engineering, University of Canterbury, Christchurch, 2012.

SINGH, G.; KAUR, M. High-temperature wear behaviour of HVOF sprayed 65% (NiCrSiFeBC)−35% (WC–Co) coating. **Surface Engineering**, v. 36, n. 11, p. 1139–1155, 2019.

SONG, J.; DENOUDEN, T.; HAN, Q. Mechanisms of soldering formation on coated core pins. **Metallurgical and Materials Transactions A: Physical Metallurgy and Materials Science**, v. 43, n. 2, p. 415–421, 2012.

TAKAHASHI, R. J.; ASSIS, J. M. K.; PIORINO NETO, F.; REIS, D. A. P. Heat treatment for TGO growth on NiCrAlY for TBC application. **Materials Research Express**, v. 6, n. 12, 2019.

TEREK, P.; KOVAČEVIĆ, L.; MILETIĆ, A.; *et al.* Improved ejection test for evaluation of soldering tendency of cast alloy to die core materials. **Journal of Materials Processing Technology**, v. 266, p. 114–124, 2019.

TORRES-GARZA, A.; QUIÑONES-SALINAS, M. A.; BARRAGAN-SERNA, I. A.; MERCADO-SOLIS, R. D. The design of a laboratory test machine to simulate thermal fatigue in hot-working tool steels. **Materials Performance and Characterization**, v. 3, n. 2, p. 229–244, 2014.

VARDELLE, A.; MOREAU, C.; AKEDO, J.; *et al.* The 2016 Thermal Spray Roadmap. **Journal of Thermal Spray Technology**, v. 25, n. 8, p. 1376–1440, 2016.

VICARIO, I.; IDOIAGA, J. K.; ARRATIBEL, E.; *et al.* Development of HPDC Advanced Dies by Casting with Reinforced Tool Steels. **International Journal of Manufacturing Engineering**, v. 2015, p. 1–10, 2015.

WANG, B.; BOURNE, G. R.; KORENYI-BOTH, A. L.; *et al.* Method to evaluate the adhesion behavior of aluminum-based alloys on various materials and coatings for lube-free die casting. **Journal of Materials Processing Technology**, v. 237, p. 386–393, 2016.

WANG, X.; WANG, J.; GAO, Z.; XIA, D. H.; HU, W. Tempering effects on the microstructure and properties of submerged arc surfacing layers of H13 steel. **Journal of Materials Processing Technology**, v. 269, p. 26–34, 2019.

WU, W.; CHEN, W.; YANG, S.; *et al.* Design of AlCrSiN multilayers and nanocomposite coating for HSS cutting tools. **Applied Surface Science**, v. 351, p. 803–810, 2015.

YANG, N. NAN; SHEN, P.; YANG, B.; GUO, R. FEN; JIANG, Q. CHUAN. Significant improvement in the wettability of ZrO2 by molten Al under the application of a direct current. **Materials and Design**, v. 111, p. 158–163, 2016.

ZHANG, X. M.; CHEN, W. P. Review on corrosion-wear resistance performance of materials in molten aluminum and its alloys. **Transactions of Nonferrous Metals Society of China (English Edition)**, v. 25, n. 6, p. 1715–1731, 2015.

ZHANG, X.; ZHANG, L.; HUANG, Z. Microstructure Characteristics and Properties of HVOF Sprayed Ni-Based Alloy Nano-h-BN Self-Lubricating Composite Coatings. **Advances in Tribology**, v. 2015, p. 1-6, 2015.

ZHOU, W.; ZHOU, K.; LI, Y.; DENG, C.; ZENG, K. High temperature wear performance of HVOF-sprayed Cr 3 C 2 -WC-NiCoCrMo and Cr 3 C 2 -NiCr hardmetal coatings. **Applied Surface Science**, v. 416, p. 33–44, 2017.

ZHU, H. **Dissolution Rate and Mechanism of Metals in Molten Aluminum Alloy A380**, 2014. Thesis (Master of Science), Purdue University, West Lafayette, 2014.

ZHU, H.; GUO, J.; JIA, J. Experimental study and theoretical analysis on die soldering in aluminum die casting. **Journal of Materials Processing Technology**, v. 123, p. 229–235, 2001.

ZHU, L.; CUI, Y.; CAO, J.; *et al.* Effect of TIG remelting on microstructure, corrosion and wear resistance of coating on surface of 4Cr5MoSiV1 (AISI H13). **Surface and Coatings Technology**, v. 405, p. 1-13, 2021.

ZHU, Y.; SCHWAM, D.; WALLACE, J. F.; BIRCEANU, S. Evaluation of soldering, washout and thermal fatigue resistance of advanced metal materials for aluminum die-casting dies. **Materials Science and Engineering A**, v. 379, n. 1–2, p. 420–431, 2004.

ŻÓRAWSKI, W.; MAKRENEK, M.; GÓRAL, A.; ZIMOWSKI, S. HVOF Sprayed Nanostructured Composite Coatings with a Reduced Friction Coefficient. **Tribologia**, p. 139–147, 2017.

ZÓRAWSKI, W.; SKRZYPEK, S. J. Tribological properties of plasma and HVOF-sprayed NiCrBSi-Fe2O3 composite coatings. **Surface and Coatings Technology**, v. 220, p. 282–289, 2013.

Appendix A – Scanning electron microscopy and energy dispersive spectroscopy auxiliar data

Figure 46 - Surface EDS after extraction of the aluminum ring for simple cast AISI H13.

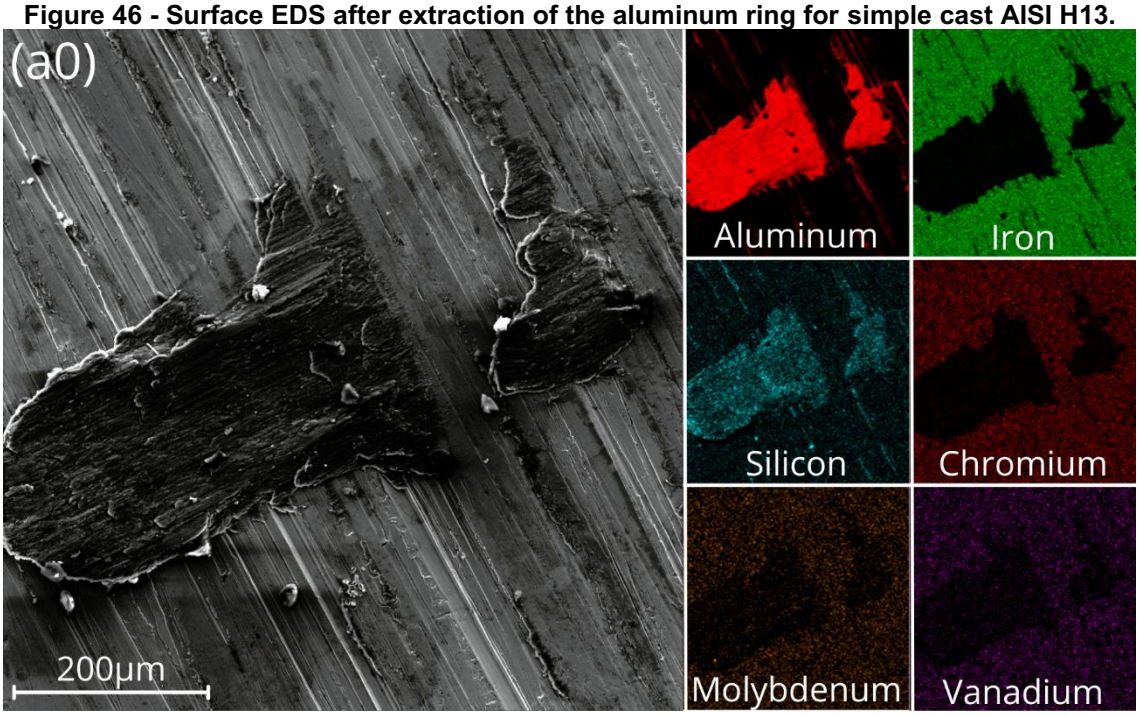

Reference: Author

Figure 47 - Surface EDS after extraction of the aluminum ring for AISI H13 after 10 minutes in molten aluminum.

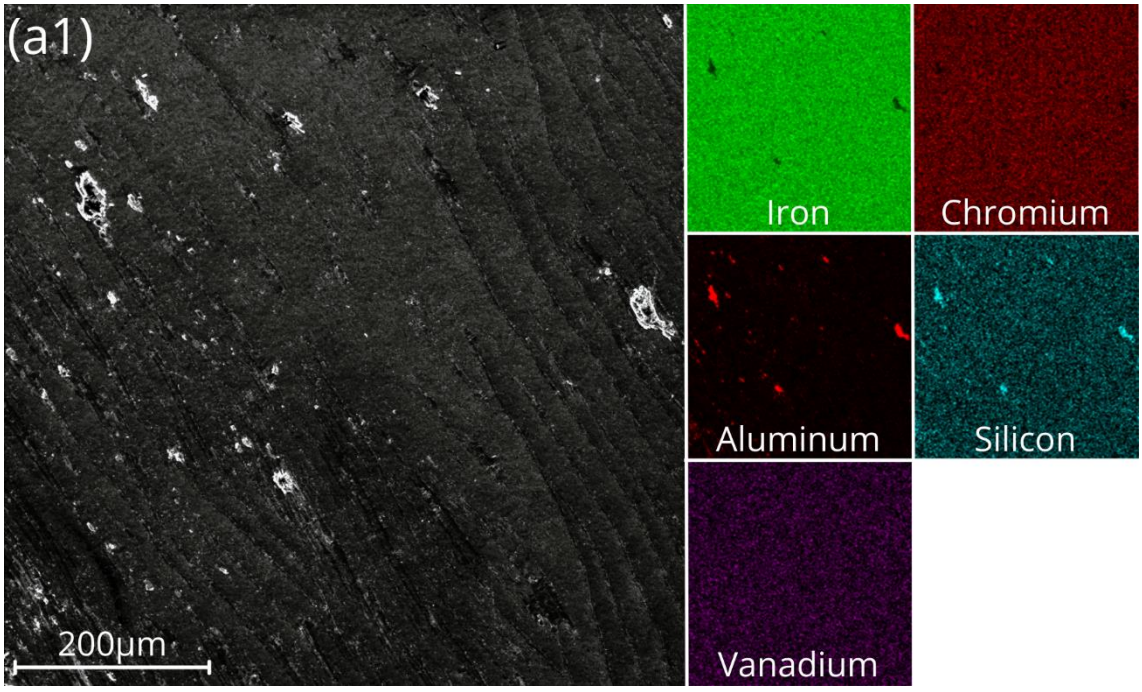

Reference: Author

Figure 48 - Surface EDS after extraction of the aluminum ring for AISI H13 after 30 minutes in molten aluminum.

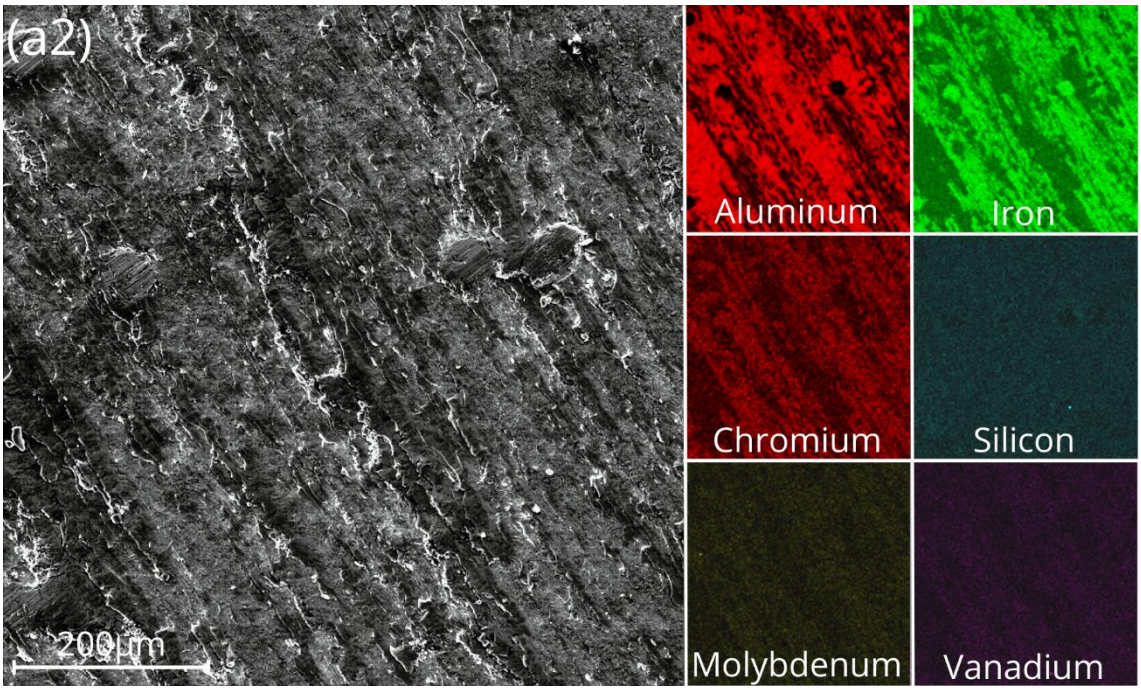

Reference: Author

Figure 49 - Surface EDS after extraction of the aluminum ring for simple cast AISI H13 with AlCrN PVD coating.

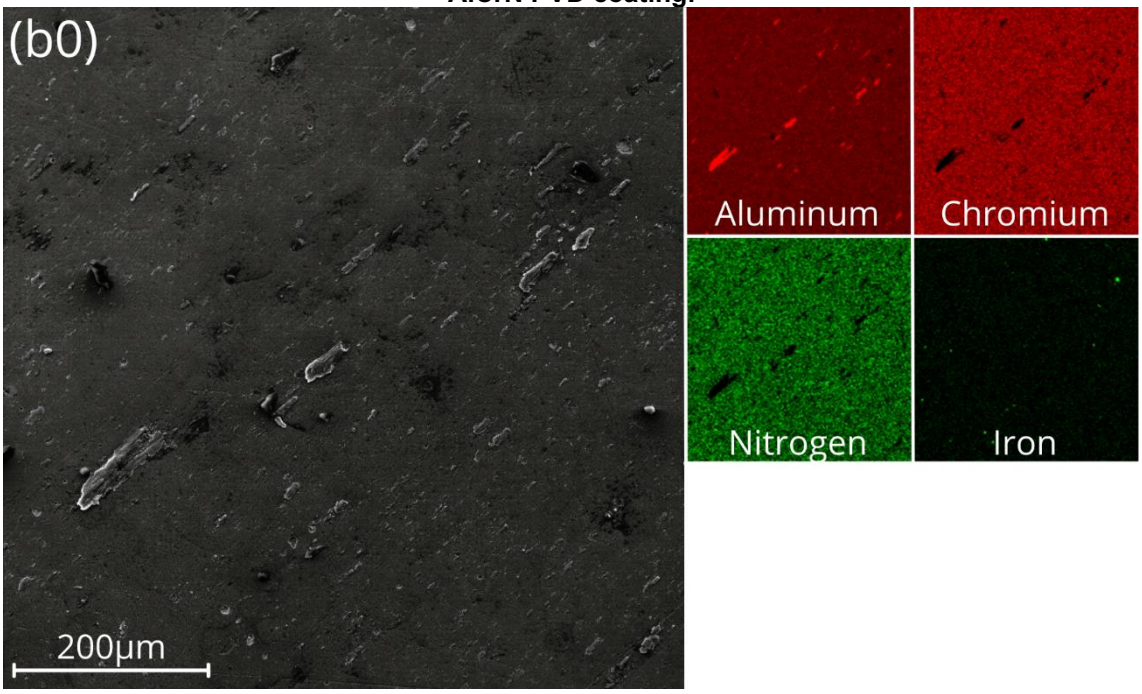

Reference: Author

Figure 50 - Surface EDS after extraction of the aluminum ring for AISI H13 with AlCrN PVD coating after 10 minutes in molten aluminum.

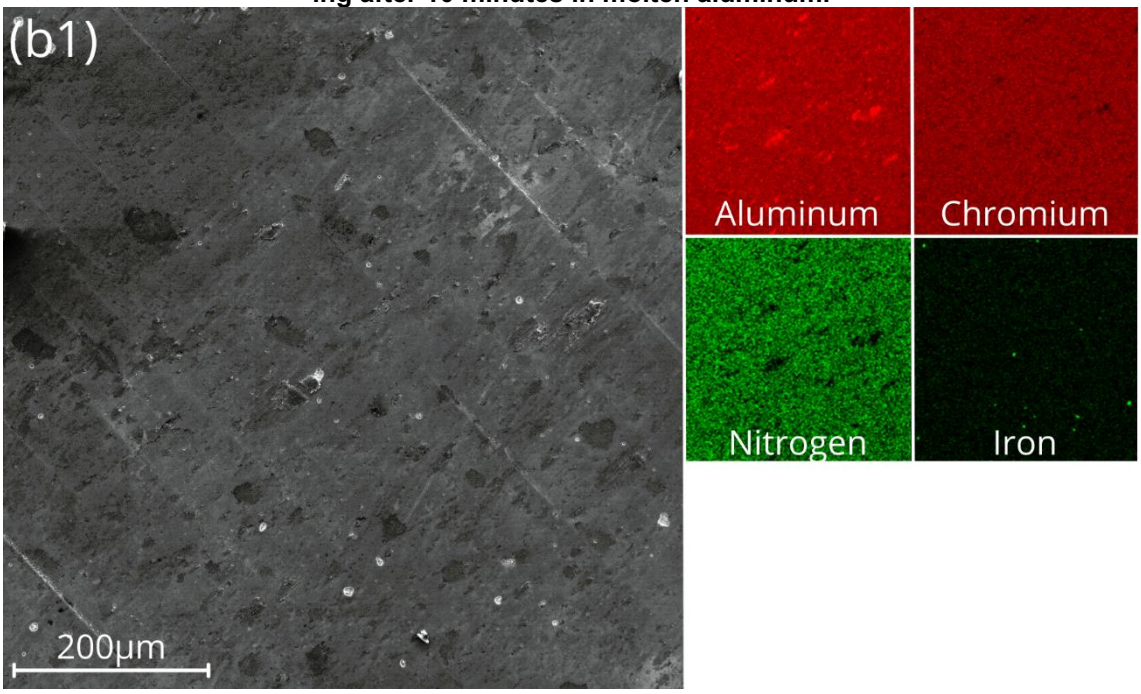

Reference: Author

Figure 51 - Surface EDS after extraction of the aluminum ring for AISI H13 with AlCrN PVD coating after 30 minutes in molten aluminum.

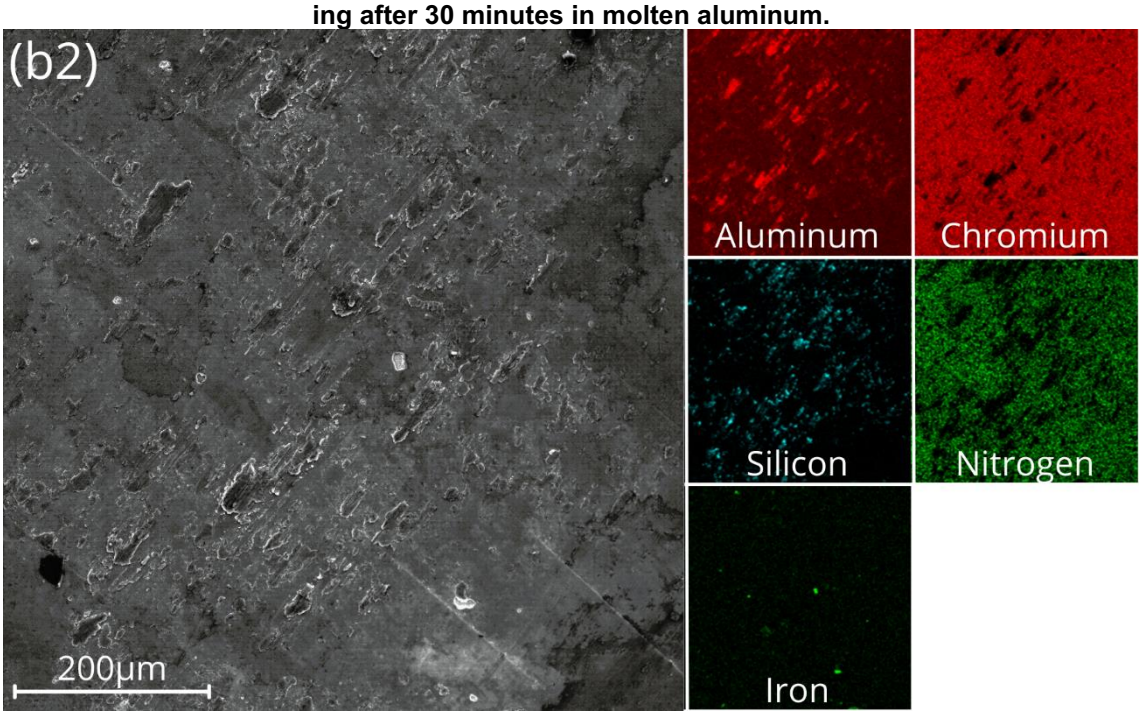

Reference: Author

Figure 52 - Surface EDS after extraction of the aluminum ring for simple cast HVOF of AISI H13.

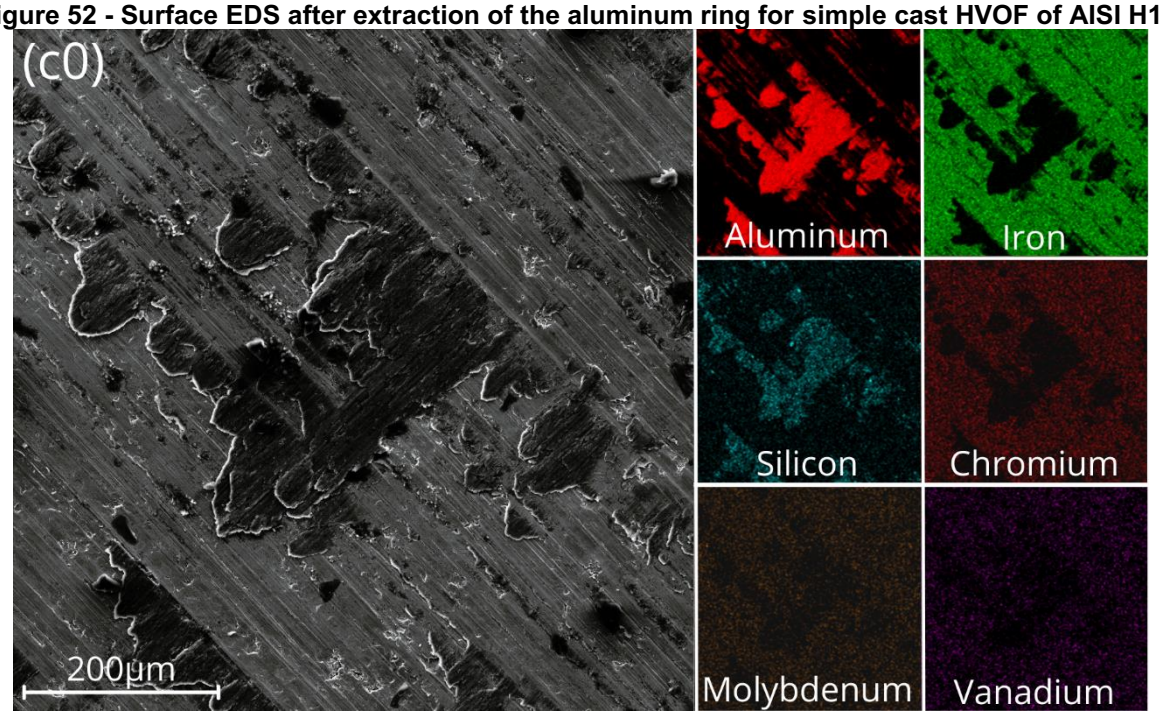

Reference: Author

Figure 53 - Surface EDS after extraction of the aluminum ring for HVOF of AISI after 10 minutes in molten aluminum.

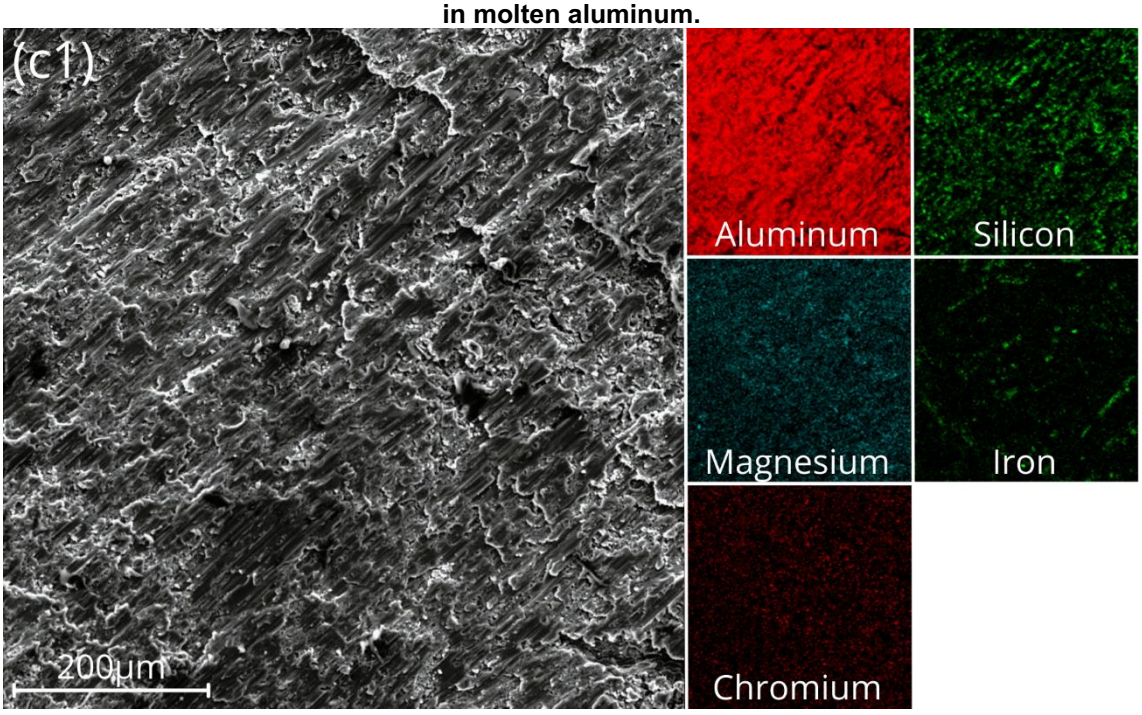

Reference: Author

Figure 54 - Surface EDS after extraction of the aluminum ring for HVOF of AISI after 30 minutes in molten aluminum.

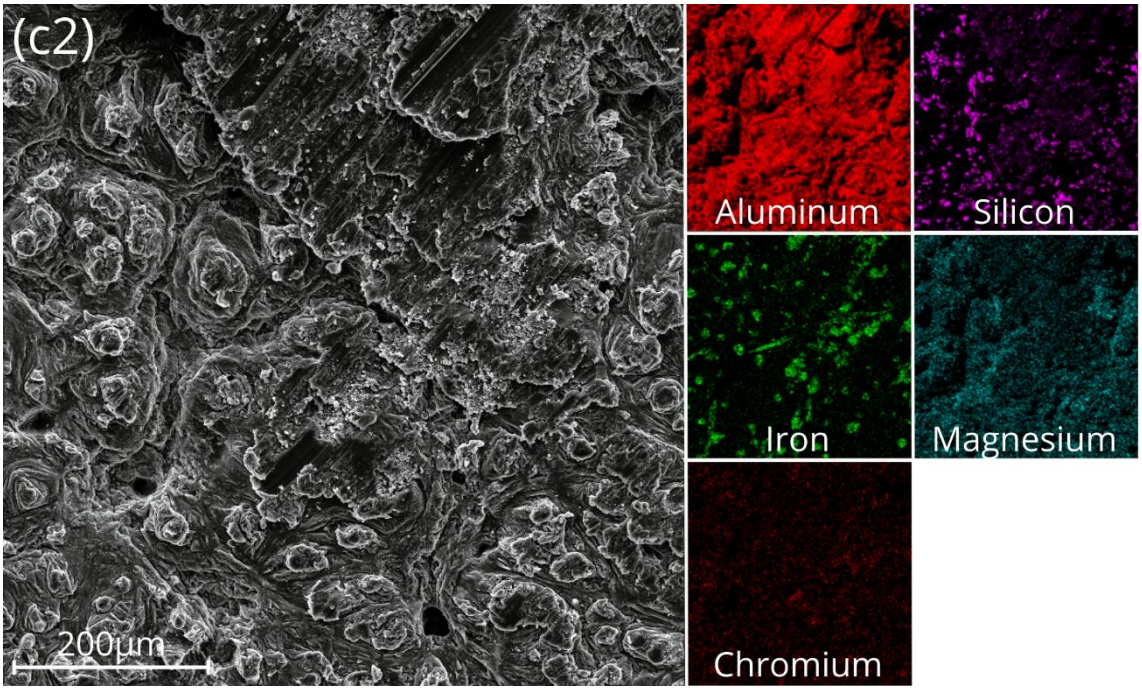

Reference: Author

Figure 55 - Surface EDS after extraction of the aluminum ring for simple cast HVOF of Cr_3C_2 25NiCr.

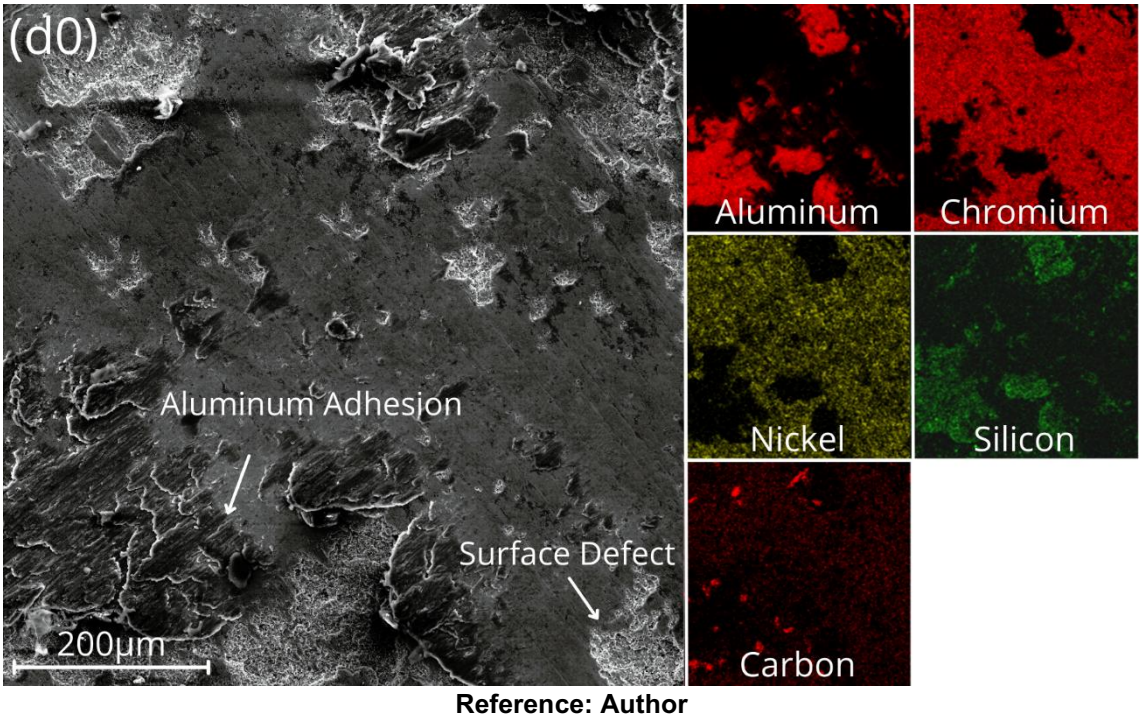

Reference: Author

Figure 56 - Surface EDS after extraction of the aluminum ring for HVOF of Cr_3C_2 25NiCr after 10 minutes in molten aluminum.

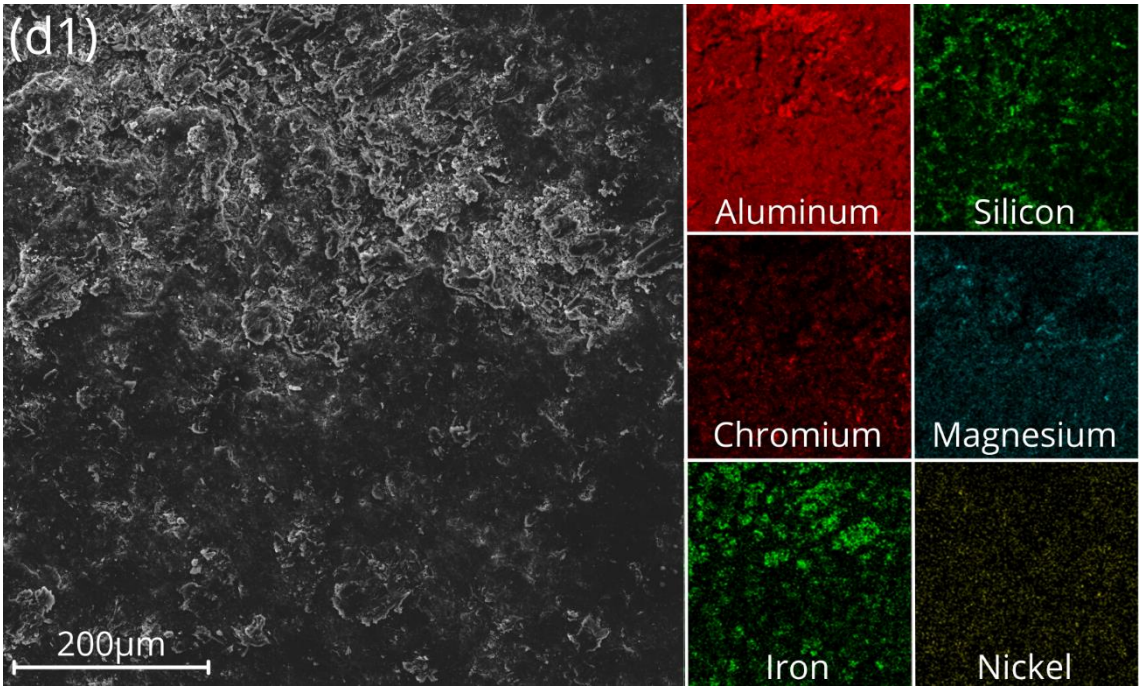

Reference: Author

Figure 57 - Surface EDS after extraction of the aluminum ring for HVOF of Cr_3C_2 25NiCr after 30 minutes in molten aluminum.

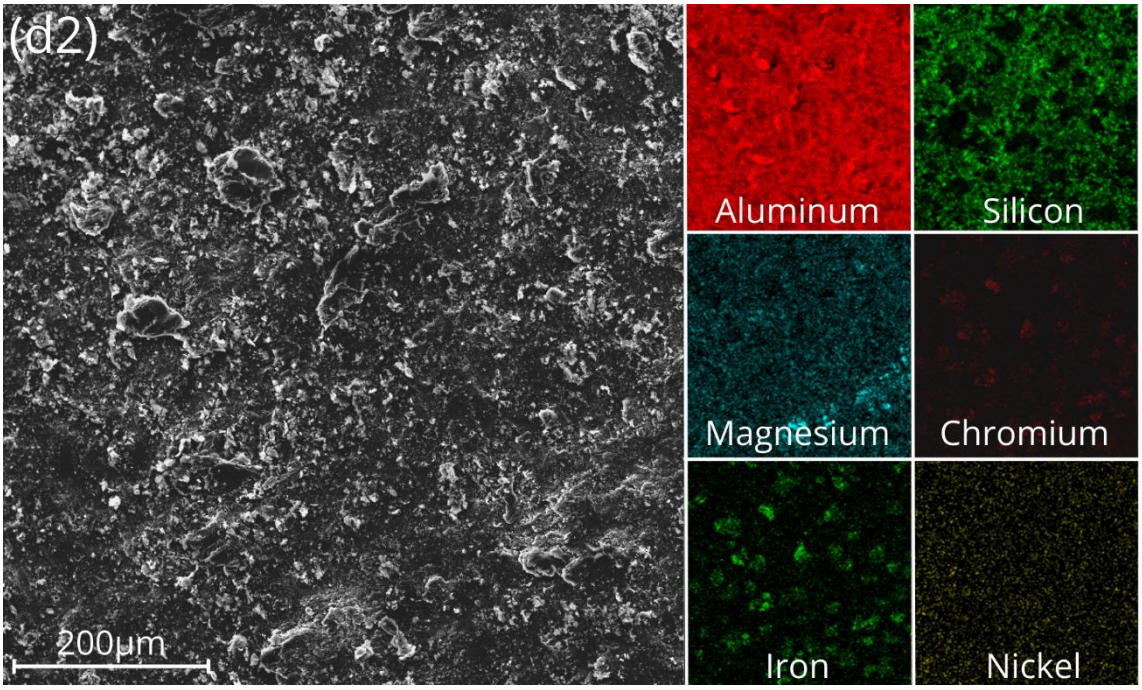

Reference: Author

Figure 58: Extracted aluminum rings from simple cast samples SEM images. (a) AISI H13, (b) AlCrN PVD, (c) HVOF of AISI H13 and (d) HVOF of Cr_3C_2 25NiCr.

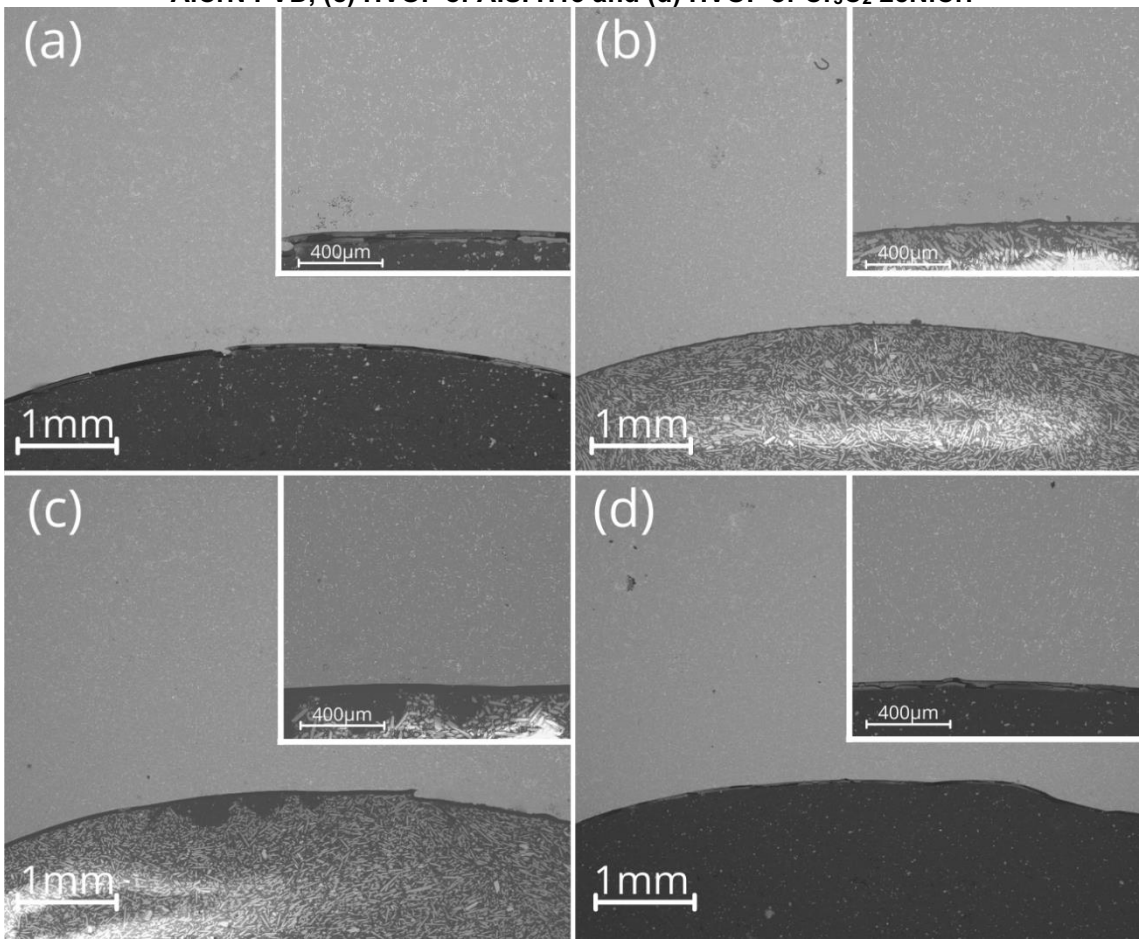

Reference: Author

Figure 59:Extracted aluminum pins from simple cast samples SEM images. (a) AISI H13, (b) AlCrN PVD, (c) HVOF of AISI H13 and (d) HVOF of Cr3C2 25NiC

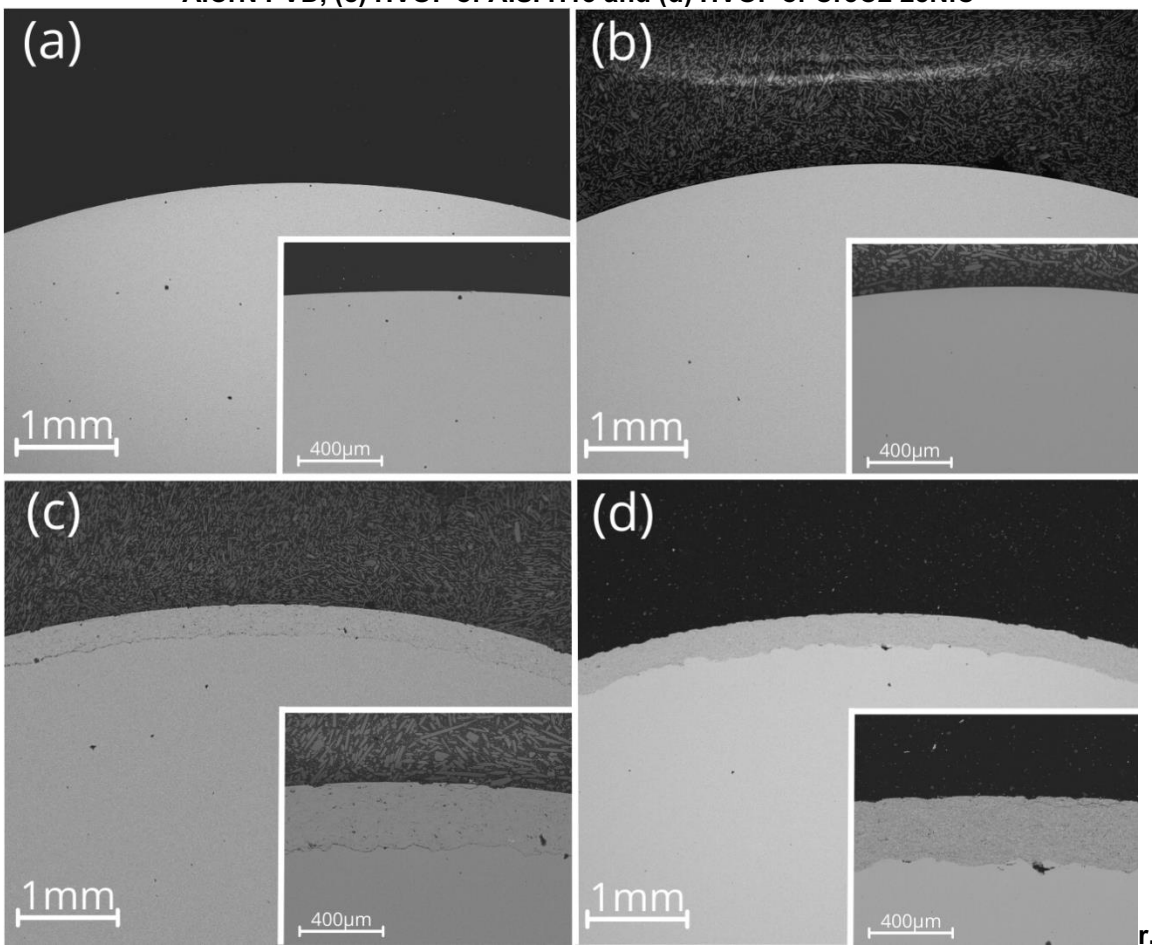

r.

Reference: Author

Figure 60 - Weight percentage of carbon after the formed intermetallic layer.

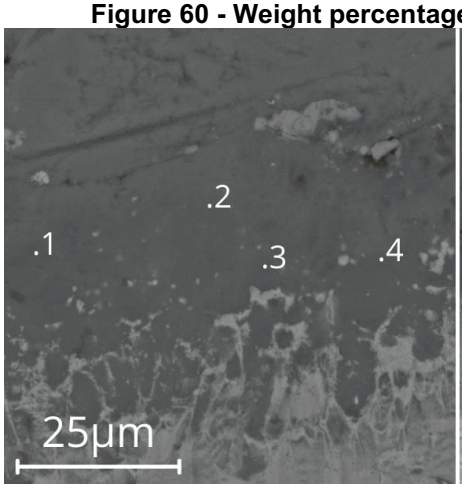

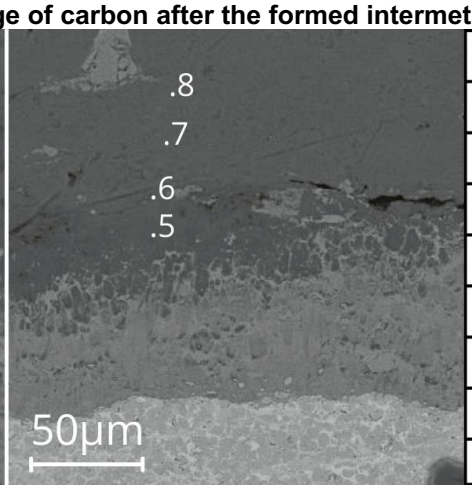

Point	C (Wt%)
1	17.2 ± 0.7
2	18.2 ± 0.7
3	17.4 ± 0.7
4	16.6 ± 0.7
5	17.7 ± 0.8
6	7.5 ± 0.8
7	3.7 ± 0.7
8	4.2 ± 0.8

Reference: Author

Figure 61 - Images of the diffusional layers for every sample. Aluminum ring extracted from AISI H13 after (a) 10 minutes and (b) 30 minutes at 720 °C. Aluminum ring extracted from AlCrN PVD after (c) 30 minutes. Aluminum ring extracted from AISI H13 deposited by HVOF after (d) 10 minutes and (e) 30 minutes at 720 °C. Cr_3C_2 25NiCr samples deposited by HVOF after being extracted from the aluminum ring after (d) 10 minutes and (e) 30 minutes at 720 °C.

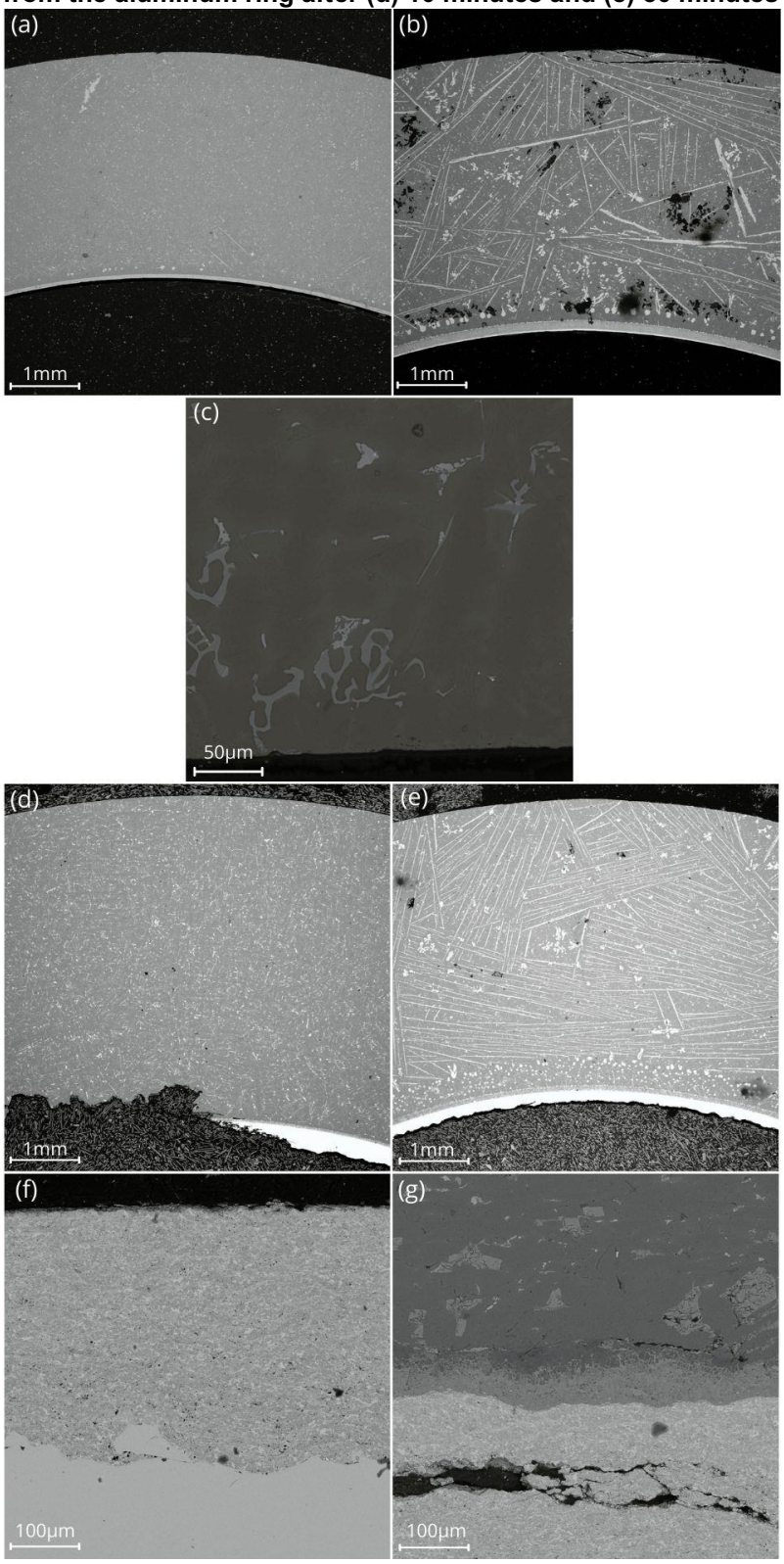

Reference: Author